Raman Spectroscopy on Selected Cooperative Systems

Inaugural-Dissertation

zur

Erlangung des Doktorgrades

der Mathematisch-Naturwissenschaftlichen Fakultät

der Universität zu Köln

vorgelegt von

Dipl. Phys. Andreas Raphael German

aus

Köln

Köln, 2022

Berichterstatter (Gutachter):

Prof. Dr. Paul H. M. van Loosdrecht

Prof. Dr. Daniele Fausti

Vorsitzender:
Prof. Dr. Andreas Eckart

Beisitzer:
Dr. Thomas C. Koethe

Tag der mündlichen Prüfung: 06.10.2022

Contents

Dedicated to:

The blond warrior, the struggle in the battle, and the beautiful spring.

We were stardust.

We will be stardust.

What we are is what we do between these two events.

- Dr. Fulvio Parmigiani.

Abstract

In this work we present different classes of materials, mainly investigated by Raman spectroscopy. It will be shown that even local symmetry changes influences the macroscopic properties of a material, and that Raman spectroscopy is a versatile tool, also in combination with other experimental and theoretical techniques, to investigate complex materials.

Optical microscopy, micro-photoelectron spectroscopy and micro-Raman spectroscopy showed in $Y_{0.63}Ca_{0.37}TiO_4$ that the temperature-driven conducting properties arise by the percolation of local conducting phases, forced by local structural changes. Simultaneously measured resistivity and macro-Raman spectroscopy on $Ca_2Ru_{0.99}Ti_{0.01}O_4$, along with phonon mode calculations, demonstrated the impact on the metal-insulator transition and the magnetic ordering by an applied electric current. Polarization-dependent Raman scattering and density functional studies point to the conclusion in $BiSbTeSe_2$ that the preferred local structure breaks inversion symmetry and explains consequently the unexpectedly high number of Raman active phonon modes. Time-resolved spontaneous Raman scattering spectroscopy on surface aligned 7-atom wide armchair graphene nanoribbons revealed that the exciton dynamics can be traced by optically induced changes of the phonon population.

Chapter 1

Introduction

My childhood's favorite toy was a box full of standardized colored bricks. I remember that I never got tired of creating something new with these little building blocks, over and over again. Later, I learned that nature consists also of little bricks. At that time (and even much later) three different bricks were enough for me, namely neutron, proton, and electron, to create everything between a bacterium and the stars. Of course, these are only a fraction (and even not the most basic ones) of the huge particle zoo of the standard model, but many of our explanations in physics, chemistry, or biology, are motivated by the interplay and the temporal connection of these three, interacting to compounds, forming complex structures, in order to decay back to its individual parts after some time. Over and over again. Two things dawned on me. First, I was the result of some recycled building blocks* and second, reincarnation must be a scientific concept. Therefore, it is surprising that although the basic building blocks are everywhere the same, e.g. in quantum objects or galaxies or inside us, the fundamental laws which describe the interactions between the particles and their environments depend on the considered length scales, at least in our scientific frameworks. Accordingly, physics is divided into different research fields, e.g., nuclear physics, condensed matter physics, astronomy, etc., where different fundamental forces become relevant.† An exception is the laws of thermodynamics which seems to be applicable all over the universe and at all times.‡ But, experimental findings and the

*The widespread belief is that all ever existing matter was created suddenly by the Big Bang. The estimated lifetime of a proton and an electron is 1.67×10^{34} yr and 6.6×10^{28} yr, respectively, which is pretty long compared to the age of the universe or the earth, 13.8×10^{9} yr and 4.5×10^{9} yr, respectively.

†Namely, gravitational, electromagnetic, strong, and weak force.

‡This is not necessarily true for the other fundamental forces. It is claimed that the universe needed some time to cool down after the Big Bang before the fundamental laws came to light. This took probably a few hundred years.

ongoing theoretical attempts to connect physical concepts by unifying theoretical models, try to understand how the universe is entangled.[§] A very general concept which is relevant on all length scales is symmetry. Hermann Weyl described it as follows: "A thing is symmetrical if there is something you can do to it so that after you have finished doing it, it looks the same as before.", where the "thing" describes the laws of physics, implying a close connection between symmetries and the fundamental laws of nature. This in turn demands invariant laws at any time and point in the universe. Emmy Noether realized the connection between geometric properties of space/time and physical quantities, showing the connection between symmetries and the conservation quantities like energy, momentum and angular momentum [1]. This result can not be overestimated. Also in condensed matter physics symmetry plays a key role, simplifying many calculations or allowing statements about possible transitions. An even more general approach to describe geometries is by the language of topology which describes objects and space by the number of their holes. Within the framework of topology it is possible to generate general statements about the universe as well as the geometry of the Fermi surface of a material (see, e.g. Ref. [2,3]). The results of the past decades in condensed matter physics (CMP) showed that quantum effects drive the macroscopic properties of many different materials. Therefore, CMP is a nutshell, equipped with a toolbox full of little bricks, which can be used on earth to understand the universe, because in the end everything is made of the same stardust.

1.1 Condensed Matter Physics

The material properties depend on various degrees of freedom which sometimes also interact with each other, e.g. SOC [4]. Often cited modern issues, such as spintronics or quantum computing, require the understanding of materials on a quantum level. Although the properties of quantum materials could in the most cases be approximated by a classical description, the origin is dictated by the quantum physical wave function of the electrons. Here, it is important to distinguish whether the effects come from interactions between electrons (anti-ferromagnetism, superconductivity, etc.) or from the the topological character of the wave function (topological insulators, Dirac semimetals, etc.). Combining these two effects generate even new classes of materials (spin liquids, topological superconductors, etc.). The properties of these materials

[§] An examples for the attempts to build a bridge between the different theories is the unification of the quantum field theory of electromagnetism and the weak force by assuming a common 'electroweak' force.

occur in many cases by the reduction of dimensionality, e.g. by the confinement of electrons in two-dimensional layers (Graphene) or one-dimensional strings (Graphene nanoribbons) which lead to collective excitations (quasiparticles) by the strong interaction of electrons [5]. Roughly, the materials can be split up into correlated electron and strong spin-orbit coupled (SOC) systems. Correlated electron physics describes the properties of 3d transition metal oxides and explains the insulating behavior of electronic materials by the interaction between electrons which fill the same orbital, leading to an enhanced Hubbard repulsion, U, between these electrons [4].

Many phenomena, e.g., local moment formation, magnetism, quantum criticality, and unconventional superconductivity, can be described by correlated electron physics [4]. SOC becomes relevant by increasing the atomic number ($\propto$ (atomic number)^4). Prominent examples are TIs ($BiSbTeSe_2$), Ruthenates (Ca_2RuO_4), or Iridates (Na_2IrO_3). SOC is defined as the interplay between the electron spin and the orbital angular momentum of an atom [4], considered in theory as a perturbation of the equilibrium Hamiltonian. By going from $3d$ to $5d$ elements, the $4d$ orbitals become more extended and consequently decreases the electronic repulsion U (Hubbard repulsion), as well as the correlation effects [4]. Thus, the splitting between degenerate states, orbitals and bands, caused by SOC, also reduces U and the kinetic energy [4].

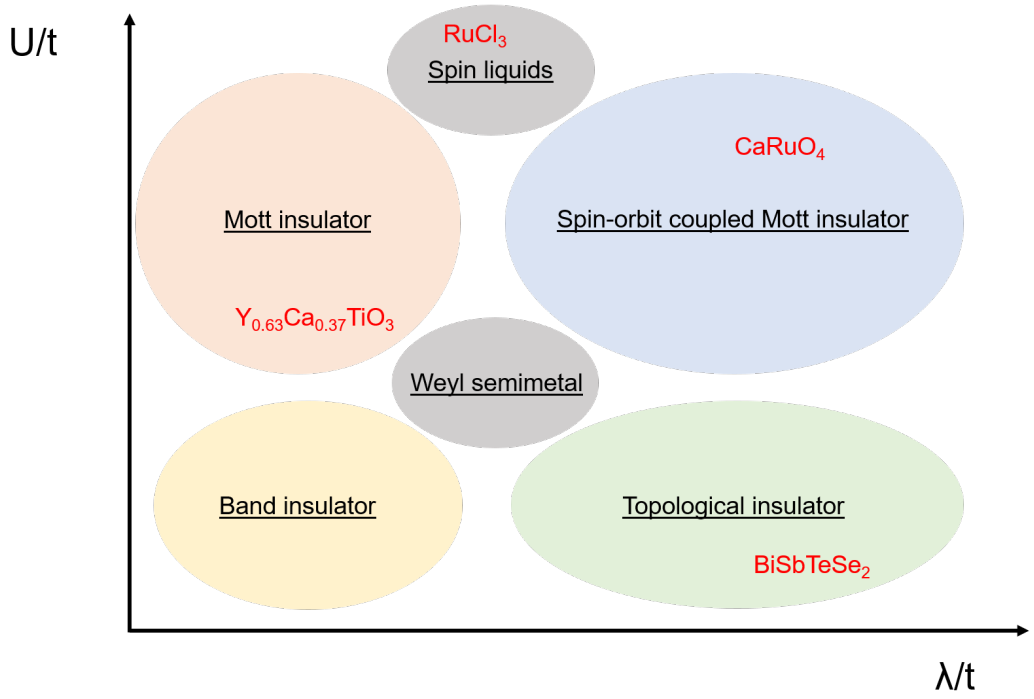

Figure 1.1: Examples of different material classes and materials, depending on λ and U, normalized by the hopping parameter t.

Fig.1.1 sketches a phase diagram depending on the relative strength of the interaction U/t, where t is the hopping amplitude, and the SOC λ/t, together with examples for the resulting material classes [4]. In transition metal materials, e.g. $Y_{0.63}Ca_{0.37}TiO_4$, SOC is negligible and if U is in the order of the bandwidth, W, a conventional metal-insulator transition (MIT) can take place [4, 6]. Increasing SOC at small U converts a metallic or semiconducting state into a semi-metal or to a topological insulator (TI), e.g., $BiSbTeSe_2$. Potentially, an insulating state is created when SOC and correlations are present in the system and they rather cooperate than compete [4]. The definition of cooperative systems is not uniformly given, but it describes systems where the behavior of sub-units strongly influence the macroscopic properties of the material by interacting together (e.g. percolation). Otherwise, highly correlated and competing interactions mostly lead to disorder. Current examples for highly quantum entangled phases of matter are quantum spin liquids, i.e. one-dimensional spin chain systems (e.g. $KCuF_3$), kagome antiferromagnet (e.g. $ZnCu_3(OH)_6Cl_2$), and Kitaev honeycomb materials (e.g. α-$RuCl_3$) [7]. The latter mentioned is a candidate for fermionic Majorana excitation, where SOC forces a favoured bond directional interaction and leads to frustration on the hexagonal lattice. Disorder by frustration is also known from anti-ferromagnetically coupled Ising spins on a triangle, where no preferred magnetic ordering is possible [8]. The complexity and variety of the interactions steadily increase and bring regularly new (topological) phases to light, e.g. Weyl semimetals [9, 10] or axion insulators [11].

1.2 Raman Spectroscopy as a Basic Tool to Study Complex-Exotic Materials

Phase transitions mostly go together with a symmetry change, at least locally. Therefore, a symmetry sensitive and non-invasive technique is needed to observe such symmetry changes. Raman spectroscopy is one of this "working horses" in CMP which is capable to provide this information and characterize materials under relatively simple experimental conditions [12]. Light-matter interaction create a lot of different phenomena. Luminescence (also fluorescence and phosphorescence) denotes the absorption and the subsequent spontaneous emission of light, where the emitted photons are in the most cases lower in energy (longer wavelength) than the one which was absorbed. When the energy of the incoming and the outgoing photon is identical then it is elastic light scattering and is called Rayleigh scattering [13]. For inelastic light

scattering the energy of the outgoing photon changes. Examples for this are Brillouin scattering, Compton scattering, and Raman scattering which describe inelastic scattering of acoustic waves in crystals, scattering of charged particles, and the creation and annihilation of phonons, respectively [13]. Under convenient conditions, Raman scattering is able to measure all of these types of light-matter interactions, and probe both electronic and vibrational properties. Besides the most used spontaneous Raman spectroscopy exist more than two dozen different kinds of Raman spectroscopy techniques, e.g. hyper-Raman scattering, coherent anti-Stokes Raman scattering (CARS), stimulated Raman scattering, surface-enhanced Raman scattering (SERS), or tip-enhanced Raman scattering (TERS) [13].

In the past, numerous Raman spectroscopy experiments were done to investigate and characterize materials, e.g., 2D materials [14], transition metal dichalcogenides [15], phonon modes in crystals [16–18], counting (mono)layers [14,19], the breathing between the layers and their shear modes [19], the level of doping [20–26], graphene edges [27,28], disorder [29–31], thermal conductivity [15, 32, 33], anisotropy [34], strain and stress [35–38], the degree of crystallinity of cellulose [39], oxidation [40], hydrogenation [41], chemical functionalization [42], electrical mobility [43], thermal conductivity [32, 33], electron–phonon [31,33,44–46], and electron–electron [45,47,48] interactions, magnetic field [49–54], and interlayer coupling [55–57].

1.2.1 Enhanced Raman Spectroscopy

The signal of the spontaneous Raman spectroscopy signal is increased by various approaches, e.g. by resonance Raman spectroscopy, SERS [58] or TERS [59, 60] . Resonance Raman spectroscopy can probe both electronic and vibrational properties at once and is proven for low-dimensional materials, like graphene or transition metal dicalchogenides [61]. It probes the number of layers [19, 62], strain fluctuations on small scales [35, 63–66], the distribution of doping domains [65, 67, 68], excitonic effects [69], the lattice temperature [32], phonon and electron lifetimes [49, 70–72].

The signal enhancement of the Raman signal can be achieved by different approaches, e.g. TERS and SERS which manipulates the surface nanostructure [73, 74] and uses charge density oscillations (plasmons) to enhance locally the light-matter interaction [75].

The spatial resolution of TERS is in the nanometre regime [76–78] and can be therefore used forvery thin and small crystalline materials [79] e.g. carbon nanotubes [74,80,81], single strands of RNA/DNA [82,83], redox reactions [84], or the investigation

and mapping of molecules [13, 60].

1.2.2 Coherent Raman Spectroscopy

Stimulated Raman scattering (SRS) is a general term for a lot of different nonlinear techniques. In contrast to spontaneous Raman scattering is SRS a coherent process which increases the signal and follows the time evolution of the excitation [13, 85]. Coherent light-scattering events need several incident photons (induced by several laser beams) which brings the material out-of-equilibrium [13].

There is a broad variety of applications for SRS, e.g. plasma physics [86], atomic interferometry [86–89], monitoring chemistry in living cells [90], and supercontinuum generation [91]. The latter is achieved by an intense light pulse passing through a nonlinear material [13, 87, 91].

But also techniques like CARS has a broad field of applications, such as biological medicine [92, 93], single-photon fluorescence [94], μ-CARS for live cell imaging [92], skeletal stem cells [95], tracing toxity in nano-materials [96], and tumour detection [97]. Because of its high temporal and spatial resolution, CARS is also used als thermography technique for electronic and opto-electronic device characterisation [98].

1.3 Thesis Overview

This thesis presents the manifold possibilities of modern Raman spectroscopy on the basis of selected materials. Chapter 1 motivates the topics discussed in this work and put the techniques and the investigated materials in the current research framework. Chapter 2 gives a brief overview of the theoretical background which is needed in the following Chapters.

In Chapter 3, the peculiar composition of $Y_{0.63}Ca_{0.37}TiO_3$ is presented. It exhibits a temperature driven change in the resistivity from conducting at low temperatures, to insulating at high temperature and shows, similar to VO_2, stripe-like patterns below the crystalographic transition temperature. The lattice vibrations of Ca_2RuO_4 influenced by an applied current are discussed in Chapter 4. Additionally, the magnetic ordering of Ca_2RuO_4 is susceptible to an applied current, shown in Chapter 5. Chapter 6 presents the local structure of the topological insulator $BiSbTeSe_2$, revealed by the investigated phonon modes. In contrast to the previous chapters, where spontaneous Raman spectroscopy is used, shows Chapter 7 the time-resolved Raman spectroscopy measurements of 7-atom Graphene Nanoribbons which reveal exciton dynamics.

Chapter 2

Theory

2.1 Spontaneous Raman Scattering

The Raman effect is caused by inelastic scattering of light in a medium (e.g. crystals, liquids, gases). It origins from optical modes of quasi-particles (e.g. phonons, magnons, plasmons) generated by the polarizibility change of molecules or the susceptibility change of the medium. Therefore, the Raman effect is the result of the response modulation generated by vibrations in the system [16, 99]. Raman spectroscopy is able to investigate novel states of matter both in the frequency and in the time domain.

2.1.1 First-Order Raman Effect

The first-order Raman effect is an one-photon-in and one-photon-out process which takes place approximately in 1 of 10^7 cases. Thus, the significant amount of the incident light is scattered elastically, called Rayleigh scattering. The inelastic scattering is divided into frequencies smaller and larger than the incident photon energy, ω_i, associated with a loss or gain of energy by creating or annihilating a phonon, denoted as Stokes and Anti-Stokes scattering, respectively. Fig. 2.1a shows a simple quantum mechanical sketch of the Raman process in which the system is raised from a real (i) to a virtual (v) state by the incident light ω_i, followed by a relaxation of the system back to a real state (f) by emitting light with the frequency ω_s. Without external forces (e.g. additional light sources) this process takes place spontaneously and is therefore denoted as spontaneous Raman spectroscopy. Infra-red (IR) - spectroscopy is a complementary technique to Raman spectroscopy that allows the investigation of vibrational modes that are not visible in the Raman process for reasons of symmetry. In IR- spectroscopy the wavelength of the irradiated light is of the order of the (optical) phonon

wavelength and the electric field of the light (transverse to the propagation direction) and the transverse optical (TO) phonon are directly coupled. For the case of photo luminescence the incoming photon has several times the energy of an optical phonon, where excited electrons (or holes) thermalize emitting optical and acoustic phonons until they recombine [100]. Both, Stokes and Anti-Stokes, give potentially the same spectra with the same energies, but differ mostly in their intensities, Fig. 2.1b. Anti-Stokes scattering requires the presence of phonons in the material which is naturally given at higher temperatures, according to the Bose-Einstein factor [100]. This is the reason why mostly Stokes scattering is presented in this thesis, unless it is otherwise indicated.

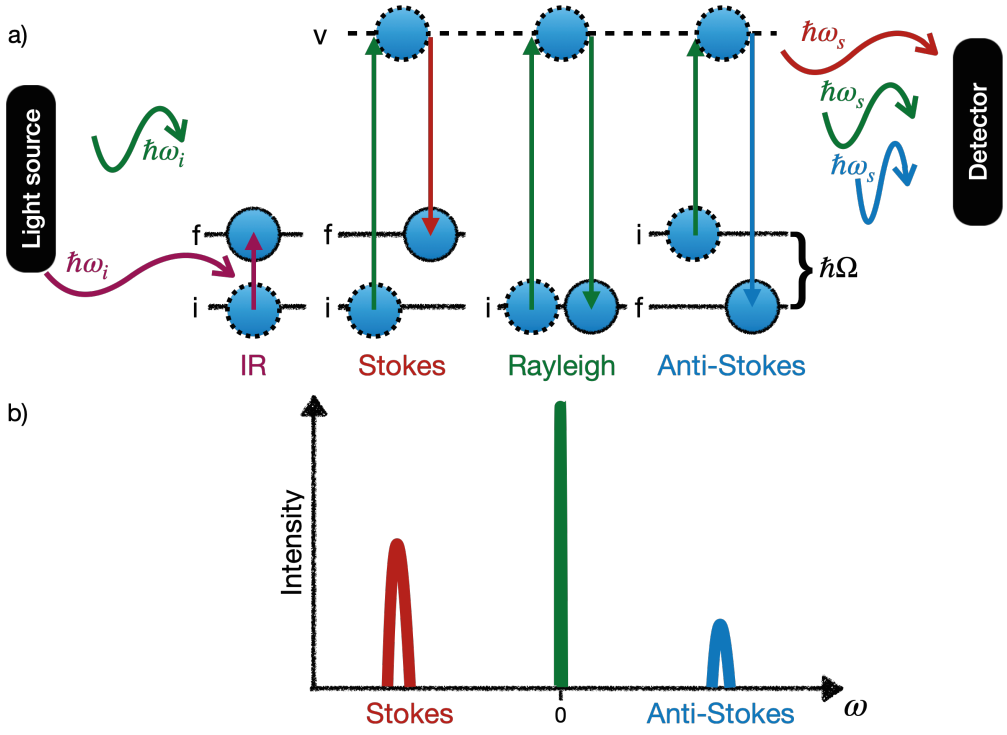

Figure 2.1: Sketch of the a) IR, Stokes, Rayleigh, and Anti-Stokes scattering process, where Ω is the energy of the resulting excitation (phonon), and b) are the corresponding spectra.

The Raman light-scattering processes in Fig. 2.1 measures the difference between the incoming and outgoing light and can be summed up by energy conservation

$$\hbar\omega_i = \hbar\omega_s \pm \hbar\Omega \tag{2.1}$$

and momentum conservation

$$\hbar\mathbf{k_i} = \hbar\mathbf{k_s} \pm \hbar\mathbf{q}, \tag{2.2}$$

where ω_i and ω_s are the laser frequencies for the incoming and outgoing light, Ω is the frequency of the excitation, $\mathbf{k_i}$ and $\mathbf{k_s}$ are the momenta of the incoming and outgoing light, and $\mathbf{q}$ is the momentum of the excitation. The sum and the subtraction in Eq. 2.1 and Eq. 2.2 stands for creation and annihilation of the excitation. First-order Raman spectroscopy considers excitations close to the Brillouin zone center ($\Gamma-$ point), i.e. $q \approx 0$, due to the conservation of energy and momentum of the incoming photons. The magnitude of the photon momentum is small compared to the reciprocal lattice constant* which is indicated by the nearly vertical arrows, Fig. 2.2. This explains also the unavailability of acoustic phonons by first-order Raman spectroscopy. But, under special conditions and in some materials, e.g. Silicon, also phonons from the high symmetry points of the Brillouin edges are measurable, e.g. by two-phonon excitation.

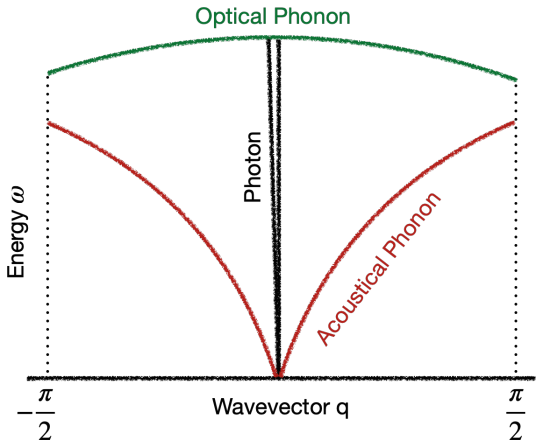

Figure 2.2: Optical and acoustic phonon dispersion relation.

Historically, inelastic light scattering is described in two different ways, microscopically and macroscopically. In the microscopic view the classical harmonic-oscillator is quantized, Equ. 2.1, and the matrix elements of the electric-dipol operator describes the atom-light interaction. The macroscopic view is valid directly for extended media in which the individual atomic dipole moments form a macroscopic polarization vector and the scattered beam is radiated by the oscillatory macroscopic polarization, described by Maxwell equations [17].

*The optical frequency of a photon is $k = 2\pi/\lambda \sim 10^7$ m^{-1}, whereas the electron wave vector is $k = \pi/a \sim 10^{10}$.

2.1.1.1 Macroscopic Raman Theory

The change of the polarizability, α_0, describes the preference of a material to distort the electron density distribution by an external oscillating electric field $E(\omega)$, where $\omega = 2\pi\nu$ is the angular frequency of the monochromatic radiation. Generalized, it is connected to the frequency-dependent linear induced electric-dipole moment by

$$\mathbf{p}^{(1)} = \alpha \cdot \mathbf{E}, \tag{2.3}$$

where $\mathbf{p}^{(1)}$ is the modulated electric-dipole moment vector which is linear in $\mathbf{E}$, indicated by the superscript, and α is the polarizability (second-rank) tensor of the molecule [18]. Hence, one has to consider also higher order dipoles to obtain the total time-dependent induced electric dipole moment vector, such as

$$\mathbf{p_{tot}} = \mathbf{p}^{(1)} + \mathbf{p}^{(2)} + \mathbf{p}^{(3)} + h.o., \tag{2.4}$$

where the higher order dipol moments require also higher rank tensors, i.e. $\mathbf{p}^{(2)} = \frac{1}{2}\beta : \mathbf{EE}, \mathbf{p}^{(3)} = \frac{1}{8}\gamma\vdots\mathbf{EEE}$, etc. [18]. Especially, the second order Raman effect becomes relevant latter in this thesis. If the molecule does not rotate and only vibrates at its equilibrium position the variation of the polarizability can be approximated by a Taylor series for the components $\alpha_{\rho\sigma}$ of the polarizability tensor α

$$\alpha_{\rho\sigma} = (\alpha_{\rho\sigma})_0 + \sum_k \left(\frac{\partial\alpha_{\rho\sigma}}{\partial Q_k}\right)_0 Q_k + \frac{1}{2}\sum_{k,l}\left(\frac{\partial^2\alpha_{\rho\sigma}}{\partial Q_k \partial Q_l}\right)_0 Q_k Q_l + ..., \tag{2.5}$$

where Q_k and Q_l are normal coordinates for the vibrational frequencies ω_k and ω_l of the molecule [18]. The subscript '0' denotes the equilibrium configuration. For now, only the first derivative in Eq. 2.5 is considered so that

$$\alpha_{\mathbf{k}} = \alpha_{\mathbf{0}} + \alpha_{\mathbf{1}}\mathbf{Q_k} \tag{2.6}$$

Inserting Eq. 2.6, the time dependence of $Q_k = Q_{k_0}\cos(\Omega t + \delta_k)$, and the frequency dependence of $\mathbf{E} = \mathbf{E}_0 \cos\omega t$ into Eq. 2.3, one obtain

$$\mathbf{p}^{(1)} = \alpha_{\mathbf{0}}\mathbf{E_0} cos(\omega t) + \alpha_{\mathbf{1}}\mathbf{E_0}Q_{k_0}\cos(\Omega t + \delta_k)\cos(\omega t). \tag{2.7}$$

By applying the trigonometric identity[†] this becomes

[†] $\cos A \cos B = \frac{1}{2}[\cos(A+B) + \cos(A-B)]$

$$\mathbf{p}^{(1)} = \alpha_0 \mathbf{E_0} \cos(\omega t) + \alpha_1 \frac{\mathbf{E_0}}{2} \cos((\omega + \Omega)t + \delta_k) + \alpha_1 \frac{\mathbf{E_0}}{2} \cos((\omega - \Omega)t + \delta_k), \quad (2.8)$$

where the first part is the Rayleigh scattering, the second and the third describe the Anti-Stokes and Stokes scattering, respectively [99]. A necessary condition for Raman scattering is

$$(\frac{\partial \alpha}{\partial Q})_{Q=0} \neq 0. \quad (2.9)$$

This means that that at least one component of α compared to Q has a non-zero gradient at the equilibrium position. $\mathbf{p}^{(1)}$ is directly connected to the dielectric polarization $\mathbf{P}$[‡] and the electric susceptibility tensor, χ_{ij}, by

$$\mathbf{P} = N\mathbf{p}^{(1)} = N\alpha\mathbf{E} = \epsilon_0 \chi_{ij} \mathbf{E}, \quad (2.10)$$

where N counts the molecules per unit volume. The Raman cross section is derived by applying the fluctuation-dissipation theory to the polarization (more details can be found in Ref. [17, 18, 99]) and depends on various parameters, i.e. the frequency of the incident light, the scattering volume, the refractive index, the Raman tensor, etc. The polarization dependent macroscopical cross section is defined as

$$\frac{d^2\sigma}{d\Omega d\omega_s} = \frac{\hbar \omega_I \omega_S^3 V \nu \eta_S |\epsilon_0 e_S^i e_I^j \chi_{ij,k}(\omega_I, \Omega)|^2 \{S/AS\}}{(4\pi\epsilon_0)^2 2c^4 \eta_I N \Omega} L(\Omega), \quad (2.11)$$

where ω are the frequencies of the EM fields, ν is the scattering volume, V is the scattering sample volume, $L(\Omega)$ describes the excitation line shape (specified in Sec. 2.1.3), N is the number of atoms, η is the refractive index, Ω is the energy of the involved excitation, S/AS is either $n(\Omega) + 1$ or $n(\Omega)$, depending on whether Stokes or Anti-Stokes is considered, $n(\Omega)$ is the Boltzmann factor[§], e is the polarization of the in or outgoing light, and the subscripts I and S denotes incident and scattered light, respectively [17]. The Raman tensor, $\chi_{ij,k} = \frac{\partial \chi_{ij}}{\partial Q_k}|_0$, describes material specific polarization dependent selection rules for the scattering process, compare Eq. 2.9.

[‡]Defined by Maxwell equation, $\mathbf{D} = \epsilon_0 \mathbf{E} + \mathbf{P}$, where $\mathbf{D}$ is the dielectric displacement, ϵ_0 is the dielectric constant, and $\mathbf{E}$ is the electric field.

[§]The ratio of probabilities of two states is known as the Boltzmann factor, depending on the energy difference between the states $\epsilon_j - \epsilon_i$: $\frac{p_i}{p_j} = e^{(\epsilon_j - \epsilon_i)/(k_B T)}$, where k_B is the Boltzmann-factor, and T is the temperature.

With the aid of group theoretical considerations and the symmetry of the Raman tensor Raman active modes can be found [16, 99]. The scattering intensity is proportional to $\mathbf{p_{tot}}^2$ and Eq. 2.11 can be simplified if the experimental conditions are fixed (e.g. scattering volume, laser wavelength, etc.) to

$$|\mathbf{p_{tot}}|^2 \propto I \propto C|\sum_{ij} e_j^s \chi_{jl,k} e_l^i|^2, \tag{2.12}$$

where C is a constant containing all fixed values of Equ. 2.11 [99].

2.1.1.2 Microscopic Theory of Inelastic Light Scattering

Microscopic theory of inelastic light scattering is based on time-dependent perturbation theory. It is needed, because the classical theory can not explain for example the thermal evolution of the response or resonance phenomena [17, 18, 101]. Following Ref. [18], the first-order electric dipole moment $\mathbf{p}^{(1)}$ has to reformulated into the quantum mechanical language

$$\left(\mathbf{p}^{(1)}\right) = \langle \Phi_f^{(1)} | \hat{p} | \Phi_i^{(0)} \rangle + \langle \Phi_f^{(0)} | \hat{p} | \Phi_i^{(1)} \rangle \,, \tag{2.13}$$

where $\Phi_{i/f}^{(0)}$ stands for the unperturbed time-dependent wave functions of the initial i and final state f, respectively, $\Phi_{i/f}^{(1)}$ are the first-order perturbed time-dependent wave functions, and $\hat{p}$ is the electric dipole moment operator [18]. The polarizability is then derived as

$$(\alpha_{\rho\sigma})_{fi} = \frac{1}{\hbar} \sum_{r \neq i,f} \left[\frac{\langle f|\hat{p}_\rho|v\rangle \langle v|\hat{p}_\sigma|i\rangle}{\omega_{vi} - \omega_0 - \Gamma_v} + \frac{\langle f|\hat{p}_\sigma|v\rangle \langle v|\hat{p}_\rho|i\rangle}{\omega_{vf} + \omega_0 + i\Gamma_v} \right], \tag{2.14}$$

where Γ_v is the full width of the (virtual) level v, i and f are initial and final levels, respectively. The left and the right term in the square bracket describes the Stokes and Anti-Stokes scattering as sketched in Fig. 2.1. For detailed derivation and for further reading see Ref. [17, 18, 99, 101, 102].

2.1.2 Second-Order Raman Effect

In contrast to the first order scattering, in the second order Raman scattering all phonons throughout the entire Brillouin zone can be active. In the macroscopic ap-

proach one has to expand the susceptibility derivative to a higher order. Therefore, the cross section for a two-phonon process is [17]:

$$\frac{d^2\sigma}{d\Omega d\omega_s} = \frac{\hbar\omega_I\omega_S^3 V\nu\eta_S}{4\pi\epsilon_0)^2 2c^4\eta_I}\frac{\hbar^2}{4N^2}\sum_{\sigma,\sigma'}\sum_{q}|\epsilon_0 e_S^i e_I^j \chi_{\sigma\sigma'}^{ij,0}(\omega_I,\Omega)|^2(\omega_{\sigma q}\omega_{\sigma q})^{-1} \times[n(\omega_{\sigma q}+1)][n(\omega_{\sigma q}+1)]\delta(\omega-\omega_{\sigma q}-\omega_{\sigma' q}) \tag{2.15}$$

2.1.3 Spectral Line Shapes

Spectral lines are radiation fields with a narrow frequency spectrum, caused by returning electrons from higher orbitals to the ground state after a transition probability determined lifetime [99]. For the analysis and interpretation of the data the line shape and its origin is of fundamental importance.

2.1.3.1 The Natural Line: Lorentzian

An excited atom (electron) losses energy by sending out EM radiation, described classically by the equation of motion of a damped oscillator

$$\ddot{x} + \frac{\mu}{m}\dot{x} + \frac{k}{m}x = 0, \tag{2.16}$$

where k is the spring constant, μ is the friction coefficient, and the m is the mass [103]. In this section we follow the approach described in Ref. [103]. Often, two definitions are made, first, $\omega_0^2 = k/m$, which gives an simple estimate of the phonon frequency depending on the involved atomic mass, and second, $\gamma = \mu/m$, which is the damping constant. The differential equation can be solved by the Ansatz $x(t) = Ce^{-\lambda t}$, where C is a constant. For small damping $\gamma \ll \omega_0$ and the boundary conditions $x(0) = x_0$ and $\dot{x}(0) = 0$ the solution is

$$x(t) = x_0 e^{-(\gamma/2)t} cos(\omega t), \qquad with \qquad \omega = \sqrt{\omega_0^2 - \gamma^2/4}, \tag{2.17}$$

The natural frequency ω_0 of the undamped oscillator corresponds to the transition from one energy level E_f to another E_i, i.e. $\hbar\omega_0 = \hbar\omega_{fi} = E_f - E_i$. The amplitude of the oscillation decays with time. As a consequence the frequency of the radiated EM wave is not monochromatic anymore, showing a spectrum of frequencies. $x(t)$ in Eq.

2.17 is a superposition of frequencies with the amplitudes $A(\omega)$ which is then described by a Fourier-transform

$$x(t) = \frac{1}{2\pi}\int_0^\infty A(\omega)e^{i\omega t}d\omega. \tag{2.18}$$

One obtain $A(\omega)$ by

$$A(\omega) = \frac{1}{2\pi}\int_\infty^\infty x(t)e^{-i\omega t}dt = \frac{1}{2\pi}\int_0^\infty x_0 e^{-(\gamma/2)t}cos(\omega_0 t)e^{-\omega t}dt \tag{2.19}$$

assuming $x(t) = 0$ for $t < 0$. In the area of ω_0, i.e. $(\omega - \omega_0)^2 \ll \omega_0^2$, the intensity distribution is given by

$$I(\omega - \omega_0) = A(\omega) \cdot A^*(\omega) \tag{2.20}$$

$$= \frac{C}{(\omega_\sigma - \omega_0)^2 + (\gamma/2)^2} \tag{2.21}$$

The constant C is chosen that the total intensity is such

$$\int_{-\infty}^{+\infty} I(\omega - \omega_0)d(\omega - \omega_0) \cong \int_0^{+\infty} I(\omega)d(\omega) = I_0. \tag{2.22}$$

This results for C in Eq. 2.21 then to $C = I_0\gamma/2\pi$. The normalized intensity profile is called Lorentzian and is given by

$$I(\omega)/I_0 = L(\omega) = I_L = \frac{\gamma/2\pi}{(\omega_\sigma - \omega_0)^2 + (\gamma/2)^2}, \tag{2.23}$$

where $\int_0^\infty L(\omega)d\omega = 1$ is valid and γ is the natural line width.

The connection between the lifetime, τ, and the line width, γ, can be derived by Eq. 2.16 by multipliying it by $m\ddot{x}$

$$m\ddot{x}\dot{x} + m\omega_0^2 x\dot{x} = -\gamma m\dot{x}^2 \tag{2.24}$$

This can be reformulated to the total energy W by interpreting the left hand side

as kinetic and potential energy

$$\frac{d}{dt}\left(\frac{m}{2}\dot{x}^2 + \frac{m}{2}\omega_0^2 x\right) = \frac{dW}{dt} = -\gamma m\dot{x}^2, \tag{2.25}$$

using x as defined in Eq. 2.17 one obtain, assuming $\gamma \ll \omega_0$,

$$\frac{dw}{dt} = -\gamma m x_0^2 \omega_0^2 e^{-\gamma t}\sin^2(\omega_0 t). \tag{2.26}$$

The average over one Periode is

$$\langle\frac{dW}{dt}\rangle = -\left(\frac{1}{2}\right)\gamma m x_0^2\omega_0^2 e^{-\gamma t}. \tag{2.27}$$

From this one can derive that the emitted intensity $I(t)$ is proportional to $\langle\frac{dW}{dt}\rangle$, decaying from the start value $I(0)$ to $1/e$ after a time τ, defined as

$$\tau = \frac{1}{\gamma}. \tag{2.28}$$

2.1.3.2 Gaussian

Another common profile that in many cases represents inhomogenous broadening, e.g. caused by thermal motion of atoms, is the Gaussian

$$I_G(\omega - \omega_0) = \frac{1}{\sigma\sqrt{2\pi}} e^{-\frac{1}{2}\left(\frac{\omega-\omega_0}{\sigma}\right)^2}, \tag{2.29}$$

where σ and σ^2 are the standard deviation and the variance of the distribution, respectively.

2.1.3.3 Voigtian

The convolution between a Gaussian and a Lorentzian line is analytically not solvable and is called Voigtian [99]:

$$V(x;\gamma_L,\gamma_G) = (I_G * I_L)(x) = \int G(\tau)L(x-\tau)d\tau. \tag{2.30}$$

If γ_L and γ_G are the widths for the Lorentzian and Gaussian lines, respectively, the resulting line width is approximately given by [99]:

$$\gamma = 0.5346\gamma_L + \sqrt{0.2156\gamma_L^2 + \gamma_G^2}. \tag{2.31}$$

An approximation to an Voigt is a pseudo-Voigt which is an linear combination of Gaussian and Lorentzian such as

$$V_p(x) = \eta \cdot L(x) + (1 - \eta) \cdot G(x), \tag{2.32}$$

where $0 < \eta < 1$.

2.1.3.4 Fano Resonance

Fano resonance effects occur if oscillators with a discrete frequency interact with a continuum transition [99]. This special emission scattering cross section is characterized by a so-called Fano profile

$$\sigma = \frac{(\epsilon + q)^2}{\epsilon + 1}, \tag{2.33}$$

where q is a phenomenological shape parameter and ϵ is a reduced energy, defined by $2\frac{E-E_r}{\Gamma}$; E_F is a resonant energy, and Γ is the width of the resonance.

There are three special cases of resonance profiles:

$q = 0$: Antiresonance characteristic where a dip trough appears at the center of the resonance.

$0 < q < \infty$: Asymmetric resonance with maximum peak and minimum trough.

$q = \infty$: Lorentzian shape resonance, which is typically seen in oscillating systems [104].

2.1.4 Raman Shift

The Raman shift measured in a Raman experiments is given in the unit wavenumbers, $\Delta\bar{\nu}$. It is defined as the frequency difference between the scattered radiation ($\nu_{scatter}$) and the incident light (ν_0) [105]:

$$\Delta\bar{\nu} = \frac{1}{c}(\nu_0 - \nu_{scatter}) \tag{2.34}$$

The common unit used in Raman spectroscopy is cm^{-1}.

2.1.5 Lattice Temperature Determination

In principle, there exist two different ways to calculate the lattice temperature. The first possibility is to follow the peak shift by changing the temperature. One would expect for an increased temperature a decreased vibrational energy according to the increased bond length [106]. To investigate the temperature like this one need narrow Raman bands. This method is not very easy from the practical point of view. It needs a very precise calibration for a given material, since different materials have different shifts of their phonons or even none. In addition, on lowering the temperature some phonons might show a decrease rather than an increase in energy. Finally, phase transitions might give shifts in frequencies (1st order) and also change the temperature derivative of the frequency. The second, and the more convenient possibility is to compare the intensity of selected Raman bands at the Stokes and anti-Stokes side, calculating the temperature by the Boltzmann distribution [106]. The expressions, which describes this is

$$\frac{I_{AS}}{I_S} = \frac{(\omega_0 + \Omega)^4}{(\omega_0 - \Omega)^4} \exp^{-\frac{h\Omega}{k_B T}}, \tag{2.35}$$

where ω_0 is the laser frequency and Ω is the phonon frequency [99]. There exist also variation of this equation where the exponent is '3' instead of '4'. The first variant is reported to be more convenient for energy-based detection. The latter one is needed for measurements where photon counting is more important [106, 107] which is the case when a charge-coupled device (CCD) is used for detection. One has to admit that in many experimental issues the difference between the two exponents are negligible, because of the experimental error bars.

2.1.6 Resonant and Electronic Raman Scattering

In contrast to the previously described Raman process, the electron is not excited to a virtual level, but to an eigenstate of the system. This considerably increases the probability that a phonon will be generated, which becomes directly visible in the increased magnitude (intensity). The Heisenberg uncertainty principle describes the lifetime of an excitation excited to a intermediate virtual state which becomes more

stable the closer it is to the energy of an eigenstate, because the energy conservation is not violated anymore [99]. Discrete excited states or critical points in the density of states are important for the resonance scattering process [99].

2.2 Magnetic Raman Scattering

2.2.1 One-Magnon Scattering

Following here the derivations from Cottam et *al.* [108] which are based on results mentioned in Ref. [17, 109]. χ has to be expanded in terms of variables which describe the excitation propagation within the solid. Therefore, the effective Hamiltonian $\mathcal{H}'$ represents the interaction of light with the magnetic system and is related to χ by

$$\mathcal{H} = \sum_{r} \sum_{\alpha,\beta} E_I^{\alpha} \chi^{\alpha\beta}(\boldsymbol{r}) E_S^{\beta} \tag{2.36}$$

The susceptibility of magnetic materials is spin-dependent which efforts an expansion in powers of the spin operators at site $\boldsymbol{r}$

$$\chi^{\alpha\beta}(\boldsymbol{r}) = \chi_0^{\alpha\beta}(\boldsymbol{r}) + \sum_{\mu} K_{\alpha\beta\mu}(\boldsymbol{r}) S_r^{\mu} + \sum_{\mu,\nu} G_{\alpha\beta\mu\nu}(\boldsymbol{r}) S_r^{\mu} S_r^{\nu} + \sum_{\delta} \sum_{\mu,\nu} H_{\alpha\beta\mu\nu}(\boldsymbol{r}, \boldsymbol{\delta}) S_r^{\mu} S_{r+\delta}^{\nu} + h.o., \tag{2.37}$$

where the first term is the susceptibility in the absence of any magnetic excitation, corresponding to an elastic scattering contribution. Magnon excitations are associated with transverse spin components. $K_{\alpha\beta\mu}, G_{\alpha\beta\mu\nu}, H_{\alpha\beta\mu\nu}$, describe the strength of the light-matter interaction. $K_{\alpha\beta\mu}$ is the coefficient for the one- magnon scattering (also first-order Elliot-Loudon scattering) and is proportionally connected to the magnetic circular birefringence (Faraday rotation). $G_{\alpha\beta\mu\nu}$ contributes to one-magnon scattering, and second-order Elliot-Loudon scattering which is then proportional to the magnetic linear birefringence (Voigt effect) [110]. $H_{\alpha\beta\mu\nu}$ describes exchange scattering. If SOC is involved it is possible to couple an electric-dipole to the spin system. As an example, and as an easier variant of anti-ferromagnetic Hamiltonian, the ferromagnetic

Hamiltonian is presented

$$\mathcal{H}_{1M} = \frac{1}{2}K\sum_r[(E_I^z E_S^+ - E_I^+ E_S^z)S_r^-(E_I^z E_S^- - E_I^- E_S^z)S_r^+] - iK\sum_r(E_I^x E_S^y - E_I^y E_S^x)S_r^z \tag{2.38}$$

$$+\frac{1}{2}G\sum_r[(E_I^z E_S^+ - E_I^+ E_S^z)(S_r^+ S_r^z + S_r^z S_r^+) + (E_I^z E_S^+ - E_I^+ E_S^z)(S_r^- S_r^z + S_r^z S_r^-)], \tag{2.39}$$

where the operators $S_r^\pm$ and $E_r^\pm$ are defined as

$$S_j^\pm = S_j^x \pm iS_j^y, \tag{2.40}$$

$$E_\zeta^\pm = E_\zeta^x \pm iE_\zeta^y, \tag{2.41}$$

where $\zeta = (I, S)$, standing for incoming and scattered.[¶]

Many antiferromagnetic insulators which is the more relevant candidate in this work, provide an excellent approximation to the Heisenberg exchange model and the the theory is similar to the ferromagnetic variant.

2.2.2 Two-Magnon Scattering

At two-magnon scattering pairs of magnons are involved. Therefore, the measured frequency shift is the sum of both $\Omega_{2M} = \Omega_{\boldsymbol{k}} + \Omega_{\boldsymbol{k'}}$ [109]. In principle, higher order terms of Eq. 2.37 are responsible for two-magnon scattering, but also exchange scattering mechanisms could contribute. The wave functions of two magnon excited states can

[¶]

$$[S_i^+, S_j^-] = 2S_i^z\delta_{ij}, [S_i^z, S_j^\pm] = \pm S_i^\pm\delta_{ij}. \tag{2.42}$$

A common approach in magnon theory is to transform spin operators to boson (or combinations of fermion) operators, which satisfy simpler relations. Due to Holstein-Primakoff

$$S_j^+ = \sqrt{2S}\sqrt{\left(1 - \frac{a_j^\dagger a_j}{2S}\right)}a_j, \tag{2.43}$$

$$S_j^- = \sqrt{2S}a_j^\dagger\sqrt{\left(1 - \frac{a_j^\dagger a_j}{2S}\right)}, \tag{2.44}$$

$$S_j^z = S - a_j^\dagger a_j, \tag{2.45}$$

where $a_j^\dagger$ (a_j) is boson creation (annihilation) operator, satisfying $[a_j, a_j^\dagger] = \delta_{ij}$.

be described by $|+\boldsymbol{k}\uparrow>$, $|-\boldsymbol{k}\uparrow>$, $|+\boldsymbol{k}\downarrow>$, $|-\boldsymbol{k}\downarrow>$, where $\pm\boldsymbol{k}$ is the magnon momentum on the spin-up or spin-down ($\uparrow$ or $\downarrow$) magnon branch [110]. Following 4 excited states are possible

$$
\begin{aligned}
|A\rangle &= |+\boldsymbol{k}\uparrow\rangle\,|-\boldsymbol{k}\uparrow\rangle && \Delta S^Z = +2,\\
|B\rangle &= \frac{1}{\sqrt{2}}[|+\boldsymbol{k}\uparrow\rangle + |-\boldsymbol{k}\uparrow\rangle] && \Delta S^Z = 0,\\
|C\rangle &= \frac{1}{\sqrt{2}}[|+\boldsymbol{k}\uparrow\rangle - |-\boldsymbol{k}\uparrow\rangle] && \Delta S^Z = 0,\\
|D\rangle &= |+\boldsymbol{k}\downarrow\rangle\,|-\boldsymbol{k}\downarrow\rangle && \Delta S^Z = -2,
\end{aligned}
$$

where $|A\rangle$ and $|D\rangle$ are the excited states due to the second-order Elliot-Loudon scattering, $|C\rangle$ describes the exchange scattering, and the even parity state $|B\rangle$ is the two-magnon absorption (not Raman active) [108–110]. For exchange scattering an anti-ferromagnet is needed with two magnon branches, in contrast to a ferromagnets with only one magnon branch. To describe the two-magnon process by the Hamiltonian, presented in Eq. 2.36, the higher order terms of Eq. 2.37 are needed.

2.3 Topology and Topological Insulators

Topology describes geometrical structures under continuous elastic deformation, e.g. stretching or compression. Objects are topologically equivalent when they are smoothly deformable into each other, even when distances and angles are changed. A sphere can be smoothly deformed into a disk, but not into a doughnut. Euler discovered that geometrical objects can be categorized by their number of holes, denoted as genus g, allowing to calculate the Euler characteristic χ.[‖] The Euler characteristic in turn is connected to the curvature of its surface by the Gauß-Bonnet-theorem.[**] Therefore, objects with smooth surfaces can be characterized topologically decisively even if they

[‖] Euler connected the number of corners (C), edges (E), and surfaces (S) of an object with its number of holes (g) by the polyhedra formula:

$$C + S - E = 2 - 2g = \chi, \tag{2.46}$$

where χ is the Euler characteristic.

[**] The Euler-Poincare characteristic of closed surfaces, with a topological invariant:

$$\chi(A) = \frac{1}{2\pi}\int_A^{max} G dA, \tag{2.47}$$

where G is the Gaussian curvature.

have no edges, corners, or when the surfaces are open. These considerations become important when one want to apply topology on the band structure.

Many properties of a periodic material are encoded in its band diagram which exists in the reciprocal space (Fourier space) and describes the connection between momentum and energy of a propagating wave. The band diagram delivers the surfaces, which one can describe with topological tools. The bottle neck here is that the definition of a hole is different in Fourier space and is solved by introducing a Berry curvature. With the Berry curvature and a theorem which is similar to the Gauss-Bonnet theorem it is possible to define a value, which represents the Euler characteristic in reciprocal space, called Chern number. To every periodic band in the band structure belongs a Chern number, depending on the underlying Berry curvature (these are integer numbers, which allows the classification of a band into a topological class). The Berry phase describes the phase acquired under an adiabatic (slowly moving) cycle which are loops in momentum space.

2.3.0.1 Topological Insulators

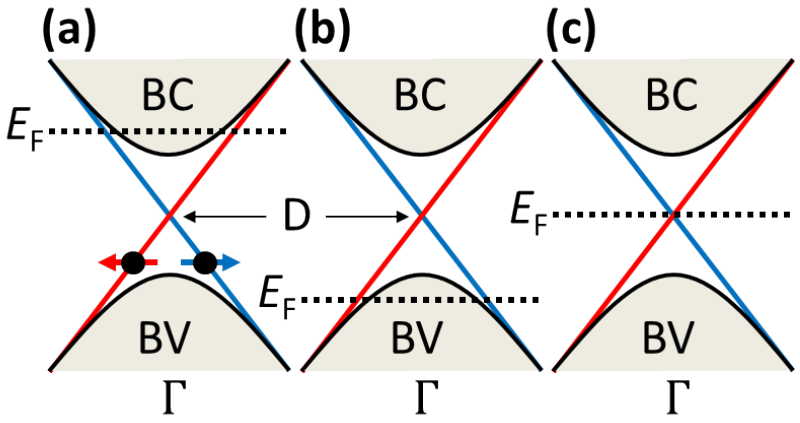

Figure 2.3: Band structure sketches of the bulk conduction band (BC), bulk valence band (BV) and the surface states (red and blue lines) for (a) p- type, (b) n- type, and (c) compensated topological insulator. The Fermi level, the Dirac- , and the Γ-point, are indicated by E_F, D, and Γ, respectively. Red and blue arrows illustrate spin-momentum locking for the electrons.

Solid state physics denotes materials with bulk insulating and surface conducting properties as topological insulators (TI). This class of materials has additionally to the energy gap between highest occupied electronic valence and the lowest empty conduction band, a conducting gapless surface/edge (depending if it is a 3D- or 2D- TI,

respectively) state, which is forced by the fundamental symmetry (topology) of its band structure. Ideally, the surface states exist within the bulk energy gap where it allows dissipationless electron conduction and the electron spin direction is perpendicular to the momentum vector [111]. Under this special conditions of spin polarization and perserving TRS, Kramers theorem dictates that the two eigenstates of the opposite momentum-spins crosses at the Γ- point, resulting into a gapless surface state [111].Fig. 2.3 illustrates the differences between (a) the prototypical p- type 3D topological insulator Bi_2Te_3 and (b) the n- type Bi_2Se_3, aswell as (c) the compensated $BiSbTeSe_2$.

2.4 Experimental Setup

The main part of this thesis was measured by spontaneous Raman scattering (macro-Raman setup) in back-scattering geometry. A subtractive triple spectrometer has been used as the dispersive component and the signal detected by a nitrogen cooled charge-coupled device camera (CCD).

Fig. 2.4 shows the sketch of a macro-Raman setup. The monochromatic light from the laser passes at first the "beam control" which is a combination of optical elements, such as $\lambda/2$- and $\lambda/4$- plates, polarizers, telescope, optical density filter, interference filter, to ensure a clean linear polarization and to control the intensity of the incoming light. Additionally, the polarization of the incoming laser light can be rotated in any needed angle, controlled by an polarizer before the mirror. The incoming laser light is focused by an objective on the sample in the cryostat. The back-scattered light is then collected with the same objective and focused on the entrance slit of the spectrometer by a lens. The polarization of the scattered light can be again selected by a polarizer. The spectrometer is equipped with three 1800 mm^{-1} gratings and is operating in double subtractive mode. Double subtractive mode means that the first two gratings work as monochromators which select the needed spectral range by blocking other frequencies. The first stage diffractes the light, the second stage merges the dispersed light, and the third stage finally disperse the light on the CCD. This process suppresses elastically scattered light so that the complete setup has a typical energy resolution of ≈ 1 cm^{-1}.

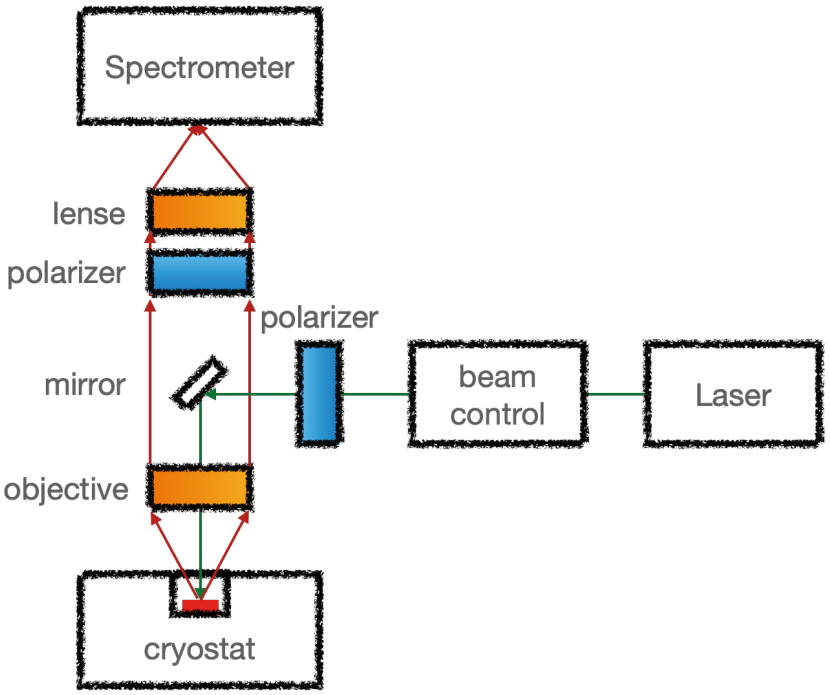

Figure 2.4: Macro-Raman setup.

Chapter 3

$Y_{0.63}Ca_{0.37}TiO_3$

We have performed optical microscopy, micro-photoelectron spectroscopy, and micro-Raman scattering measurements on $Y_{0.63}Ca_{0.37}TiO_3$ single crystals in order to clarify the interplay between the microstructure and the temperature dependent electronic transport mechanisms in this material. Optical microscopy observations reveal dark and bright domain patterns on the surface with length scales of the order of several to a hundred micrometers showing a pronounced temperature dependent evolution. Spatially resolved photoelectron spectroscopy measurements show the different electronic character of these domains. Using micro-Raman spectroscopy, we observe a distinct temperature dependence of the crystal structure of these domains. On the basis of these findings the different domains are assigned to insulating and metallic volume fractions, respectively. By decreasing the temperature, the volume fraction of the conducting domains increases, hence allowing the electrons to percolate through the sample at temperatures lower than ∼150 K.

3.1 Introduction

In the past decades the perovskite $YTiO_3$ has attained much interest as a toy material for correlated electron systems due to its simple Ti-3d^1 electronic structure. [6,112–114] It is classified as a typical Mott-Hubbard-insulator with a Mott-Hubbard gap of ~ 1 eV and charge transfer gap of ~ 4 eV. [115–117] By substituting Y^{3+} with Ca^{2+} in $Y_{1-x}Ca_xTiO_3$, i.e. hole-doping, first the ferromagnetic order vanishes at $x \sim 0.15$. By further doping, the macroscopic electronic property of this material changes from insulating to metallic at $x > 0.39$. For doping between $x = 0.33$ and $x = 0.39$ these samples exhibit a peculiar temperature driven metal-insulator transition (MIT), meaning that they are conducting at low temperatures and become insulating at higher

temperatures with a transition temperature ranging from $\sim$ 90 K to $\sim$ 220 K with increasing x. [118, 119] This is rather uncommon as mostly the insulating phase is found to be more stable at lower temperatures. The most remarkable in the doping range of $x = 0.33 - 0.39$ is the compound $Y_{0.63}Ca_{0.37}TiO_3$, which exhibits in addition a hysteresis in the electrical resistivity and the magnetic susceptibility. [120]

$Y_{0.63}Ca_{0.37}TiO_3$ undergoes a structural phase transition from high temperature orthorhombic Pbnm (HTO) to low-temperature monoclinic $P2_1/n$ (LTM) symmetry at $\sim$200 K. [121] This LTM phase has been shown to be orbitally ordered, and possibly also charge ordered. [122] As seen in electrical resistivity measurements, the compound is insulating at room temperature and the MIT for this compound takes place at $\sim$ 150 K. [123] * Thus the crystallographic transition from HTO to LTM is not related to a change in the macroscopic electronic property and the sample remains insulating in the LTM phase. Upon further cooling below 200 K, a low-temperature orthorhombic Pbnm (LTO) phase appears and starts to coexist with the LTM phase. [121] This LTO phase is distinguished from the HTO phase, as it has a smaller unit cell than the HTO phase. [122] The volume fraction of the LTO phase increases by lowering the temperature, accompanying the metal insulator transition. [123] Thus, a possible conducting character of the LTO phase would suggest a percolation mechanism underlying the MIT. The phase separation is also observed in conducting samples ($x > 0.40$), where the volume fraction of the LTO phase is high enough even at room temperature to render these samples conducting, assuming the LTO phase to be metallic. [124] In this work we will directly show the relationship of the crystallographic structure of $Y_{1-x}Ca_xTiO_3$ and its macroscopic electronic properties. For this we investigated the material $Y_{1-x}Ca_xTiO_3$ with $x = 0.37$, exhibiting the pronounced hysteresis at the MIT. [125] Optical microscopy studies allow to follow the temperature and spatial evolution of coexisting domains in this material. Using micro photoemission studies it is possible to classify the coexisting domains to conducting and insulating phases. Finally, using micro Raman studies, these coexisting domains are also classified to their crystallographic structures, hence allowing to directly relate the microstructure to the electronic behavior of this material, underlying the temperature driven MIT.

*The lattice parameters and physical properties of our samples with the chemical composition x = 37 %, as determined experimentally (see Sec. II), correspond to samples with x = 39 % in ref. [123].

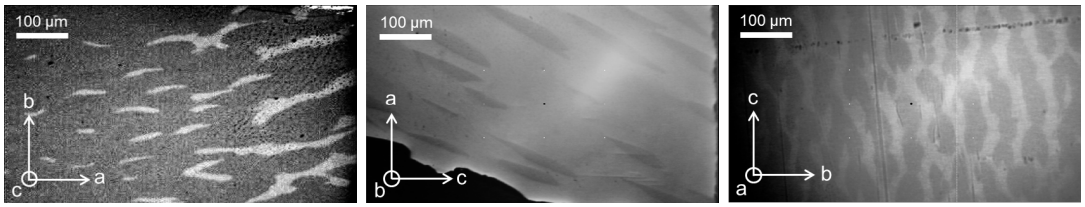

(a) T = 10 K; (001) (b) T = 10 K; (010) (c) T = 10 K; (100)

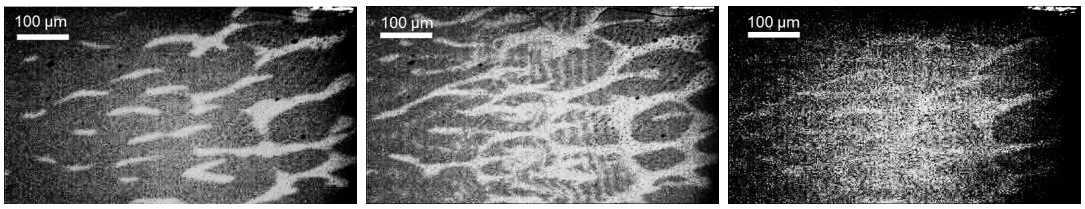

(d) T = 100 K; (001) (e) T = 170 K; (001) (f) T = 296 K; (001)

Figure 3.1: Microscope images of $Y_{0.63}Ca_{0.37}TiO_4$. (3.1a) - (3.1c) pattern formation for the three surface orientations, (001), (010), and (100), respectively, at 10K. (3.1d) - (3.1f) temperature evolution of the (001)-surface pattern.

3.2 Experimental

The untwinned single crystal $Y_{0.63}Ca_{0.37}TiO_3$ was grown by the floating-zone technique. The oxygen stoichiometry was checked by thermal gravimetric analysis (TGA) to be 3±0.02, while the Ca content was determined from a comparison of the measured lattice constants with the results of ref. [126] (see also ref. [125], Fig. 5.10) to be $x = 0.37\pm0.01$. The optical microscopy studies of the mechanically polished samples were done in the back-reflection geometry, using a microscope with an objective of 8x magnification and numerical aperture of 0.18. The photoemission microscopy was performed at the spectromicroscopy beamline operated by the Elettra storage ring. [127] Photons at 74 eV were focused through a Schwarzschild objective, to obtain a submicron size spot on the sample. The measurements were performed in ultra-high vacuum at a base pressure of $p < 2 \times 10^{-10}$mbar on *insitu* cleaved (001)-surfaces. The temperature of the sample was T = 110 K throughout the photoemission measurements.

For the spontaneous micro-Raman setup a continuous wave DPSS laser of 532 nm wavelength was used as a light source, sent through a microscope with a long distance objective and a numerical aperture of 0.2. The Raman scattered light was collected in a back-scattering geometry using a triple subtractive spectrometer equipped with a liquid nitrogen cooled CCD camera. This setup yields an energy resolution of 7 cm^{-1}. The samples were mounted in an Oxford Microstat cryostat, cooled by liquid Helium.

In this work the following back-scattering geometry for the Raman measurements was used: the incoming laser light propagates in the c-direction of the sample and the polarization of the incident and detected scattered light were each directed in the a-direction of the sample, abbreviated in the Porto notation as $c(aa)\bar{c}$. With the microscope, the spot-size of the laser beam is $\sim 30\mu m$ in diameter and the position of the laser spot on the sample was fixed with an accuracy of $\pm 2.5\mu m$. The power of the incident laser light was set to 1.7 mW.

3.3 Results and discussion

3.3.1 Optical Microscopy

The top panel of Fig. 3.1 shows microscope images of a $Y_{0.63}Ca_{0.37}TiO_3$ single crystal at $T = 10$ K in three different orientations, i.e. facing a (001), (010), and (100) surface of the material, respectively, with respect to the orthorhombic Pbnm symmetry. For each of these different orientations, specific patterns of bright and dark regions appear which show a preferred direction. As a result, the whole sample surface partitions in stripe-like patterns with a width of the order of 10 - 20 μm. While on the (100)-surface, these stripes extend across the whole field of view of several hundreds of μm, on the other two surfaces they form disconnected islands of one kind with extensions of the order of 100 - 200 μm within a background of the other kind. The bottom panel of Fig. 3.1 shows the evolution of the pattern with temperature from 100 K to room temperature for the (001)-surface. Comparing Fig. 3.1(a) and Fig. 3.1(d), it is seen, that islands of brighter areas exist at 10 K, which grow upon heating, while their shape is mainly maintained even at 100 K. Upon further heating a growth of these islands in a and b directions of the sample continues. However, this growth starts to take place more rapidly, so that these islands start to connect in a and b directions at $\sim$ 140 K. Furthermore, at $\sim$ 150 K, bright stripes evolving in b direction start to occur within the dark background. The width of these sub-stripes is $\sim 5\,\mu$m and the distance between the stripes is $\sim 20\,\mu$m. Finally, the brighter areas consisting of the former islands and the evolving stripes continue to grow and form a connected network as it is shown in Fig. 3.1(e) for 170 K.

The contrast between bright and dark areas continuously weakens above 100 K and eventually becomes insignificant at room temperature. However, by artificially enhancing the contrast of the microscope images, the different areas can be shown to still exist at 296 K, as shown in Fig. 3.1(f).

A noteworthy observation is the fact that the bright areas invariably show up in the same positions after several temperature cycles. Given the exceptionally high doping level, it seems likely to assume chemical inhomogeneity of the material to be the reason for this pattern. Additionally, the microscope images show temperature hysteresis of the surface fractions in the same temperature region as reported in the resistivity data. Remarkable is, however, the unusually large length scales in the range of many tens to hundreds of μm, i.e. several orders of magnitude larger than what had previously been reported. [124]

3.3.2 Spatially Resolved Photoelectron Spectroscopy

In order to investigate the electronic properties of the different areas observed in the microscope images, spatially resolved photoelectron spectroscopy measurements have been carried out at $T = 110$ K. The inset in Fig. 3.2a) shows the Ti $3d$ spectral weight for two different sites on the sample, denoted as 'A' and 'B'. As the blowup in the main panel reveals, the spectra especially differ in a narrow region close to the Fermi level, with 'B' being slightly more conducting than 'A'.

Fig. 3.2b shows a map of a $200\,\mu\text{m} \times 70\,\mu\text{m}$ area of the sample with a pixel size of $1\,\mu\text{m}^2$. The sample surface was oriented in [001]-direction and fractured before the measurement to get a clean surface. For each pixel, a full spectrum in the energy range as shown in the inset of Fig. 3.2a) has been taken. Photoemission intensity variations due to surface roughness etc. have been corrected for by normalizing each spectrum to unity. The map shows the integrated intensity in a narrow energy window around the Fermi level, i.e. the region where the spectra from sites 'A' and 'B' vary, as color values. Thus, more conducting regions appear bright and red in the Fig. in contrast to the insulating blue ones. The map reveals a similar domain pattern of stripes with a separation of $\approx 20\,\mu$m as had been observed in the microscope images.

Furthermore, a smaller scale stripe formation is recognizable. The widths and distances between these sub-stripes are of the order of $\sim 1\,\mu$m. Stripe-like features are also observed in the photoemission spectral weights of the O $2p$ band which is a natural consequence of the hybridization with the Ti $3d$, and presumably related to a rigid band shift. The presumption based on the microscope observations, that the origin of the stripe pattern might be chemical inhomogeneity, appears to be in line with the results of the photoelectron spectroscopy.

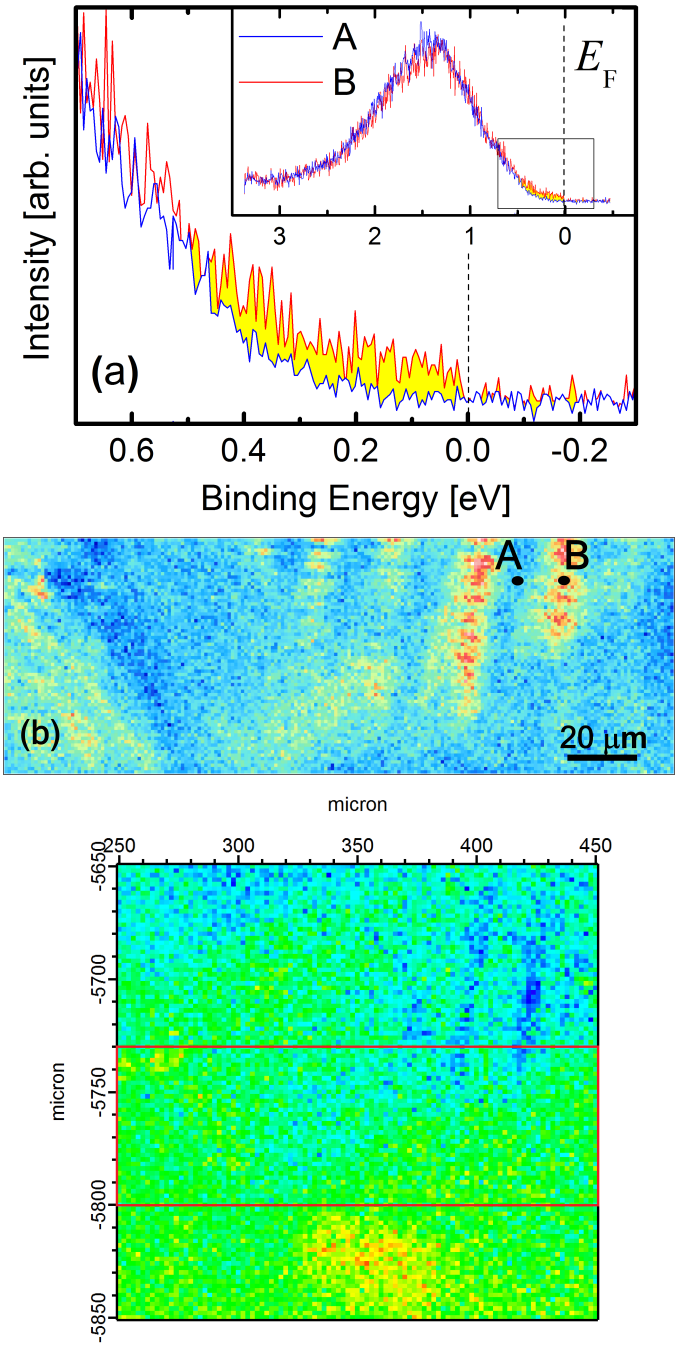

Figure 3.2: Spatially Resolved Photoemission Spectra of the Ti 3d band at 110K with sample orientation in [001]-direction. (a) Comparison between conducting and insulating spectrum in red and blue, respectively, at two different spots on the sample, denoted as 'A' and 'B'. (b) 200 μm $\times$ 70 μm cut-out of the spatially resolved and normalized Ti 3d band photoemission spectra. Side 'A' and 'B' are indicated by black dots. (c) Spatially resolved photoemission spectra of the Ti O 2p band at 110K with sample orientation in [001]-direction. The red rectangle marks the 200 μm $\times$ 70 μm cut-out of the spatially resolved and normalized Ti 3d band photoemission spectra shown in (b).

Mode	$YMnO_3$ Calc.	$YMnO_3$ Exp.	$YTiO_3$ Exp.	$Y_{0.63}Ca_{0.37}TiO_3$ LTM - phase
$A_g(7)$	104	151	145	
$A_g(5)$	147	188	168	
$A_g(2)$	223	288	273	
$A_g(6)$	304	323	314	294
$A_g(4)$	407	396	417	394
$A_g(3)$	466	497	446	457
$A_g(1)$	524	518	512	532
$B_{1g}(7)$	137	151	142	
$B_{1g}(5)$	162	220	219	
$B_{1g}(4)$	285	317	306	
$B_{1g}(6)$	393	341	328	
$B_{1g}(3)$	470	481	487	
$B_{1g}(2)$	583	537	521	
$B_{1g}(1)$	617	616	643	
$B_{2g}(5)$	145	178	151	
$B_{2g}(4)$	363	336	284	
$B_{2g}(3)$	390		366	342
$B_{2g}(2)$	476		452	494
$B_{2g}(1)$	610		678	637
$B_{3g}(5)$	181	205	162	
$B_{3g}(3)$	288	284	303	
$B_{3g}(4)$	342	384		
$B_{3g}(2)$	413		485	
$B_{3g}(1)$	593		644	593

Table 3.1: Calculated and experimentally obtained phonon modes of $YMnO_3$, [128] $YTiO_3$, [129] and the LTM phase of $Y_{0.63}Ca_{0.37}TiO_3$ measured at 10 K in $c(aa)\bar{c}$ geometry, respectively. The Raman shifts are given in units of cm^{-1}.

3.3.3 Spontaneous micro-Raman Spectroscopy

Various Raman investigations on $Y_{1-x}Ca_xTiO_3$ are available in the literature, showing that the Raman spectra are quite different between insulating (x < 0.33) and metallic (x > 0.39) samples at low temperatures. [129, 130] However, the phonon energies at room temperature do not change significantly by doping. This suggests, that mode assignments on $YTiO_3$ can be transferred to our doped material. [129] Phonon mode calculations are available for the perovskitelike $YMnO_3$. [128] As the Ti^{3+}/Mn^{3+} ions do not participate in the Raman active modes, no significant shift in the mode energies due to their different masses are expected. Table 6.1 shows the phonon energies for $YMnO_3$, both lattice dynamical calculations (LDC) and experimentally observed values compared to the experimentally obtained values for $YTiO_3$. [129] This shows that there is indeed a good overall agreement in energies of both materials. Finally, the Raman shifts of $Y_{0.63}Ca_{0.37}TiO_3$ obtained in this work from fits of the Raman spectra are also listed in Tab. 6.1. This comparison allows an explicit mode assignment of the observed phonon peaks. The Raman active modes for $Y_{0.63}Ca_{0.37}TiO_3$ in Pbnm symmetry are assumed to be $\Gamma = 7A_g + 5B_{1g} + 7B_{2g} + 5B_{3g}$. The Wyckoff positions are 4(c) for both Y and O1, 4(a) for Ti, and 8(d) for O2. But only Y, O1 and O2 yield Raman active modes. The Raman scattered light corresponding to A_g-modes retains the polarization of the incoming light, refereed to in experiment as *parallel polarization*, while for the B_{1g}-,B_{2g}-, and B_{3g}-modes, the polarization changes with the Raman process, thus these are observed in *cross polarized* geometry. The phase transition from Pbnm to $P2_1/n$ preserves the total number of modes, because the primitive cell is the same in both phases and inversion symmetry is not broken. However, this transition leads to a redistribution of orthorhombic B_g-modes to monoclinic A_g ones. Therefore, the polarization dependence of the Raman modes can be used to identify the crystallographic phase of the material. Fig. 3.3a) shows the Raman spectra in c(aa)$\bar{c}$ geometry at 10 K, obtained from two different spots on the sample, corresponding to distinct phases, as described above in the optical microscopy section. Significant differences are visible in the spectral weights and peak positions of the Raman spectra obtained from the bright and dark phases, respectively, see Fig.3.1a. The energy regions at ∼310, ∼390 and ∼640 cm^{-1}, denoted as P1, P2, and P3, respectively, exhibit the most prominent differences between the two phases. As reported in Tsurui et *al.* (2004), [129] the modes P1 and P2 are fingerprints of Raman spectra obtained from conducting samples with doping level $x > 0.39$, while P3 is only visible for doping levels $x < 0.39$, thus belonging to the insulating phase. Therefore, the Raman spectra allow us to identify the darker areas of the sample in Fig. 3.1a, as the LTO phase, represented by P1 and

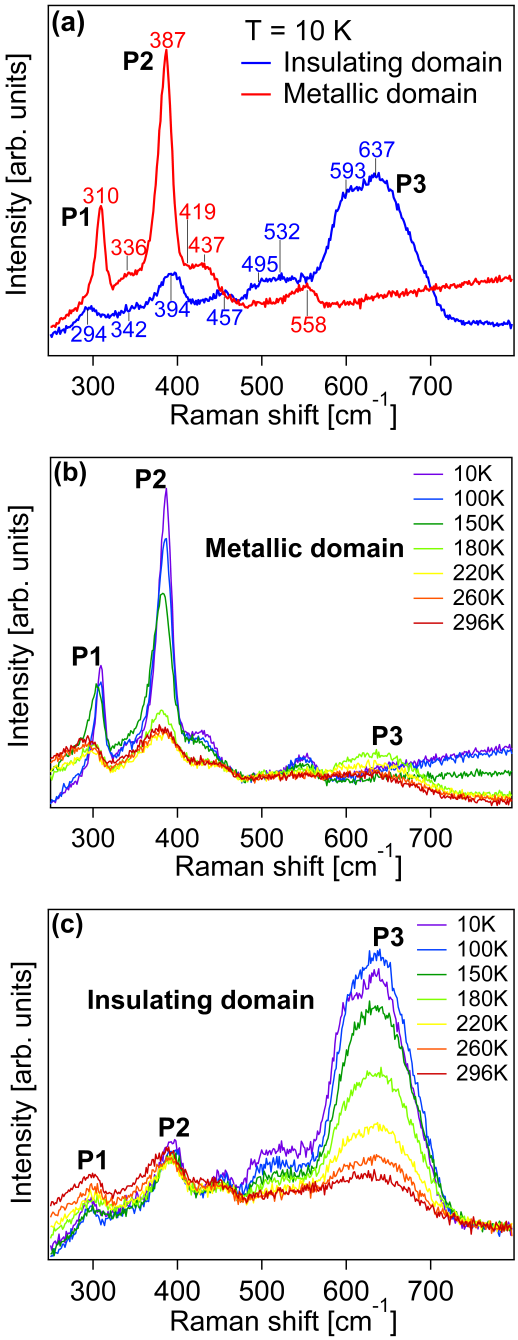

Figure 3.3: (a) Raman scattering spectra of $Y_{0.63}Ca_{0.37}TiO_4$ single crystal, measured for dark and bright spots, shown in Fig. 3.1a, in $c(aa)\bar{c}$ geometry at 10 K. The spectrum in blue is obtained from a bright area, while the spectrum in red is obtained from a dark area. (b) and (c) temperature evolution of the Raman spectra of the dark and bright domains, respectively.

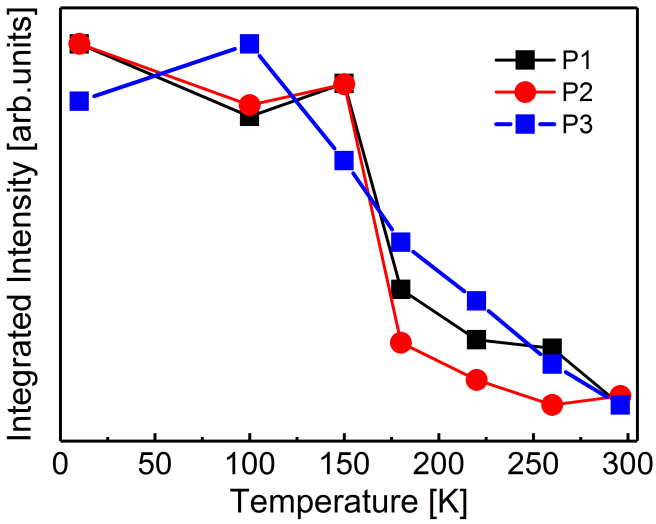

Figure 3.4: Temperature evolution of the normalized integrated peak weights of the metallic (red and black) and insulating (blue) domains, represented by the peaks P1, P2, and P3, respectively.

P2, and the brighter areas as the LTM phase, represented by P3. Fig. 3.3b and c show the temperature dependence of the spectra for spatially fixed positions in conducting and insulating regions, respectively, in the range from 10 K to room temperature. Of particular interest is the feature P3, which is strongest in the insulating domain at 10 K. The polarization geometry and the calculated frequencies from the literature suggest that the feature consists of the $B_{2g}(1)$ breathing mode and of other bond-stretching modes. These become Raman active in parallel polarization in the monoclinic phase and show a strong temperature dependence. Note, that the structural distortions, the modulation of the Ti-O bond distances, associated with orbital and charge ordering, are remarkably strong in these titanates, [125] which may explain the strong signal of the P3 feature as well as the strong temperature dependence.

Following the temperature evolution of P3 from room temperature to 10 K, the peak weight continuously increases and saturates between 100 K and 150 K, see Fig. 3.4. Such a saturation behavior is also observed for the static G-type distortion pattern associated with the charge and orbital order of the LTM phase. [125] This similarity in saturation behavior indicates, that the $B_{2g}(1)$ modes become A_{1g} modes, which correspond to the static distortions of the LTM phase. As the unit cell volumes of LTO and LTM phases differ, strain plays an important role in the phase separated state, which has been reported in TEM measurements: [124] it has been observed that especially the LTO phase is highly strained in contrast to the LTM phase, which will

favor phase separation.

The Raman spectra in the conducting domain show an abrupt change between 150 K and 180 K. This is especially seen in the peak weights of P1 and P2, shown as black and red curves in Fig. 3.4 Both modes require a description by an asymmetric Fano lineshape in the fits, which may hint to an enhanced coupling of the charge carriers to the phonon modes P1 and P2.

At room temperature, the spectra in the different regions of the material are almost identical, in agreement with the observation that in the microscope images the contrast between them is barely detectable.

3.4 Conclusions

Combining our results from optical microscopy, spatially resolved photoelectron spectroscopy, and Raman scattering, we can identify regions of different crystallographic and, in turn, electronic character in the material, which form stripe-like domain patterns of typical sizes of order $20 \times 100\,\mu\text{m}^2$. Along the direction of the stripes, these domains can extend up to several hundreds of μm. The result of our investigations of $Y_{0.63}Ca_{0.37}TiO_3$ allow us to assign the bright domains, see Fig. 3.1a, to be insulating and the dark domains to be conducting by using Raman spectroscopy. The insulating domains are furthermore identified with the LTM phase and the conducting domains with the LTO phase of the material. With these identifications, the optically observed percolation of the dark domains is indeed a percolation of the metallic LTO phase through the insulating LTM phase, which in the end leads to the macroscopic effect of a temperature-driven metal insulator transition. The domain patterns and the growth direction of the domains with varying temperature also explains the anisotropy observed in the resistivity. [129] As seen in the optical microscope pictures in Fig. 3.1, the three differently oriented surfaces exhibit a preferred growth direction of the metallic domains in a- and c- directions. However the growth in b- direction is strongly suppressed. Resistivity measurements along a- and c- directions in the literature indeed show a temperature-driven metal to insulator transition, whereas in b- direction the MIT is strongly suppressed. [129] Different transition temperatures with varying stoichiometries (x=0.37-0.39) are reported in the literature. [121,125] We attribute this to a faster percolation due to the higher number of metallic domains, and vice versa. In turn, the apparent natural inhomogeneity in the material is expected to result in spatially varying physical properties like transition temperatures. The reason for the stability of the insulating phase at high temperatures is still unclear and remains an

open question.

In summary, we have performed microstructural measurements using optical microscopy, spontaneous micro-Raman scattering, and micro-photoemission on single crystals of $Y_{0.63}Ca_{0.37}TiO_4$ in a temperature range from 10 K to room temperature. We observe a phase separation throughout the temperature range and identify the structural and the electronic differences between the different domains as well as their temperature dependence. Our results suggest that the macroscopic change of the electronic transport behavior is a result of percolation of the conducting LTO phase inside a non conducting phase, which at high temperature has an orthorhombic crystal structure, but at low temperature becomes monoclinic.

3.5 Acknowledgments

The here presented chapter has been published in

R. German, B. Zimmer, T. C. Koethe, A. Barinov, A. C. Komarek, M. Braden, F. Parmigiani, and P. H. M. van Loosdrecht,
"Temperature dependent percolation mechanism for conductivity in $Y_{0.63}Ca_{0.37}TiO_4$ revealed by a microstructure study,"
Materials Research Express, **5**, 126101, 2018.

The Raman measurements were performed by B. Zimmer and me, as well as the analysis of the data. The optical microscopy images were taken by B. Zimmer. The Micro-photoemission spectra were measured by T. Koethe and me, under the guidance of S. Barinov at the synchrotron Elettra, Trieste, Italy. The data was analysed by T. Koethe and me. The manuscript was written by myself in collaboration with the co-authors, especially T. Koethe. I gratefully acknowledge the fruitful discussions with C. Schüßler-Langeheine and D. Khomskii.

Chapter 4

Current influenced lattice vibrations of Ca_2RuTiO_4

We combine Raman light scattering and X-ray diffraction experiments with density functional theory calculations to study the impact of the metal-insulator transition driven by either temperature or electric field on the lattice dynamics in Ca_2RuO_4. Comparing the polarization dependent Raman spectra with the *ab-initio* lattice dynamics calculations we obtain good agreement concerning the frequencies and we can thus identify the character of the individual Raman-active modes. Current-dependent Raman measurements were performed at current densities, where the sample temperature can be kept constant, as it is confirmed by the Raman anti-Stokes/Stokes intensity ratios. Our data agree with a highly nonhomogeneous state and with a strong role of local distortions.

4.1 Introduction

Ca_2RuO_4 has attracted considerable interest as a Mott-insulating analogue [131–133] of the unconventional superconductor Sr_2RuO_4 [134]. The smaller ionic radius of Ca^{2+} compared to Sr^{2+} implies strong structural distortions associated with a tilt, a rotation and also flattening of the RuO_6 octahedron [135, 136]. These distortions reduce the electronic band width thereby enhancing the impact of electronic correlations [137] while the overall electronic state is similar in both ruthenates with 4 electrons occupying the Ru $4d$ t_{2g} states. In general there is consensus about a strong polarization of the orbital occupation with almost completely filled d_{xy} states in Ca_2RuO_4 [138–145], while in Sr_2RuO_4 the orbital occupation of each of the three d_{xy},d_{xz} and d_{yz} amounts to $\sim$4/3. However, the role of spin-orbit coupling in Ca_2RuO_4 remains matter of debate.

It was proposed that spin-orbit coupling in Ca_2RuO_4 is sufficiently strong to induce a non-magnetic state and van-Vleck type excitonic magnetism [146] while the strong flattening of the RuO_6 octahedron and the resulting orbital polarization point to a more conventional picture. The magnon dispersion [147] disagrees with predictions of the excitonic model [148] and can be very well described within a spin model with highly anisotropic parameters [149]. In excellent agreement recent ARPES studies [150] and DMFT calculations [139, 140] find almost complete orbital polarization. In addition the calculated magnetic interaction parameters describe the experimental magnon dispersion very well including a longitudinal mode [140, 149, 151]. Therefore, treating the spin-orbit coupling in Ca_2RuO_4 in a perturbative manner seems adequate.

Ca_2RuO_4 exhibits a metal-insulator transition upon cooling below T_{MI}=357 K [132, 136, 152] which is accompanied by flattening of the pseudo-tetragonal lattice and the RuO_6 octahedron. Due to the rotation of the octahedron around the vertical axis and due to an additional tilting the symmetry is lower than that in tetragonal Sr_2RuO_4 (space group I4/mmm) and is described in space group Pbca (D_{2h}^{15}), but the symmetry of the crystal structure does not change at T_{MI} [135, 136]. The insulating phase is characterized by a reduced c lattice parameter inspiring the labeling S phase in contrast to metallic Ca_2RuO_4 with a longer c parameter, labeled L phase. The strong structural changes between the low-temperature S and high-temperature L phases are not restricted to the MIT but occur on a broad temperature range from T_{MI} down to the antiferromagnetic ordering temperature T_N=110 K [135, 136, 153], below which the Ru^{4+} ($4d^4$) ion spins point along the orthorhombic b axis [135].

The insulating state in Ca_2RuO_4 appears rather unstable and can easily be suppressed by electronic doping, i.e. La substitution [154], by isovalent substitution $Ca_{2-x}Sr_xRuO_4$ [155], by applying pressure [153, 156] and even by applying a moderate electric field of the order of only 40V/cm [157]. In contrast typical Mott insulating states break down only at much higher electric fields [158]. The electric-field induced metallic state persists upon cooling the sample to low temperature and has been studied by various methods [159–167]. The report of strong diamagnetism and anomalous transport properties of current-carrying Ca_2RuO_4 crystals at low temperature [164] further increased the interest in this metallic state, but the strong diamagnetism reported for the current-induced phase turned out to arise from an experimental artefact [168]. Neutron and X-ray diffraction experiments indicate that at moderate current densities there is at most a minority metallic phase present at low temperature, while a new phase with an intermediate effective c lattice constant is observed that was attributed to microscopic phase mixture [165]. Already the S-shaped characteristic line presenting

current versus voltage indicates an inherent instability towards phase coexistence [165], which is also observed in infrared experiments [160]. Such tendency towards phase coexistence will be enhanced through the strong relative strain of the S and L phases, as it is typically observed for martensitic phase transitions [165,169,170]. A stripe pattern of alternating metallic and insulating regions was observed by scanning near-field optical microscopy [160]. Due to the phase coexistence of metallic current-carrying parts with insulating ones the definition of the temperature becomes very delicate and in particular for large current densities of the order of several 10 Acm^{-2}, proper assessment of the temperature seems to be impossible and the temperature can vary locally [165, 166].

The scope of this work is to study the current- and temperature-induced metal-insulator transition in $Ca_2Ru_{0.99}Ti_{0.01}O_4$ and in particular its impact on the local structure. We combine Raman scattering experiments for T $\approx$ 10 - 360 K and current densities J = 0 - 12 Acm^{-2} with density-functional-theory (DFT) calculations of the lattice dynamics and with temperature dependent X-ray diffraction studies. Raman scattering offers the opportunity to investigate locally the current induced mechanisms under current heating. To minimize Joule heating, the relevant experiments were conducted at current densities of less than $\sim$ 15 Acm^{-2}. The reported experiments show that a sharp drop of the resistivity and a change of the Raman detected phonons take place at $\approx$ 1.3 Acm^{-2} and $\approx$ 3.5 Acm^{-2}, respectively. These current-induced behaviors suggest that local distortions in the crystal matrix are essential. In particular, phonon modes assigned to the A_g symmetry reflect the bare current-induced ionic displacements. Disentangling local structural mechanisms from long-range order effects is mandatory for the interpretation of current driven insulator-metal transitions in Ca_2RuO_4. Additionally, strong electron-phonon coupling is derived by Fano-like phonon asymmetries.

4.2 Experimental

The $Ca_2Ru_{0.99}Ti_{0.01}O_4$ crystals were grown by the floating-zone method as discussed in Refs. [149, 171, 172]. A small amount of Ti (slightly above 1 percent) was added in two of the three crystal growths discussed here, as this was found to yield larger crystals, which are more stabel on cycling through the first order structural phase-transition than the non Ti-substituted ones. Similar observations were made for Mn substitution [167]. The full determination of the crystal structure by X-ray single-crystal diffraction on comparable crystals indicated that the inserted amount of Ti is slightly higher, because Ru evaporates during the crystal growth [149]. Temperature dependent X-ray

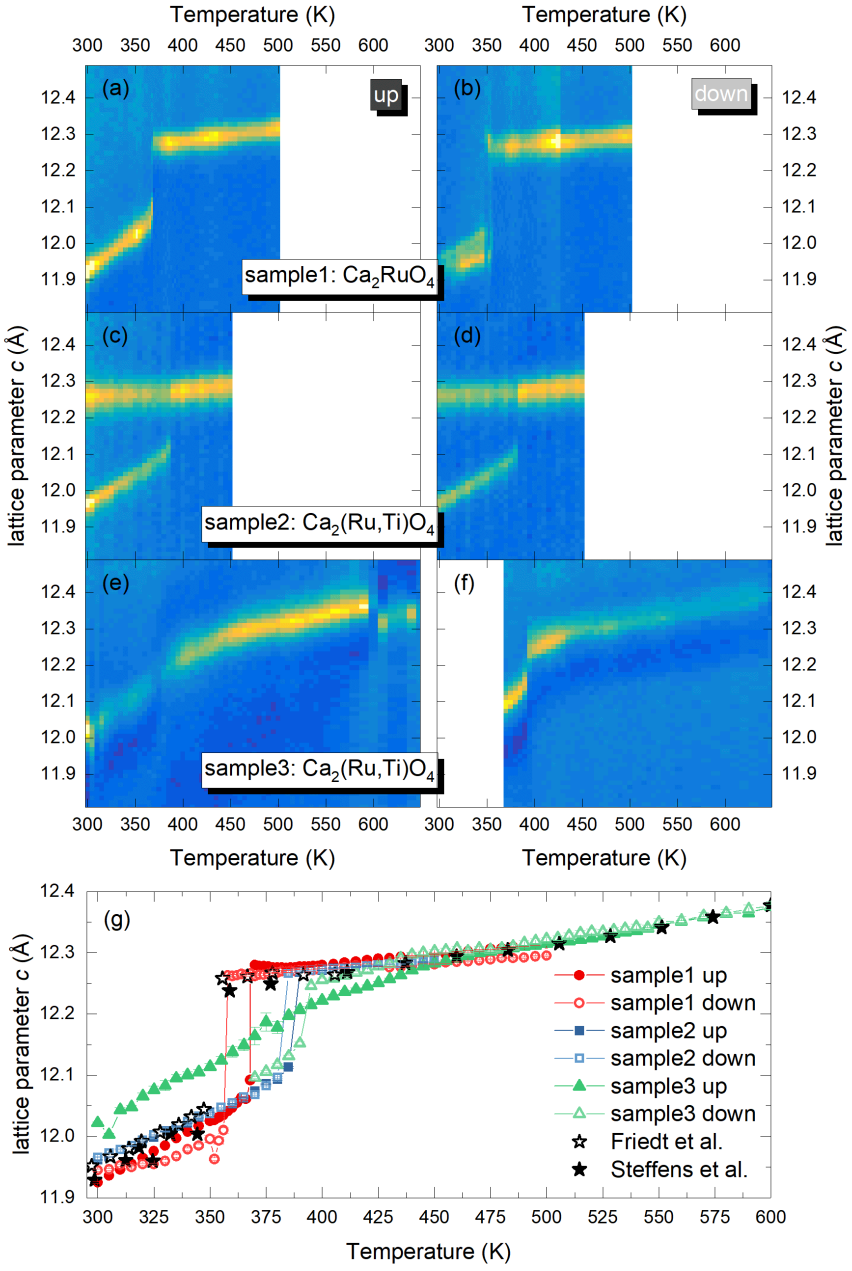

Figure 4.1: Temperature dependence of the lattice parameter c as visualized through the (006) Bragg peak. The 2Θ angles were transformed into the lattice parameter plotted as vertical axis. Panels (a)-(f) show data taken while ramping the temperature up (left panels) and down (right panels) with three different single crystals. In panel (g) we compare the single-crystal results with previous studies on polycrystalline samples [136, 153].

diffraction experiments were performed on a D5000 powder diffractometer in Bragg-Brentano geometry (Cu K_α radiation) by scanning along the c lattice parameter.

The spontaneous Raman measurements were performed by a continuous wave solid-state laser of 532 nm wavelength using crystals containing the small amount of Ti. The samples were fixed by varnish on a sapphire support glued to a copper sample holder and adapted to a temperature controlled system suitable for optical spectroscopy and electrical resistivity experiments from LHe to 360 K. The current in the Raman spectroscopy experiments was applied along the a-axis and measured by a two-point probe method due to experimental limitations. The more reliable four-point probe was carried out separately and is compared with the results in the Appendix. Hence, the absolute values of our transport measurements will be affected by the systematic errors associated with parasitic voltage drops. The Raman spectra were collected by using a triple grating spectrometer operating in subtractive mode and equipped with a LN_2 cooled CCD camera and a final resolution of 1 cm^{-1}.

4.3 Results

4.3.1 X-ray Diffraction Experiments of the C Lattice Parameter

We mounted three single crystals of $Ca_2Ru_{1-x}Ti_xO_4$ with nominal Ti content of 0 and 0.01 on a powder diffractometer. The plate-shaped crystals can perfectly replace the area sample used in Bragg-Brentano geometry yielding high statistics but limiting the accessible Bragg reflections to (00l). The temperature dependent results of the c lattice constants are shown in Fig. 4.1, where data are normalized at 600 K and compared to previous results obtained by powder neutron [136] and powder X-ray [153] experiments. The c parameter strongly varies with temperature. Due to the onset of tilting at T_S=650 K there is pronounced shrinking of the c lattice constant between T_S and T_{MI} by ∼0.0005 Å/K. At the metal-insulator transition c abruptly shrinks by roughly 0.2 Å and in the insulating phase the temperature dependent shortening is even stronger, ∼0.002 Å/K. In the insulating phase the shrinking partially stems from a larger tilting and partially from the change in the orbital occupation [173].

It is obvious that the Ti content slightly shifts the metal-insulator transition to higher temperatures as already concluded in reference [149]. For samples 1 and 2 there is only a small hysteresis between up and down ramping the temperature, but the data obtained upon increasing temperature on sample 3 do not reveal the abrupt

changes in the lattice constants but a smoother increase upon heating. We attribute this behavior to a microscopic phase coexistence as discussed for the current induced changes in [165]. Also the strong uptake of c in the neutron powder diffraction data close to the transition [136] points to local structure effects occurring even in the powder samples. The strong strain between metallic and insulating phases must facilitate non-homogeneous phases close to the transition [165, 169, 174]. Single crystals are grown from the melt and rapidly cooled through the metal-insulator transition which can freeze a non-equilibrium state. We suppose that in sample 3 a mixture of metallic and insulating regions was quenched which results in a c lattice parameter in between those of the metallic and insulating phases. Only after heating above T_{MI} long range metallic and insulating regions evolve.

4.3.2 Raman Spectroscopy

$Ca_2Ru_{0.99}Ti_{0.01}O_4$ crystallizes in the orthorhombic Pbca (61) space group. The associated Wykoff positions are 4a for Ru^{4+}, and 8c for Ca^{2+}, O_1^{2-}, and O_2^{2-} [135], but only 8c positions imply Raman active phonon modes. There are four formula units in the primitive unit cell for Ca_2RuO_4, which translates to 84 phonon modes at each propagation vector. The lattice dynamics of Ca_2RuO_4 is thus much more complex than that in Sr_2RuO_4 for which the entire phonon dispersion was studied by inelastic neutron scattering experiments [175] and DFT calculations [176] yielding excellent agreement for most of the branches.

The $\Gamma-$point phonons reduce to the following irreducible Raman active representations [177]:

$$\Gamma = 9A_g + 9B_{1g} + 9B_{2g} + 9B_{3g} + 12A_u + 12B_{1u} + 12B_{2u} + 12B_{3u}. \tag{4.1}$$

Excitations in A_g and B_{1g} geometry are probed by parallel and crossed polarized light, corresponding to $c(ab)\bar{c}$ or $c(ba)\bar{c}$, and $c(aa)\bar{c}$ or $c(bb)\bar{c}$, in Porto notation, respectively.

4.3.2.1 Phonon Excitations

Fig. 4.2 shows the Raman active excitations of $Ca_2Ru_{0.99}Ti_{0.01}O_4$ in the frequency range of 100 - 1500 cm^{-1}, detected in A_g geometry at 10 K, and labeled as A1-A20. Fig. 4.3 presents the calculated polarization vectors and Fig. 4.4 compares the Raman signals in in A_g geometry with the excitations detected in B_{1g} geometry, labeled as

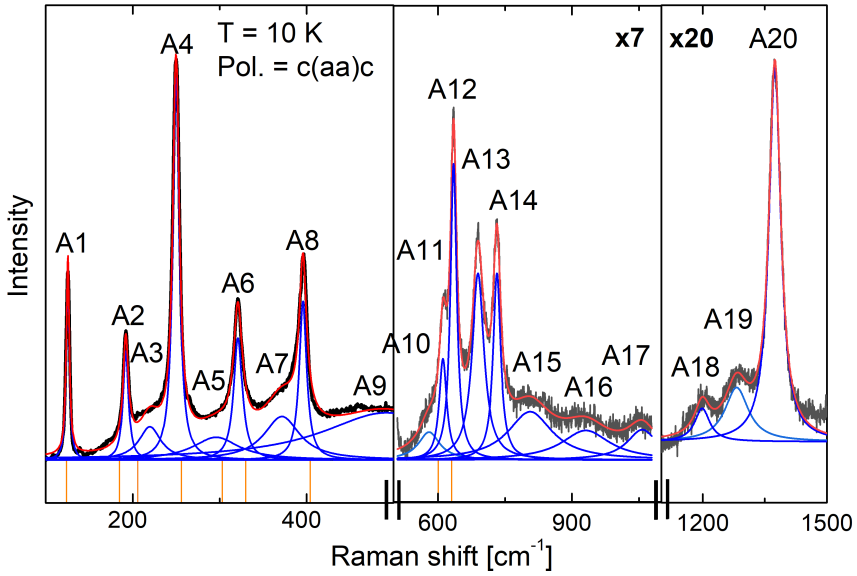

Figure 4.2: Raman spectra of $Ca_2Ru_{0.99}Ti_{0.01}O_4$ at 10 K in c(aa)c geometry (black) together with the Lorentzian fits (blue), denoted as A1-A20, and the resulting envelope (red). Calculated values are presented as orange bars.

B1-B16. In order to assign these features to the proper phonon mode we calculated the phonon frequencies and polarization patterns by density functional theory (DFT) with finite differences method implemented in pseudopotential VASP code [178], and the Perdew-Burke-Ernzerhof (PBE) exchange-correlation potential [179]. A plane-wave cutoff energy is set to 500 eV. The on-site Hubbard repulsion and intra-atomic Hund's rule exchange are taken to be U= 3 eV and J_H = 0.7 eV [149, 180, 181] in GGA+U calculations. The AFM order is assumed in the calculations for the insulating phase. We performed calculations with crystal structure of the S phase at 10 and 300 K [135] and with that of the L phase at 400 K [136]. The mode assignment is done by the analysis of the eigenvectors of the obtained dynamical matrix. The calculated frequencies are compared to Raman data in Table 4.1 and the corresponding polarization patterns of the A_g modes are shown in Fig. 4.3.

All Raman features detected in A_g symmetry are fitted by Lorentzian oscillators, presented in blue in Fig. 4.2. The agreement between DFT calculations [176] and the experimental phonon dispersion in Sr_2RuO_4 [175] is excellent with only minor deviations pointing to some anomalous electron phonon coupling. Therefore, the comparison of the Raman low-temperature data with DFT calculations for the S phase at 10 K can be used to unambiguously identify the A_g and B_{1g} modes in Ca_2RuO_4, see Table 4.1.

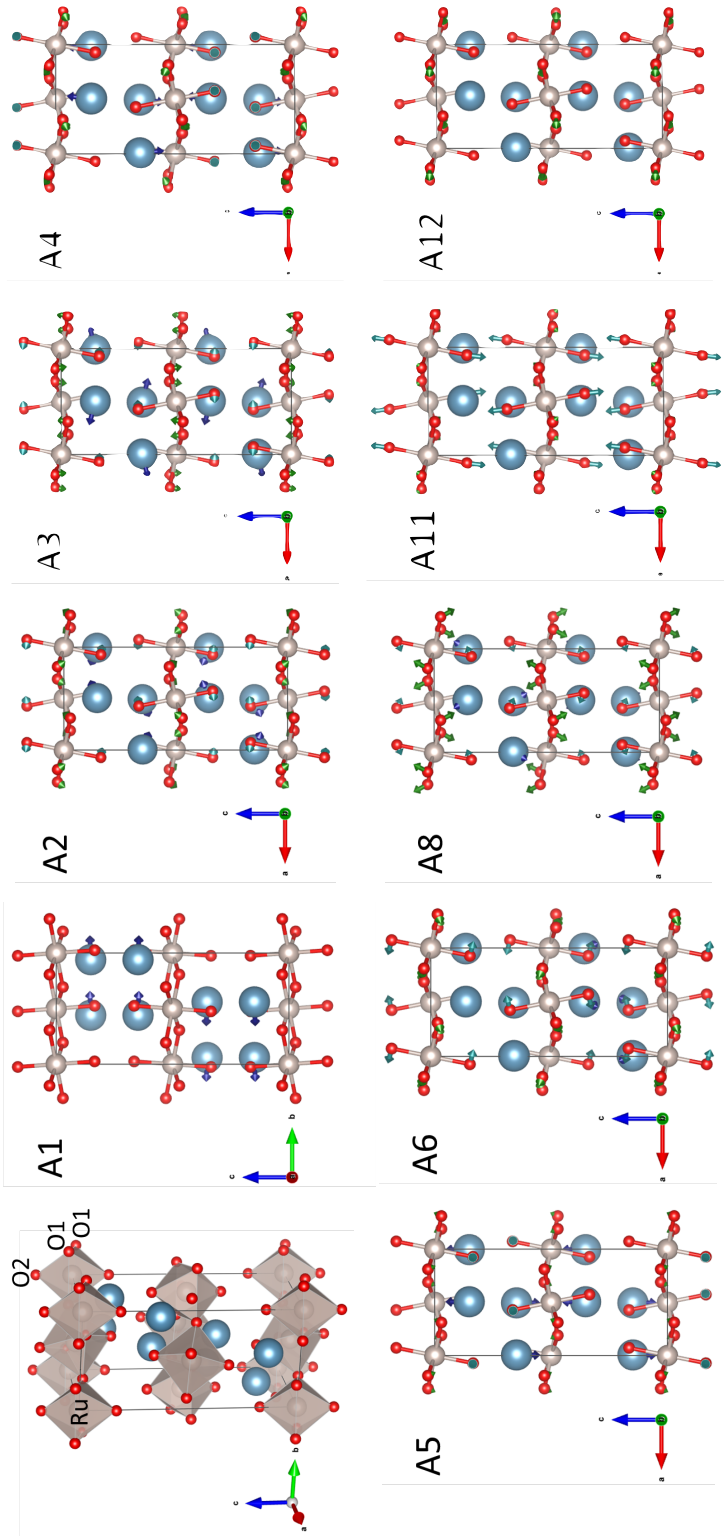

Figure 4.3: Sketch of the $Ca_2Ru_{0.99}Ti_{0.01}O_4$ crystal structure and the ion displacements for the 9 calculated A_g phonon modes A1-A6, A8, A11, A12.

		DFT calculation					Raman	at ∼10 K
A_g/B_{1g}	label	L 400 K	S 300 K	S 10 K	$\frac{\Delta\nu}{\nu}$ 300 K	$\frac{\Delta\nu}{\nu}$ 10 K	ref. [177]	here
B_{1g}	B12/A13	727.4	676.0	662.5	-7.1	-8.9	683	691.7
A_g	A12	666.6	640.7	627.9	-3.9	-5.8	-	634.4
A_g	A11	552.8	569.7	600.3	3.1	8.6	607	611.0
B_{1g}	B9	481.0	482.4	514.3	0.3	6.9	534	518.4
A_g	A8	391.9	407.6	404.5	4.0	3.2	395	395.7
B_{1g}	B8	419.2	397.5	461.5	-5.2	10.1	459	461.0
B_{1g}	B6	345.9	352.5	381.0	1.9	10.1	388	388.2
A_g	A6	320.5	311.9	329.3	-2.7	2.7	322	321.1
B_{1g}	B4	286.1	281.3	287.3	-1.7	0.4	292	294.5
A_g	A5	271.5	276.6	302.9	1.9	11.6	304	(295.9)
B_{1g}	B3	267.6	264.2	263.6	-1.3	-1.5	269	266.9
A_g	A4	227.9	250.8	256.5	10.0	12.5	251	249.8
B_{1g}	B3	233.4	242.7	255.8	4.0	9.6	265	266.9
B_{1g}	B2	175.4	202.3	225.9	15.3	28.8	215	211.8
A_g	A3	204.7	198.2	206.0	-3.2	0.6	204	(219.7)
A_g	A2	176.1	174.5	185.2	-0.9	5.2	192	192.0
B_{1g}	B1	119.4	131.0	133.7	9.7	12.0	140	139.5
A_g	A1	95.2	118.0	124.2	23.9	30.5	126	125.4

Table 4.1: Comparison of the Raman-active A_g and B_{1g} modes in Ca_2RuO_4. The Raman data of reference [177] and our data are compared to our DFT calculation with different crystal structures. All frequencies are given in cm^{-1} and relative frequency changes compared to the calculation for the L phase at 400 K are are given in percent. At 10 K the frequencies of modes A3 and A5 cannot be unambiguously determined and values are set in parentheses.

Our identification mostly agrees with that proposed in reference [177], where, however, a feature at 356 cm^{-1} was attributed to an A_g mode while the two highest A_g modes could not be separated. There are additional features observed which are not covered by the phonon calculations in A_g geometry. In particular there is a broad continuum above 200 cm^{-1} that was already reported by Souliou et *al.* [182] and that evolves upon entering the magnetically ordered state. This continuum seems to extend to above 600 cm^{-1} in agreement with an interpretation as two-magnon continuum and the width of the magnon dispersion observed in inelastic neutron scattering experiments [149, 151]. For the modes A1-A6, A11, and A12 no obvious asymmetric line shapes are observable. Only A8 shows a small asymmetric shoulder, which we attribute to an extra excitation A7, lying at $\approx$ 370 cm^{-1}. The origin of this mode is not clear, it can arise from a feature in the two-magnon density. Furthermore, A7 is also visible as a weak shoulder in B_{1g} geometry. Symmetry leaking induced by defects and local distortions of the lattice could lead to additional visible modes in one or the other geometry. Therefore, the numerous B_{1g}, B_{2g}, and B_{3g} modes could leak into the A_g spectrum. This could be also the case for the broad excitation A9, where the temperature dependence in Fig. 4.5 (black dots) and the B_{1g} geometry suggest underlying modes. The modes A13 - A20 are mainly visible in both geometries, whereas A13 could be assigned by the phonon mode calculation to a B_{1g} mode. The origin of the features A14- A19 is not clear, but we suggest that they are due to multi-phonon excitations. The highest of these frequencies perfectly matches twice the highest Raman active mode observed, see Table 4.1. A20 is strongly temperature dependent and disappears at $\approx$ 200 K, reported also in Ref. [183]. This mode A20 is controversially discussed in the literature and interpreted by the authors as orbital wave. Comparison with similar systems, like e.g. $LaMnO_3$, suggests the mode A20 to be multi-phonon scattering [184].

Fig. 4.4 compares the A_g Raman data with the results obtained for the B_{1g} geometry for a temperature of 10 K. The B_{1g} data were also fitted by several Lorentzian oscillators thereby determining the mode frequencies given in Table 4.1. The B_{1g} geometry mode at $\sim$110 cm^{-1} was observed in many Raman studies and designated to a magnetic excitation. With the inelastic neutron scattering study determining the lowest magnon energy at 13.2 meV=106 cm^{-1} [147] it is obvious that this excitation does not correspond to the typical two-magnon feature. Instead it is the single magnon at the antiferromagnetic zone center that becomes Raman active due to the strong spin-orbit coupling in Ca_2RuO_4 [147]. Due to the orthorhombic symmetry and the magnetic moment being aligned along orthorhombic b there are two separate magnon modes at the antiferromagnetic zone center whose finite energies arise from the mag-

netic anisotropy and thus spin-orbit coupling. For the layered system the rotation of the ordered moment within the RuO_2 layers is expected to reveal a lower energy, but even this mode appears at a rather high frequency of 106 cm^{-1} [147] perfectly corresponding to M1. The other anisotropy mode associated with rotating the moment out-of-plane exhibits a remarkably high energy reflecting the strong flattening of the RuO_6 octahedron and the associated orbital polarization. This mode is found at 45.5 meV=364 cm^{-1} in neutron scattering studies [149, 151] and again a weak Raman B_{1g} response (mode B5 as a shoulder of B6) is detected at this frequency. The feature M2 at 71 meV=570 cm^{-1} in B_{1g} geometry is also of magnetic origin because it rapidly disappears upon heating; it furthermore agree with a finding in reference [182] but it cannot be identified. There is no evidence for a longitudinal mode expected to appear at 40 meV=320 cm^{-1}. From the comparison with the DFT calculation and with previous Raman experiments [177] we deduce that the feature B3 contains two different B_{1g} modes that are nearly degenerate.

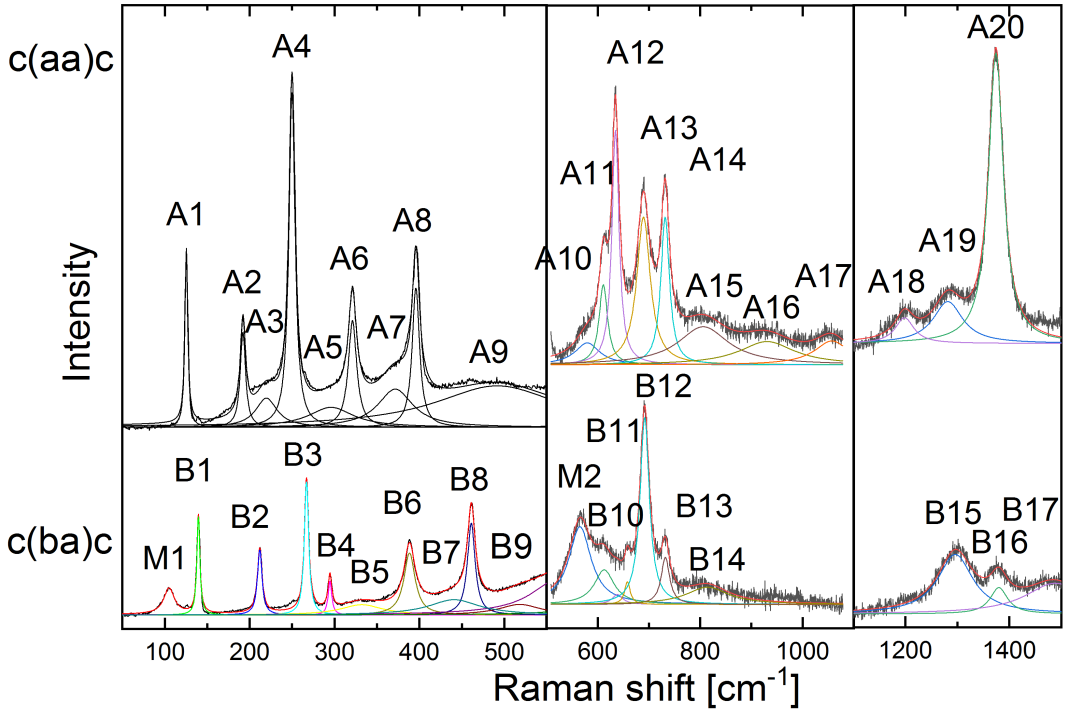

Figure 4.4: Raman spectra of $Ca_2Ru_{0.99}Ti_{0.01}O_4$ at 10 K in c(aa)c- and c(ba)c- geometry and the fitted sum (red). The fitted oscillators (blue) are denoted by the letters A1-A20 and B1-B17, corresponding to c(aa)c and c(ba)c, respectively.

In the following we focus on the A_g phonon modes A1 - A6, A8, A11, and A12 in the

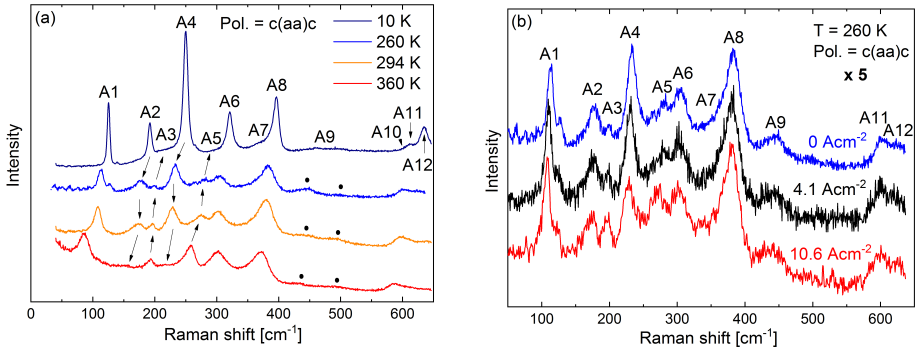

Figure 4.5: Raman spectra of $Ca_2Ru_{0.99}Ti_{0.01}O_4$ at (a) 10 K (blue), 260 K (purple), 294 K (orange), and 360 K (red), in c(aa)c geometry. A1- A12 denote the phonon modes as introduced in Fig. 4.2. Black dots show the possible modes contributing to A9. Arrows indicate the gain or loss of intensity upon variation of temperature. (b) Raman spectra of $Ca_2Ru_{0.99}Ti_{0.01}O_4$ at the 260 K with a applied current density of 0 Acm^{-2} (blue), 4.1 Acm^{-2} (black), and 10.6 Acm^{-2} (red). The spectra are enlarged by a factor of 5 in respect to the spectrum at 260 K in (a).

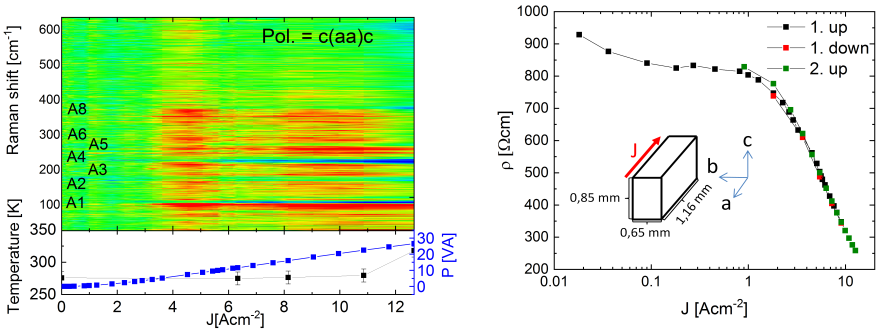

Figure 4.6: (a) Current induced Raman spectra of $Ca_2Ru_{0.99}Ti_{0.01}O_4$. All spectra are subtracted by the Raman spectrum at 0 Acm^{-2}. At the bottom the temperature (black), calculated by the Raman intensities ,and the calculated Joules power (blue) is presented. (b) The corresponding resistivity at 260 K for several cycles (black, red, green). The inset sketches the sample dimensions and the direction of the applied current.

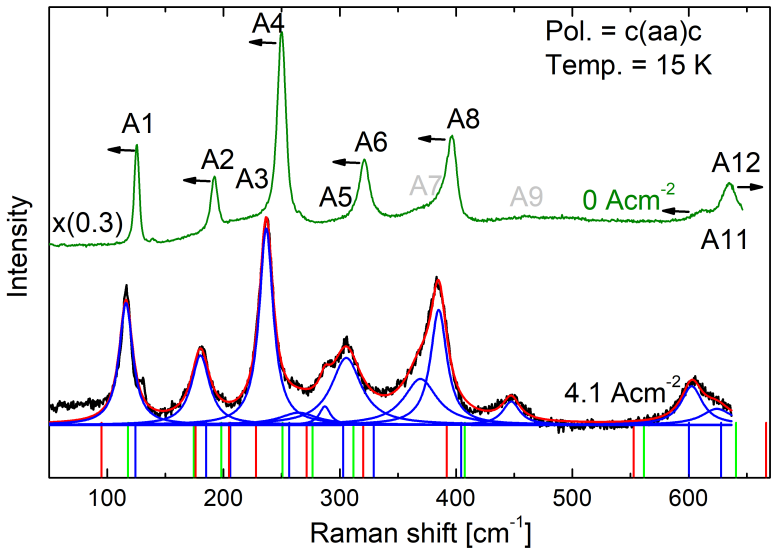

Figure 4.7: Raman spectra of $Ca_2Ru_{0.99}Ti_{0.01}O_4$ at 15 K for 0 Acm^{-2} (green) and 4.1 Acm^{-2} (black) current density. The fitted Lorentzian oscillators and their sum are presented in blue and red, respectively. The calculated phonon energies are indicated by red (for L phase at 400K) and by blue and green vertical bars for the S phase at 10 and 300 K, respectively. All calculated energies are given in Tab. I.

energy range of 50 - 650 cm^{-1}. Fig. 4.3 sketches the crystal structure and shows the corresponding A_g displacement patterns. The parameters in the polarization vectors of the A_g modes correspond to the free structural parameters of Ca, in-plane oxygen O1 and out-of-plane O2 positions in the Pbca structure. In the modes A1, A2 and A3 we find the parameters describing the tilting of the octahedron, which corresponds to the structural phase transition occurring at 650 K [153]. One may thus expect the hardened soft rotation mode among the A_g modes, but closer inspection of the patterns for A1, A2 and A3 indicates that the hardening of the rotational mode already results in a mixing of characters. While the lowest mode exhibits a strong Ca displacement the movements of the O2 and O1 are found in A2 and A3 respectively. In particular the lowest A1 mode exhibits a strong temperature dependence for heating to room temperature and for passing into the metallic phase, see Table 4.1. The metallic phase exhibits a smaller tilt distortion in perfect agreement with the softer rotational mode. Concerning the two highest A_g modes the interpretation is simple. Both are Ru-O bond-stretching modes, A_{11} corresponds to the vibration of the apical O2 in c direction and A_{12} is the in-plane stretching mode. These two modes can be taken as a probe of the flattening or elongation of the RuO_6 octahedra.

The temperature dependence of these A_g modes are presented in Fig. 4.5a. Especially the mode intensities of A2 (A3) and A4 (A5) decrease (increase) by increasing temperature, depicted by arrows in Fig. 4.5a. The frequencies and intensities of the highest two A_g modes exhibit an opposite temperature dependence. Due to the pronounced elongation of the RuO_6 octahedra with increasing temperature the out-of-plane mode A11 strongly softens while the in-plane mode A12 hardens. This splitting is further enhanced in the metallic phase, see Table 4.1.

In a similar way the modes A2 - A5 are affected when a current along the crystallographic a- axis is applied at a constant temperature of 260 K, see Fig. 4.5b. A systematic Raman study of the current induced effects between 0 - 12.5 Acm^{-2} is presented in Fig. 4.6a. All current induced Raman spectra are subtracted by the Raman spectrum at zero current. The map with the relative Raman intensity versus the current density is related to the effective local sample temperature and the current induced Joules power, presented at the bottom of Fig. 4.6a, and is deduced by the Raman anti-Stokes/Stokes ratio:

$$\frac{I_{AS}}{I_S} = \frac{(\nu_{laser} + \nu_{phonon})^4}{(\nu_{laser} - \nu_{phonon})^4} \exp^{-\frac{h\nu_{phonon}}{k_B T}}, \tag{4.2}$$

where ν_{phonon} and ν_{laser} are the frequencies of the phonon mode and the laser,

respectively, k_B is the Boltzmann constant, h denotes the Planck constant, and T indicates the temperature.

All Raman modes exhibit a significant change when the current density reaches ≈ 3.5 Acm^{-2}, suggesting a sudden local lattice distortion by a critical current density. However, the simultaneously measured resistivity, and the calculated Joule power, reveals a clear onset of the conductivity behavior at ≈ 1.3 Acm^{-2} as shown in Fig. 4.6a, b. Additional four-point resistivity measurements over several cycles and with current densities up to 100 Acm^{-2} revealed significant resistivity changes from one measurement to the other when $J \approx 10$ Acm^{-2} is exceeded, presented in SM Fig. 1. Thus, for high current densities the dissipated energy could contribute to the increase of the lattice temperature.

The Raman spectra recorded on ramping the current density up show a highly non-continuous behavior. While there is little change up to $\sim$3 Acm^{-2} the pattern at 4.1 Acm^{-2} exhibits important differences. For slightly higher current densities, however, the pattern looks more similar to that at zero current density. Another discontinuous change occurs around 8 Acm^{-2} while the data at the highest current densities again exhibit less differences. The Raman experiment does not probe the entire volume of the sample crystal as the penetration of the light is of the order of a μm, in addition only an area of 100μm$\times$100μm is covered by the beam. Therefore the non-continuous data support the inhomogeneity arising from ramping the current up. This is in agreement with a filamentary or percolative conductivity that was deduced from diffraction experiments [165]. Within the sensed volume near the surface different states will dominate. One should also consider the effect of the cooling by the contact with the He gas at the surface. The analysis of the Stokes anti-Stokes intensities was performed on the same data, see Appendix, so that we can estimate the temperature of the sensed part of the sample as it is indicated in the lower part of Fig. 5 (a). Even for the two abrupt changes in the Raman spectra the temperature does not essentially vary. This, however, cannot exclude that warmer and metallic parts exist deep in the crystal outside the volume sensed by the Raman experiment.

In order to investigate the increase of the sample conductivity by applying current, further experiments and phonon mode calculations were performed. Raman spectra for 0 Acm^{-2} (green) and 4.5 Acm^{-2} (black) at 15 K exhibit a clear red shift of the phonon modes, Fig. 4.7. All fitted Lorentzians modes (blue) are presented together with its sum (red). The comparison of the data taken at high current density and low temperature with the calculated positions of A_{1g} phonon frequencies (see Table 4.1) clearly shows that the data neither correspond to the insulating phase at much

higher temperature nor to the metallic phase above the metal-insulator transition. In particular for the bond-stretching modes much stronger shift are expected when passing into the fully metallic state.

4.4 Conclusion

In conclusion, we have used a combination of X-ray diffraction and Raman spectroscopy for studying the temperature and current-driven structural and electronic transport behavior of well characterized $Ca_2Ru_{0.99}Ti_{0.01}O_4$ single crystals. By comparing the Raman excitations with DFT calculations for the metallic and insulating phases of $Ca_2Ru_{0.99}Ti_{0.01}O_4$ we can identify the character of the A_g and B_{1g} modes and thereby unambiguously identify modes of magnetic origin. Some phonon modes exhibit a pronounced temperature dependency which are attributed to the structural changes occurring within the insulating phase and near the metal-insulator transition. We have observed a significant reduction of the sample resistivity for $J > 1.3$ Acm^{-2} but up to $J \approx 3.5$ Acm^{-2} the Raman emissions remain substantially unchanged. However, at $J \approx 3.5$ Acm^{-2} a sudden change of the Raman emission is taking place, while spectra taken at even larger current density are again more similar to the one without current. A similar effect is observed for current densities above $J \approx 8$ Acm^{-2}. Since the Raman experiment senses only a small volume close to the surface, these abrupt effects must be attributed to the inhomogeneous state that is induced by ramping the current up. In agreement with diffraction studies an inhomogeneous state seems to be unavoidable for moderate current densities and low temperatures. Overall finite current densities induce a red shift in most phonon frequencies resembling temperature increase and underlining that local structural distortions in an highly inhomogeneous state are the driving force for the current induced metal insulator transition.

4.5 Acknowledgments

The here presented chapter has been submitted to PR Materials

R. German, E. Komleva, S. Streltsov, K. Jenni, S. Kunkemöller, M. Braden, F. Parmigiani, and P. H. M. van Loosdrecht,
"Current-induced effects on the local structure and electrical transport behavior in Ca_2RuO_4 unveiled by Raman Scattering,"
PRM.

The Raman measurements were performed by myself, as well as the analysis and the interpretation of the data. The neutron and X-ray diffraction experiments were performed and interpreted by K. Jenni and M. Braden. The presented calculations were done by E. Komleva and S. Streltsov. The manuscript was written by myself in collaboration with the co-authors.

4.6 Appendix

4.6.1 Analyses of the Conductivity

Resistivity data of $Ca_2Ru_{0.99}Ti_{0.01}O_4$ containing a small amount of Ti were measured after the Raman spectroscopy experiments using the same sample crystal. Fig. 4.8a shows the comparison between two- and four-point method of this later conducted measurements. Until $J \approx 35$ Acm^{-2} the two methods give qualitatively the same results, but they strongly deviate for higher current densities. Repeating the resistivity measurements several times with the four-point method gives qualitatively the same results, but is not reliable regarding to their absolute values, see b). Additionally, voltage fluctuations were observed while the experiment was conducted, visible also in the data for higher current densities and hinting to a internal reorientation of charges. Nevertheless, for the current densities below ≈ 15 Acm^{-2}, used in the Raman experiments, the resistivity was repeatable. The temperature dependent resistivity shows comparable behavior with the literature. The Raman spectra do not show significant intensity drops until ≈ 10 Acm^{-2}, see Fig. 4.9c).

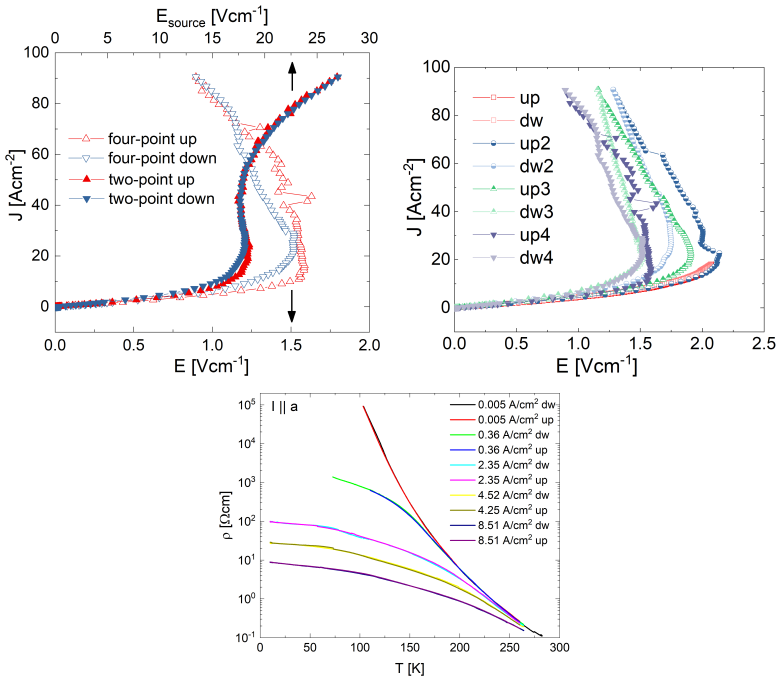

Figure 4.8: Current dependent resistivity measurements for $Ca_2Ru_{0.99}Ti_{0.01}O_4$ at 260 K. (a) Comparison between 2- and 4- point method and (b) consecutive cycles up to ≈ 90 Acm^{-2}. (c) Temperature dependent resistivity from 260 K to 5 K.

4.6.2 Estimation of the Local Temperature

Fig. 4.9 shows anti-Stokes and Stokes spectra for different induced currents densities. The analysis of the temperature by equation (2) strongly depends on the treatment of the background arising from Rayleigh scattering that clearly differs for the sign of energy change. In panel (a) and (b) we report results for two ways of describing the background that yield rather different temperatures for modes at low energies. In particular for the mode A1 is is not possible to determine the background with sufficient precision. Only the peak A8, which exhibits a high intensity on a lower background, seems suitable to indicate the temperature of the sensed regions of the crystal.

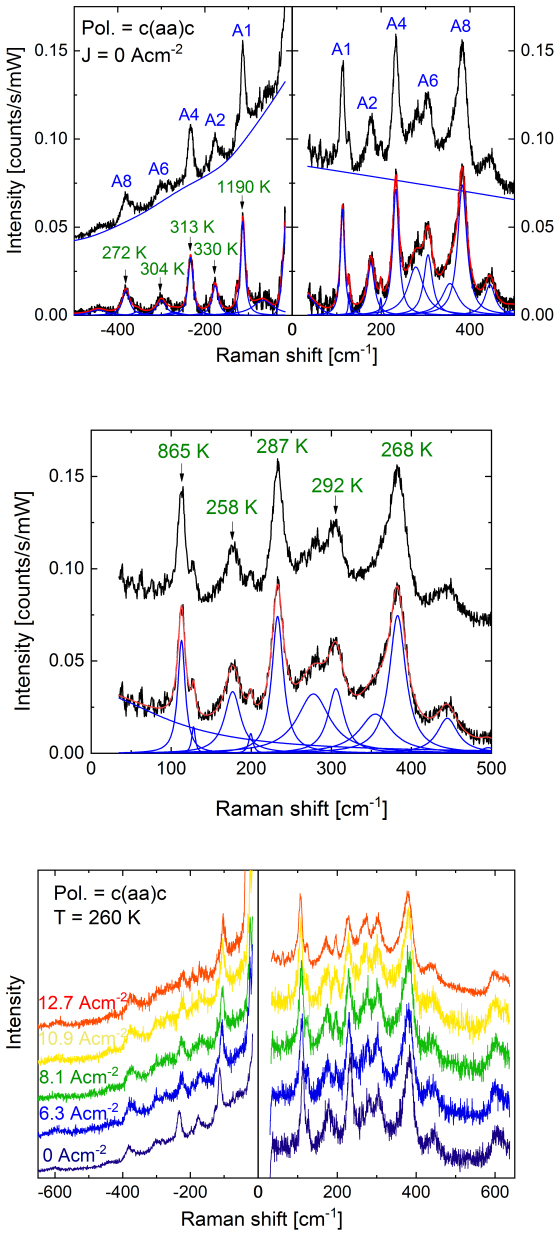

Figure 4.9: Anti- Stokes- and Stokes- Raman spectra in c(aa)c- geometry. (a) and (b), fitted spectra for 0 Jcm^{-2} with two different background subtractions and the corresponding calculated temperatures (green). (c) Spectra for 0 to 12.7 Acm^{-2}. For a better comparison the spectra a shifted.

Chapter 5

Current Influenced Magnetism in Ca_2RuTiO_4

As shown in the previous chapter Raman light scattering experiments on Ca_2RuO_4 give new insights to the interplay between lattice degree of freedom and coupling mechanisms. We investigate the sample magnetization by an applied current. Here, we report a sudden magnon energy renormalization for $J < 0.02$ Acm^{-2}, interpreted as orbital re-orientation, which is percolating through the sample and is responsible for the increase of the conductivity. We show that increasing the current to $J \approx 1$ Acm^{-2} suppresses the AFM order and forces additionally a crystal lattice change.

5.1 Introduction

The focus of this chapter is the interplay between magnetic, orbital, and lattice degrees of freedom in $Ca_2Ru_{0.99}Ti_{0.01}O_4$ in the view of controlling external stimuli induced phase transitions [185]. We recap from the previous chapter that the flattening of the RuO_6 octahedra along the c- axis and the stretching along the b- axis, causes beside of a temperature-driven metal-insulator transition (MIT) at $T_{MIT} \approx 357$ K [136, 152], also an orbital ordering at $T_{OO} \approx 260$ K [138, 173, 186], and a anti-ferromagnetic odering (AFM) at $T_N \approx 110$ K [135]. Additionally, also the tilt of the RuO_6 octahedra increases upon cooling [135, 136], pinning the magnetic moment parallel to the b axis [187]. In the present case of $Ca_2Ru_{0.99}Ti_{0.01}O_4$, a magnetic moment canting of $\sim 0.08\mu_B$ (canting angle $\alpha = 3.5°$) along the a- direction was observed, interpreted as RuO_6 octahedra distortion induced Dzyaloshinskii-Moriya interaction (DMI) [135]. It is very likely that this RuO_6 octahedra distortions also change the orbital occupation, provoking the $4d_{xy}$ orbitals to become doubly and the $4d_{xz,yz}$ singly occupied, and thus

influencing the electronic and magnetic behavior of the compound [139, 188]. SOC was claimed to be strong enough to change the multiplet structure to a nonmagetic j = 0 ground state, forming singlet magnetism [146, 148]. Inelastic neutron scattering (INS) experiments observed a large magnetic anisotropy gap in the in-plane transverse modes which was explained by broken tetragonal symmetry and SOC, described by a conventional Heisenberg model [187, 189]. Especially, experiments under current induced conditions have a significant problem to disentangle Joules heating from intrinsic effects, which becomes even worse in inhomogeneous samples, varying strongly the local temperature and consequently the lattice constants. Nano-imaging optical techniques report nano-stripe structured areas of phase coexistence with different optical reflectivity [160]. Zhao et *al*. reports a lattice orthorhombicity reduction for $J > 0.15$ Acm^{-2} due to the Oxygen-octahedra distortions, leading to a new orbital order and the suppression of the AFM phase [188], explaining this by a current stabilized non-equilibrium electron occupancy of the t_{2g} orbitals which are forcing the lattice changes. A total current induced suppression of the AFM ordering is also reported by Raman spectroscopy measurements [163].

Here, we present Raman scattering experiments on $Ca_2Ru_{0.99}Ti_{0.01}O_4$ in the AFM-ordered phase for current densities $J \leq 1.5$ Acm^{-2}. We observe a crystallographic direction dependent magnon anisotropy, due to slightly different a- and b- axis. Moreover, this non-degenerated magnon modes reveal an sudden energy renormalization for $J < 0.02$ Acm^{-2}, interpreted as percolating orbital re-orientation, which is forced by the current induced electron imbalance, and leading finally to the suppression of the AFM order. After the nearly total suppression of the AFM order also the crystallographic bond length changes at $J \approx 1$ Acm^{-2} as a consequence of the further increase of the electro-static force.

5.2 Experimental

The experimental setup is as described in Chapter 4. The current direction for all presented results is along the crystallographic a-axis, measured by a two-point probe method when Raman scattering experiments were done simultaneously. For this case the current was set always at 260 K and subsequently cooled down to 15 K cryostat temperature. Therefore, several cooling and heating cycles were performed on one sample. Independently, the bulk resistivity of $Ca_2Ru_{0.99}Ti_{0.01}O_4$ was measured by a four-point method, depending on the applied current and the temperature.

5.3 Results

5.3.1 Raman Spectroscopy

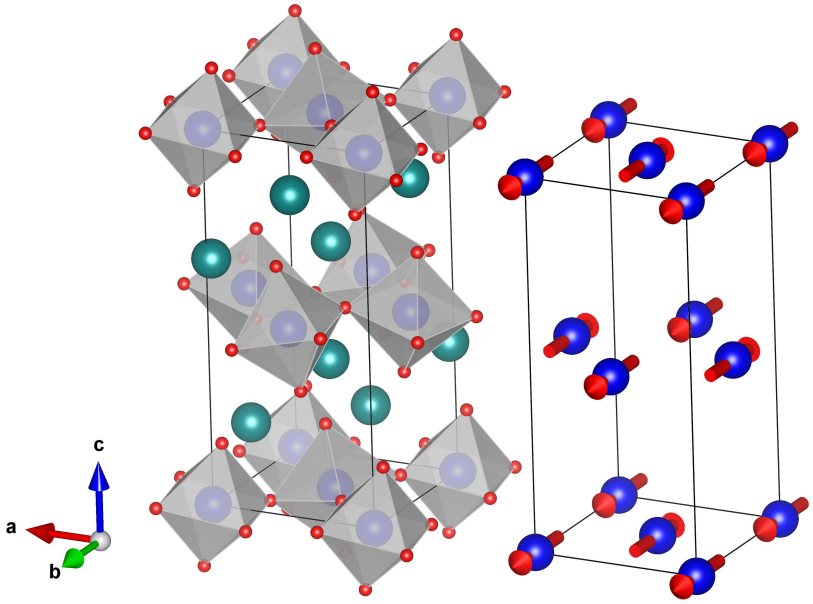

Figure 5.1: Sketch of the $Ca_2Ru_{0.99}Ti_{0.01}O_4$ crystal and the corresponding B-centered G-type AFM structure.

The crystallographic space group of Ca_2RuO_4 is the orthorhombic Pbca-D_{2h}^{15} (61). The corresponding Wykoff positions are 4a for Ru^{4+}, and 8c for Ca^{2+}, O_1^{2-} and O_2^{2-} [135]. Whereas only the position 8c is Raman active. Therefore, the Raman active irreducible representation of the 81 $\Gamma-$point phonons is

$$\Gamma = 9A_g + 9B_{1g} + 9B_{2g} + 9B_{3g}, \tag{5.1}$$

which corresponds to the following Raman tensors of D_{2h}(mmm):

$$\underbrace{\begin{pmatrix} a & 0 & 0 \\ 0 & b & 0 \\ 0 & 0 & c \end{pmatrix}}_{A_g}, \underbrace{\begin{pmatrix} 0 & d & 0 \\ d & 0 & 0 \\ 0 & 0 & 0 \end{pmatrix}}_{B_{1g}}, \underbrace{\begin{pmatrix} 0 & 0 & e \\ 0 & 0 & 0 \\ e & 0 & 0 \end{pmatrix}}_{B_{2g}}, \underbrace{\begin{pmatrix} 0 & 0 & 0 \\ 0 & 0 & f \\ 0 & f & 0 \end{pmatrix}}_{B_{3g}}. \tag{5.2}$$

According to the single layer stacking, two different magnetic structures are known for Ca_2RuO_4 [136] which correspond to Pbca (A- centered) and Pbc'a' (B- centered) [136, 189]. The net ferromagnetic canted moments per layer of Pbca cancel due to an

antiferromagnetic stacking, whereas the B-centered Pbc'a' structure results in a total ferromagnetic moment. By applying a time reversal operator θ on Pbca, one get the magnetic space group Pbc'a' (mm'm') for the B- centered variant [189], see Fig. 5.1. Further details can be found elsewhere [190–192]. Thus, the corresponding magnetic Raman tensors are given by

$$\underbrace{\begin{pmatrix} A & 0 & 0 \\ 0 & E & iB \\ 0 & iD & I \end{pmatrix}}_{R_1}, \underbrace{\begin{pmatrix} 0 & iG & H \\ iC & 0 & 0 \\ F & 0 & 0 \end{pmatrix}}_{R_2}. \tag{5.3}$$

The excitations could be probed by crossed and parallel polarized light, corresponding to $c(ab)\bar{c}$ or $c(ba)\bar{c}$, and $c(aa)\bar{c}$ or $c(bb)\bar{c}$ in Porto notation, respectively, by

$$I \sim |e_{out} R_i e_{in}|^2, \tag{5.4}$$

where I is the intensity of the Raman active excitation, R_i $(i = 1, 2)$ is the Raman tensor, e_{out} and e_{in} are outgoing and incoming polarizations of the light, respectively.

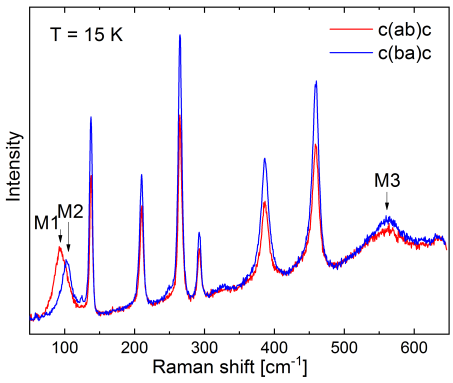

Figure 5.2: Raman spectra of $Ca_2Ru_{0.99}Ti_{0.01}O_4$ at 15 K in c(ab)c- and c(ba)c - geometries. Magnetic excitations are depicted as M1, M2, and M3.

Fig. 5.2 presents the Raman spectra of $Ca_2Ru_{0.99}Ti_{0.01}O_4$ at 15 K in $c(ab)\bar{c}$- and $c(ba)\bar{c}$- geometry. The excitations M1 ($\sim$ 95 cm^{-1}), M2 ($\sim$ 105 cm^{-1}), and M3 ($\sim$ 565 cm^{-1}), appearing below $T_N = 110$ K, are magnetic in origin, since phonon modes can be excluded by the discussion of the phonon modes in Chapter 4. Accordingly, M1 and M2 are assigned as one-magnon, and M3 is a two-magnon excitation, respectively, supported by calculations in Ref. [189]. Interestingly, M1 and M2 are exclusively visible either in $c(ab)\bar{c}$ or $c(ba)\bar{c}$ polarization. This is a consequence of the crystallographic,

and subsequently, the magnetic anisotropy [189], which is reflected by group theoretical considerations, summarized in Equ. 5.3, and leading with Equ. 5.4 to the polarization dependent intensities $I \sim |iG|^2$ and $I \sim |iC|^2$ for $c(ba)\bar{c}$ and $c(ab)\bar{c}$, respectively.

In particular, assuming k along the c- axis with perpendicular e_{out}- and e_{in}- vectors in Equ. 5.4, one obtain for both $c(aa)\bar{c}$ and $c(bb)\bar{c}$ $I = 0$, but for $c(ba)\bar{c}$ and $c(ab)\bar{c}$ they are $I \sim |iG|^2$ and $I \sim |iC|^2$, respectively, resembling the experimental findings.

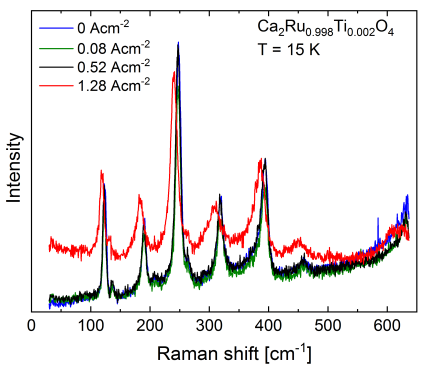

(a) c(aa)c

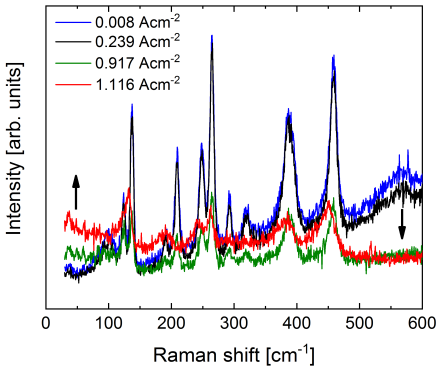

(b) c(ba)c

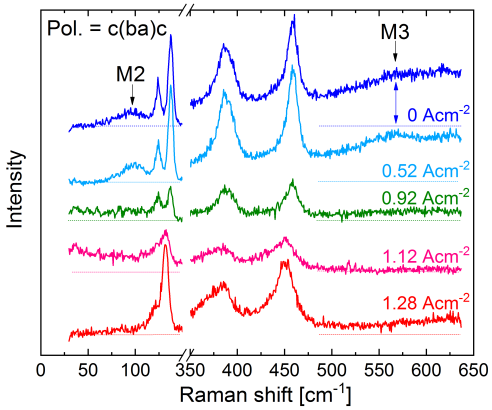

(c) c(ba)c

Figure 5.3: Current dependent Raman spectra at ≈ 80 K in a) c(aa)c and b,c) c(ba)c - geometries. M1-M3 denotes the magnetic excitations and dashed lines indicate the estimated base lines.

In the following, the magnetic excitations are investigated under the influence of different applied currents, which were set always at 260 K before the sample was cooled down to ≈ 15 K cryostat temperature and an effective lattice temperature of ≈ 80 K . The lattice temperatures are deduced by the Stokes/ anti-Stokes ratios as discussed

in Chapter 4. Fig. 5.3 show the current induced changes of the Raman spectra in the c(aa)c and c(ba)c- polarizations. Besides the pure phonon excitations in c(aa)c, c(ba)c additionally exhibit the magnon excitations, denoted as M2 and M3. The difference between Fig. 5.3b and 5.3c is only the way of presentation. Several observations are directly evident from these three figures. First, small current densities < 0.92 Acm^{-2} does not affect the local lattice structure directly, because the phonon intensities and energies does not change.

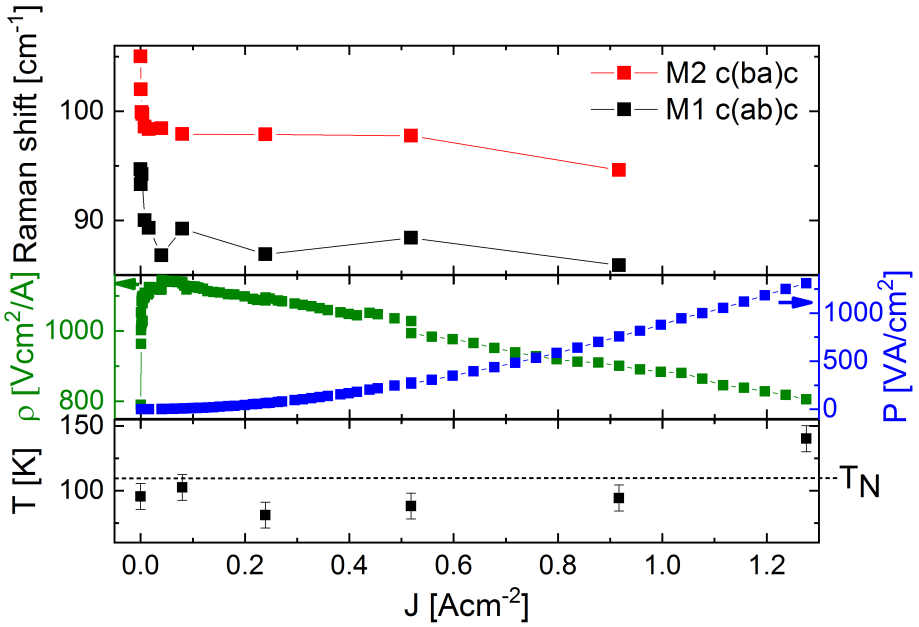

Figure 5.4: Summarized current dependent magnon energies for c(ab)c- and c(ba)c -geometries from 5.3, together with the simultaneously measured and calculated resistivity, Joules power, and the lattice temperature.

At ≈ 0.92 Acm^{-2} the phonon mode intensities significantly decrease and the line shapes are broadened. Additionally, the magnetic excitations are strongly suppressed and disappear. At ≈ 1.12 Acm^{-2} an energy shift and an increase of the Raleigh tail is observed. Usually, Raman scattering on metallic samples exhibit strong Raleigh scattering accompanied by a background increase due to electron screening effects, which is responsible for the phonon intensity reduction, compared to an entirely insulating sample. A further broadening of the phonon modes together with an energy shift and the total suppression of the magnetic excitations is visible at 1.29 Acm^{-2}. Compared to the spectrum taken at $J = 0.92$ Acm^{-2} the phonon intensities are almost equal. The phonon mode intensities increase by increasing the current density and at $J = 1.28$ Acm^{-2} they reach a comparable level to $J = 0$ Acm^{-2}. M3, at ~ 580 cm^{-1}, which is

assumed as two-magnon excitation is completely suppressed.

Comparing the current dependent energy shifts of the magnetic excitations M1 and M2 with the simultaneously measured resistivity, the calculated lattice temperatures and the power, several interlocking stages are observed, Fig. 5.4. Increasing the current to $J \approx 0.02$ Acm^{-2}, increases rapidly the resistivity, but decreases at the same time the one-magnon excitation energy by ≈ 5 cm^{-1} (0.7 meV), whereas the calculated lattice temperature and the calculated Joules power are constant within the experimental errors. Moreover, the temperature of ≈ 90 K is further constant until $J \approx 0.92$ Acm^{-2}, before it rises above T_N. Between $J \approx 0.02 - 0.1$ Acm^{-2} the resistivity stays at a plateau, before it drops constantly by increasing the current. The magnon energies M1 and M2 are not affected by the increase of the conductance and they shift again above $J \approx 0.52$ Acm^{-2}. Note, the Joules power is continuously rising. The partial resistivity offsets occur when not the same equilibrium position as before is found after an cooling cycle. This error source is hardly avoidable and underlines the sensitive character of the sample, the middle panel in Fig. 5.4. For current densities up to at least $\sim J = 1.3$ Acm^{-2} the Raman spectroscopy features are reversible, Fig. 5.5. This is not the case for $J \sim 12.4$ Acm^{-2}, where the phonon modes show the same behavior, but the magnetic excitations are strongly suppressed even when it is remeasured at $J = 0$ Acm^{-2}.

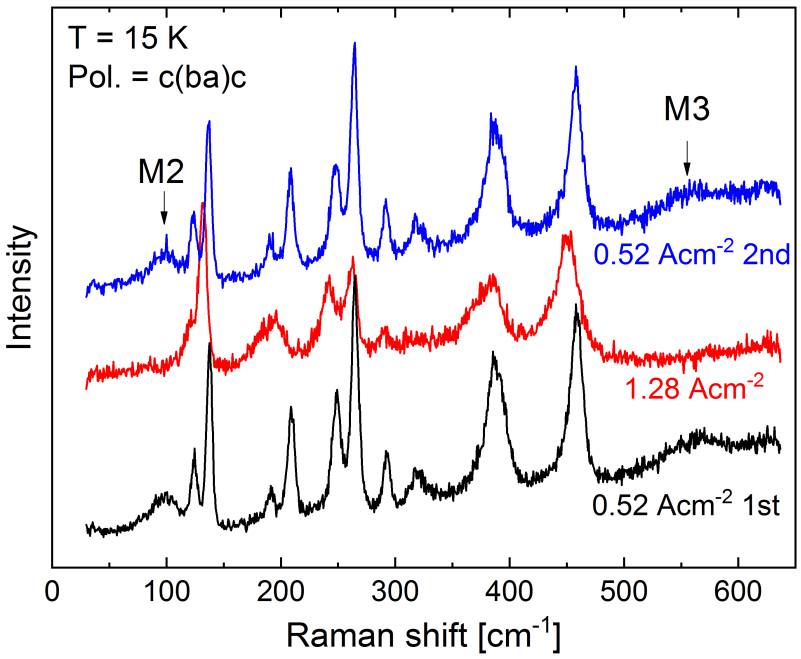

Figure 5.5: Raman spectra showing the reversibility of the excitation (blue) after suppressing the magnetic excitation and shifting the phonons (red) and going back to the original configuration (blue).

5.4 DFT Calculations

In order to investigate the electronic structure we used density functional theory (DFT) within the generalized gradient approximation (GGA) taking into account strong Coulomb correlations via the GGA+U method (see also Ref. [193]). The on-site Hubbard repulsion U and the Hund's exchange coupling is assumed to be 3 eV and $J_H = 0.7$ eV, respectively. Electronic structure GGA+U calculations were done by the Vienna ab initio simulation package (VASP) [194], where an exchange-correlation potential [195] and the plane-wave energy cutoff of 500 eV was assumed. The k-space was integrated by the tetrahedron method using the k-mesh density of $8 \times 8 \times 4$. The exchange parameters were calculated for the Heisenberg model written in the following form:

$$H = \sum_{i>j} J_{ij} S_i S_j, \tag{5.5}$$

where i and j counts the lattice sites and the total energy method is included in the $JaSS$ code.

5.4.1 Results

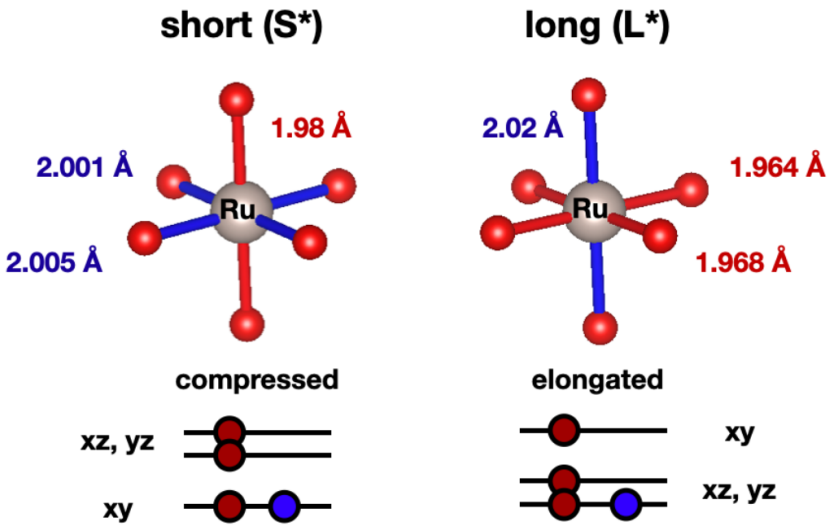

Figure 5.6: Principal oxygen octahedra distortions in S* and L* phases with the corresponding energy level schemes.

S* and L* denote the current influenced S- and L- phases and the corresponding lattice constants used in the present calculations can be found in Ref. [135, 136, 161]. While in the S-phase the Ru atom has a shorter distance to the axial oxygen than to the in-plane (equatorial) ones, the octahedron is compressed. In the case of the L-phase the situation is the opposite which leads to an elongated octahedron, Fig. 5.6. This affects the crystal-field splitting and changes orbital sequence in a diagram of the energy levels. For all "short" phases the lower xy orbital is fully occupied, while in the "long"-phases this orbital turns out to be half-filled. In contrast in L-phases the lower levels are of xz/yz symmetry. They are doubly degenerate. As we will show below this strongly affects magnetic properties of "short" and "long" phases.

Isotropic exchange paths considered for S, S*, L and L* phases are shown in Fig. 5.7 and corresponding values of exchange constants are presented in Table 5.1. The exchange parameters are anti-ferromagnetic in nature and the exchange interaction between the nearest in-plane Ru ions strongly decreases by going from the S- (S*-) to the L- (L*-) phase.

Strong in-plane antiferromagnetic exchange in the S- phases is obviously due to superexchange interaction between the half-filled xz and yz. Slightly different values of exchange constants are most probably related to features of the crystal structure of S and S* phases. In L-phases the situation is very different - the xy orbital is half-filled

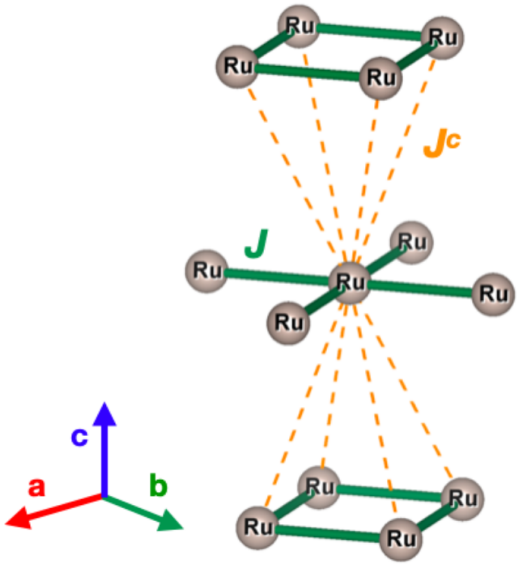

Figure 5.7: In-plane (J) and out-of-plane (J_c) exchanges paths considered in the article.

J_{ij}	S	S*	L	L*
J	5.0	5.3	2.8	1.7
J^C	0.6	0.6	0.3	0.2

Table 5.1: Calculated in the GGA+U approximation parameters of the isotropic exchange interactions (in meV) for various phases of $Ca_2Ru_{0.99}Ti_{0.01}O_4$.

and it provides antiferromagnetic exchange, but there is also additional contribution from the xz/yz orbitals. The most direct way to analyze this effect would be to plot the half-filled orbital of the xz/yz doublet in the GGA+U calculation.

However, due to technical reasons it is easier to draw a single completely filled t_{2g} orbital instead. This is exactly what is shown in Fig. 5.8. One can see that there is antiferro-orbital ordering for these orbital and hence for the half-filled xz/yz orbital as well. The orbitals at the neighboring sites are nearly orthogonal to each other. Exchange interaction between these orbitals are of super-exchange type and occurs via two orthogonal p-orbitals. This 90° path gives the ferromagnetic contribution to the total exchange interaction. It is not strong enough to fully suppress the existing antiferromagnetic contribution due to the xy orbitals, but substantially reduces it. Therefore, the orbital ordering is assumed to cause the changes in the magnetic properties in L*-phase of $Ca_2Ru_{0.99}Ti_{0.01}O_4$.

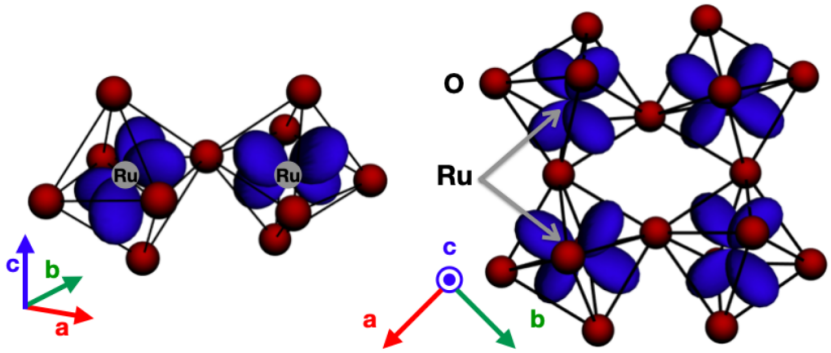

Figure 5.8: Result of the GGA+U calculation for the lowest in energy magnetic configuration (all nearest neighbors in the ab- plane are anti-ferromagnetically ordered). The Ru 4d orbitals are doubly occupied for each site (in the L*-phase). The other half- filled orbital with the same energy is orthogonal to the drown one, showing the antiferro-orbital ordering, discussed above.

5.5 Discussion

Raman scattering on $Ca_2Ru_{0.99}Ti_{0.01}O_4$ was reported previously in the literature [164, 182], but with different interpretations for the magnetic modes M1/M2 and M3. Sow et *al*. (2017) claim M1/M2 as two-magnon excitation, whereas Souliou et *al*. (2017) interpreted it as a one-magnon. Neutron scattering, expanded by magnon dispersion calculations [189], supports the one-magnon interpretation. The one-magnon and

phonon energies up to 460 cm^{-1} correspond well to Ref. [163, 182], discussed in detail in Chapter 4. Differences occur in B_{1g}- geometry at the excitation M3 at ~ 568 cm^{-1} which we assign to a broad two-magnon excitation from a magnon lying at ≈ 45 meV (360 cm^{-1}). This peak were reported previously at ~ 540 cm^{-1} as a part of a broad continuum, denoted as B' and interpreted as two- Higgs continuum [182]. The authors also report a continuum A' in A_g- geometry which is claimed to be the corresponding amplitude mode peaking at ~ 320 cm^{-1} (40 meV). Phonon mode calculation reveals a huge number of very close lying phonon modes which significantly could contribute to these continua by mode leaking caused by anisotropic lattice distortions.

Raman scattering experiments show that small applied currents does not destroy the magnetic exciations suddenly, but forces a magnon energy renormalization. The simultaneous increase of the resistivity suggests an increase of the electrostatic pressure which can be relaxed by the re-orientation of the orbitals. Our DFT calculations show that they are significant differences between the coupling constants in the S- and L-phase, forcing the orbital ordering. Increasing the current increases the number of re-oriented orbitals, which are percolating through the sample, leading to the linear resistivity drop starting at $J \approx 0.1$ Acm^{-2}, and finally suppresses the AFM ordering at $J \approx 1$ Acm^{-2}. Current results state that additional to the S- and L- phase also an current induced intermediate phase MI exists, which is closely related to the S-phase, coexisting next to the each other [165]. The authors also claim that the L^* and S^* from Ref. [161] measured at 110 K, rather belong to temperature driven lattice constants of the L- and S- phase measured at 240 K. From the symmetry point of view this does not matter much, because even the local crystal structure is always assumed to be the orthorhombic Pbca-D_{2h}^{15}, differing only by the c- lattice constants. Thus, the local concentration of these phases determine the electronic and magnetic properties of the sample. Nevertheless, Raman spectroscopy measurements show by the clear phonon shifts that the crystal enters a current induced phase. At this point, we need to remember that a pure metallic sample would not be measurable by Raman. Thus, we assume that we mainly measure the more insulating contribution of the sample, which is reacting to increasing strain and relaxes by changing the bond lengths. Okazaki et *al*. observed current dependent decreasing of the resistivity which is explained as gap energy suppression [159]. These effects were already mentioned for charge-ordered insulators or nonequilibrium superconducting states, where the superconducting gap is reduced by quasiparticles, formed by the induced current [196]. The tetragonal crystal-field splitting, occuring from the flattened RuO_6 octahedra, together with the strong Coulomb repulsion between the 4d electrons, stabilizes the d_{xy} orbital ordering

below T_{MIT} [159, 197]. These interpretation is supported by theoretical studies which suggesting that the orbital order follows the structural transition [138].

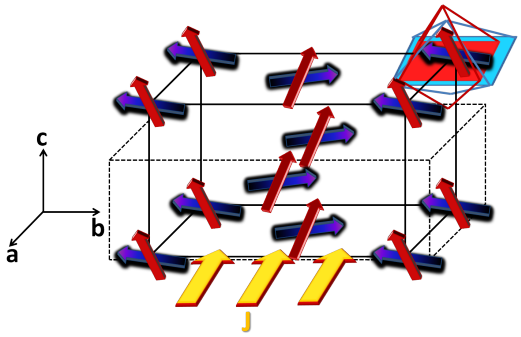

Figure 5.9: Sketch of the structural changes induced by a current density J in $Ca_2Ru_{0.99}Ti_{0.01}O_4$. The blue (red) arrows depict the magnetic moments from the Ru-atoms without (with) applied current. The blue (red) octahedra sketches the orbital distortions without (with) current, together with the crystallographic changes of the the unit cell, depicted as dashed (solid) black lines.

5.6 Acknowledgments

The here presented chapter is in preparation for submission. The Raman measurements, their analysis and interpretation were done by myself. The DFT calculations were done by Evgeniia Komleva and Sergey Streltsov. The manuscript was written by myself in collaboration with the co-authors. I gratefully acknowledge the fruitful discussions and help in sample preparation from Oliver Breuning and Johannes Engelmayer.

5.7 Appendix

5.7.1 Temperature-Dependent Measurements

Ca_2RuO_4 was measured in different geometries and polarization. Fig. 5.10 shows an overview of the Raman spectra taken 10 K from the crystallographic c- and b- axis. In the configuration, especially the mode at ≈ 600 is very pronounced. Fig. 5.11 shows the temperature and polarization dependent Raman spectroscopy measurements of the crystallographic b- axis.

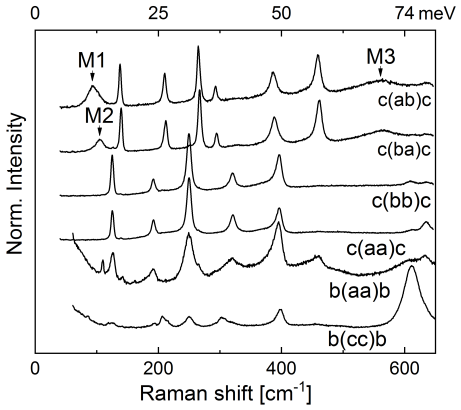

Figure 5.10: (a) Raman spectra at 10 K in A_{1g} ($c(aa)\bar{c}$, $c(bb)\bar{c}$, $b(aa)\bar{b}$, $b(cc)\bar{b}$) and B_{1g} ($c(ab)\bar{c}$, $c(ba)\bar{c}$) geometry. M1, M2, and M3 denote the magnetic excitations.

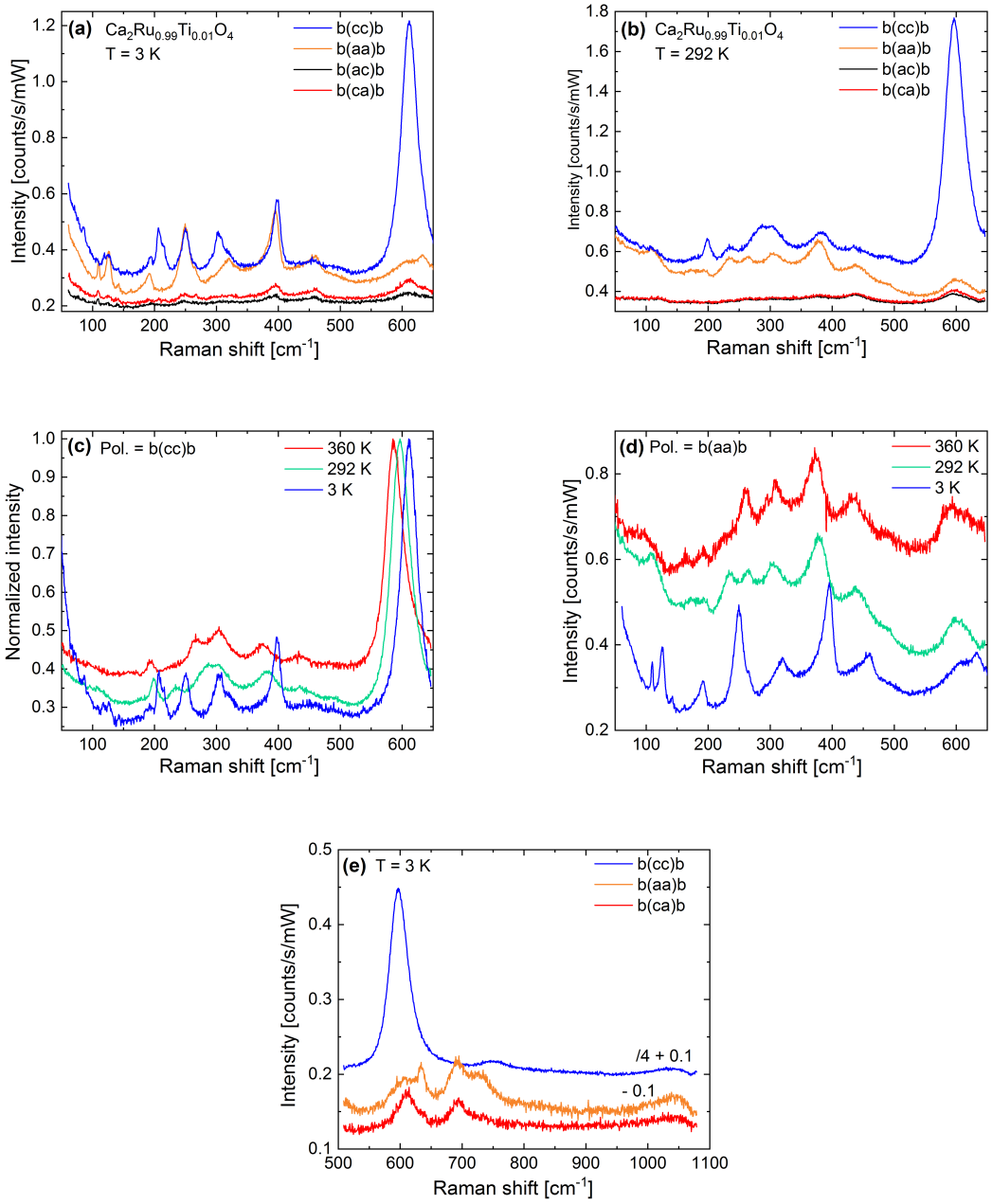

Figure 5.11: (a)-(e) Temperature and polarization dependent Raman spectra of the crystallographic b- axis of Ca_2RuO_4 .

Chapter 6

$BiSbTeSe_2$

The tetradymite compound $BiSbTeSe_2$ is one of the most bulk-insulating three-dimensional topological insulators, which makes it important in the topological insulator research. It is a member of the solid-solution system $Bi_{2-x}Sb_xTe_{3-y}Se_y$, for which the local crystal structure, such as the occupation probabilities of each atomic site, is not well understood. We have investigated the temperature and polarization dependent spontaneous Raman scattering in $BiSbTeSe_2$, revealing a much higher number of lattice vibrational modes than predicted by group theoretical considerations for the space group $R\bar{3}m$ corresponding to an ideally random solid-solution situation. The density functional calculations of phonon frequencies show a very good agreement with experimental data for parent material Bi_2Te_3, where no disorder effects were found. In comparison to Bi_2Te_3 the stacking disorder in $BiSbTeSe_2$ causes a discrepancy between theory and experiment. Combined analysis of experimental Raman spectra and DFT calculated phonon spectra for different types of atomic orders showed coexistence of different sequences of layers in the material and that those with Se in the center and a local order of Se-Bi-Se-Sb-Te, are the most favored.

6.1 Introduction

Three-dimensional (3D) topological insulators (TIs) attract a great deal of interest mainly due to their topologically-protected metallic surface states in which the spin is locked to the momentum [111, 198]. Such a spin-momentum locking provides opportunities for realizing various useful functionalities, such as the control of spin polarization for spintronics or the creation of Majorana zero modes for topological quantum computation. To take advantage of the peculiar surface state properties, it is useful to create a situation where the current flows only through the surface states; this requires that

the bulk of a 3D TI should be insulating. In this regard, some of the tetradymite compounds, such as Bi_2Se_3, Bi_2Te_3, and Sb_2Te_3, are prototypical 3D TIs [199] and they have been intensively studied in recent years, but these binary tetradymite compounds are not really insulating in the bulk. The first bulk-insulating 3D TI material, Bi_2Te_2Se, was discovered in 2010 and it is an ordered ternary tetradymite coumpound [200]. Its ordered nature, with the Se layer conceiled in the middle of the Te-Bi-Se-Bi-Te quintuple-layer (QL) unit, is the key to its bulk-insulating property. To further improve the bulk-insulating property, Ren *etal*. have employed the concept of compensation and synthesized a series of solid-solution tetradymite compounds, whose compositions are generally written as $Bi_{2-x}Sb_xTe_{3-y}Se_y$ (BSTS), that are bulk-insulating [201, 202]. In such BSTS compounds, the concealment of the Se layer in the middle of the QL unit is kept intact, but an appropriate mixing in the occupancy of the anion layers as well as the outer chalcogen layers makes it possible to achieve a high level of compensation between residual electron- and hole-doping. In particular, the nominal composition of $BiSbTeSe_2$ (BSTS2), which corresponds to (x,y) = (1,2) variant of the BSTS solid solution, was found to achive a particularly high level of bulk-insulation [201, 203, 204]. Although, the transport gap is relatively small (up to ∼60 meV [201]), it is inevitable in compensated semiconductors [205] due to the formation of charge puddles [206]. Since BSTS2 is currently the most bulk-insulating 3D TI material available as a bulk single crystal, it is widely used in various experiments aiming at studying the surface transport properties [207–211]. Despite the importance of BSTS2 in the research of 3D TIs, little is know about its local crystal structure. For example, the extent of randomness in the Bi/Sb sites and the outer Te/Se sites in the QL layers has not been studied. If there is some correlations between the occupancies of these nominally random sites, it may lead to a local inversion-symmetry breaking, which might affect/limit the topological properties of this compound. In this respect, the high-frequency phonon modes detected in Raman scattering are sensitive to local symmetry of the crystal lattice, and hence they are expected to provide useful information on the local crystal structure of BSTS2. In the present paper, we report combined experimental (Raman) and theoretical [density-functional-theory (DFT)] study of BSTS2 solid solution, which allowed us to obtain insights into the local structure of BSTS2. The temperature and polarization-dependent Raman spectra show the existence of an unexpectedly high number of Raman-active modes, which are forbidden in the group-theoretical considerations of the global symmetry of BSTS2 ($R\bar{3}m$ [212]), signaling a high degree of local symmetry-breaking disorder. To understand their origin, we performed DFT calculations with different combinations of atomic layers in the unit cell.

This analysis points to the conclusion that the occupancy of the upper and lower sides of a QL unit are likely to be correlated to prefer the local structure of Se-Bi-Se-Sb-Te or Te-Sb-Se-Bi-Se, which breaks inversion symmetry. Moreover, we suggest the peak at ~ 120 cm^{-1} in the Raman spectra, corresponding to the E phonon, to be potentially a marker to estimate the degree of the local inversion symmetry breaking.

6.1.1 Experimental Details

The single crystals of BSTS2 used in the present study were grown from high-purity elements by using a modified Bridgman method in a sealed quartz glass tube. [201] Before the measurement, the crystals surface was cleaved along the (001) plane for a clean shiny surface. For the spontaneous Raman measurements a continuous wave DPSS laser of 532 nm wavelength and a Krypton gas laser of 647.1 nm wavelength were used. The samples were mounted in an Oxford Instruments Microstat cryostat, cooled by liquid Helium. Raman spectra were collected using a triple grating spectrometer operating in subtractive mode equipped with a LN_2 cooled charge-coupled device camera.

6.1.2 Results

6.1.2.1 Raman spectroscopy

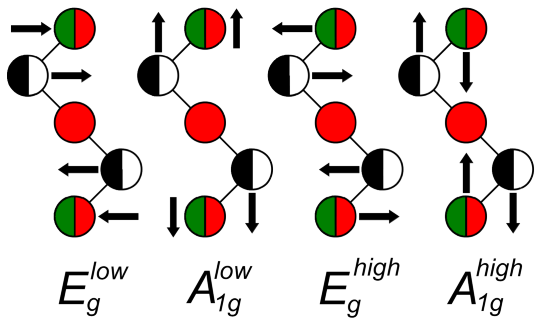

Figure 6.1: Displacement patterns of the ions, Te (green), Se (red), Bi and Sb (either black or white), in BSTS2 across the quintuple-layered unit cell, which generate Raman active modes. Low and high refers to the frequency.

Assuming the same primitive unit cell for $BiSbTeSe_2$ as for Bi_2Te_3, Bi_2Se_3, and Sb_2Te_3, five atoms are decisive for the group theoretical considerations of the vibrational modes. Therefore, in accordance with the chemical formula there are $3N-3 = 12$ optical lattice dynamical modes at q = 0. These modes are exclusively Raman- or

infrared-active according to inversion symmetry and consequently to their selection rules [213]. If BSTS2 is an ideally randomly distributed solid solution, the global symmetry of $R\bar{3}m$ should be the same as for the parent compounds with the Raman active irreducible representation given by

$$\Gamma_{vib} = 2A_{1g} + 2E_g, \tag{6.1}$$

where E_g and A_{1g} denote in-plane and out-of-plane vibrational modes, see Fig. 6.1. Locally, this statement does not necessarily hold anymore. Inversion symmetry automatically breaks when the QL are not symmetrically occupied by the same atoms. Thus, the originally assumed global space group of $R\bar{3}m$ for BSTS2 turns locally into $R3m$ with the following irreducible representation:

$$\Gamma_{vib} = 4A_1 + 4E. \tag{6.2}$$

Parallel and cross polarizations, i.e. c(aa)c and c(ab)c in Porto notation, probe the diagonal and off-diagonal elements of the Raman tensor, respectively.

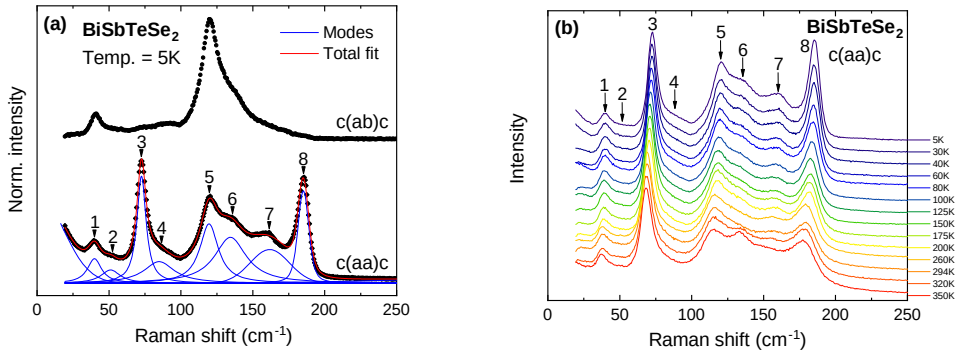

Figure 6.2: (a) Normalized Raman spectra of $BiSbTeSe_2$ at 5K in c(aa)c and c(ab)c geometry. The red curve shows a fit to the c(aa)c data using Lorenzian modes for no. 1 - 7 and a Voigt profile for no. 8 (blue curves). (b) Temperature dependent Raman spectra of $BiSbTeSe_2$, measured in c(aa)c geometry. Arrows denote the positions of the fitted oscillators, see Tab. 6.1.

Thus, E modes are observable in both c(aa)c and c(ab)c geometry, while A_1 are only visible in c(aa)c geometry. In the following, we use this more general representation to describe our results. Fig. 6.2a shows the polarization dependent Raman measurements of BSTS2 on the (001)- surface at 5 K. Two distinct modes ($\sim$ 40 cm^{-1} and $\sim$ 120 cm^{-1}) appear in both polarizations. These are in line with the number of reported E_g modes for perfectly ordered binary compounds, listed together with our fit results in

Tab. 6.1. It is clear by the number of modes observed in parallel polarization that they exceed the expected number for $R\bar{3}m$ symmetry. Notably, modes of Bi_2Se_3, Bi_2Te_2Se, and Sb_2Te_2Se correspond to energies of the observed peaks (1, 3 and 5 - 8), leading to the assumption that the configuration with the Selenium layer in the middle of the QL is indeed the most favoured one and the compound is highly mixed. In this sense, the obtained Raman spectrum is a superposition of locally differing sequences of ions.

To shed more light on this, we performed temperature dependent Raman measurements, presented in Fig. 6.2b. These spectra were measured from 350 K down to 5 K and each spectrum was normalized by the total spectral weight (SW), which decreases as expected by the Bose factor. The temperature dependent measurements were done with a laser excitation wavelength of 532 nm. Compared to the laser excitation wavelength of 647.1 nm, no differences, in terms of energy shifts or line widths of the modes, were observed. Numbered arrows depict the central positions of fitted oscillators. It was suggested that electron-phonon coupling could play a role in this class of compounds [214], revealed by possible asymmetric Fano line shapes. In $BiSbTeSe_2$, the most likely mode for showing this interaction is no. 8, which shows a strong deviation from a pure Lorentzian line shape, especially below 80 K. However, according to the high number of phonon modes, it is not possible to make consistent assumptions about the underlying continuum. Therefore, we cannot confirm a Fano-like resonance behaviour with our data. The best fitting results were achieved by applying a Pseudo-Voigt-function, which reflects usually the instrumental limitation in the case of a very sharp mode. Fig. 6.3 shows the temperature dependencies of the Raman shifts and full width at half maximum (FWHM) for the strongest modes no. 3, 5, and 8. They all show anharmonic phonon decaying behaviour. For the mode no. 8, this effect is more pronounced, which implies stronger anharmonic coupling to the lattice. Below ~ 40 K the observed variations with temperature saturate. This coincides with the reported temperature of charge puddle formation [215].

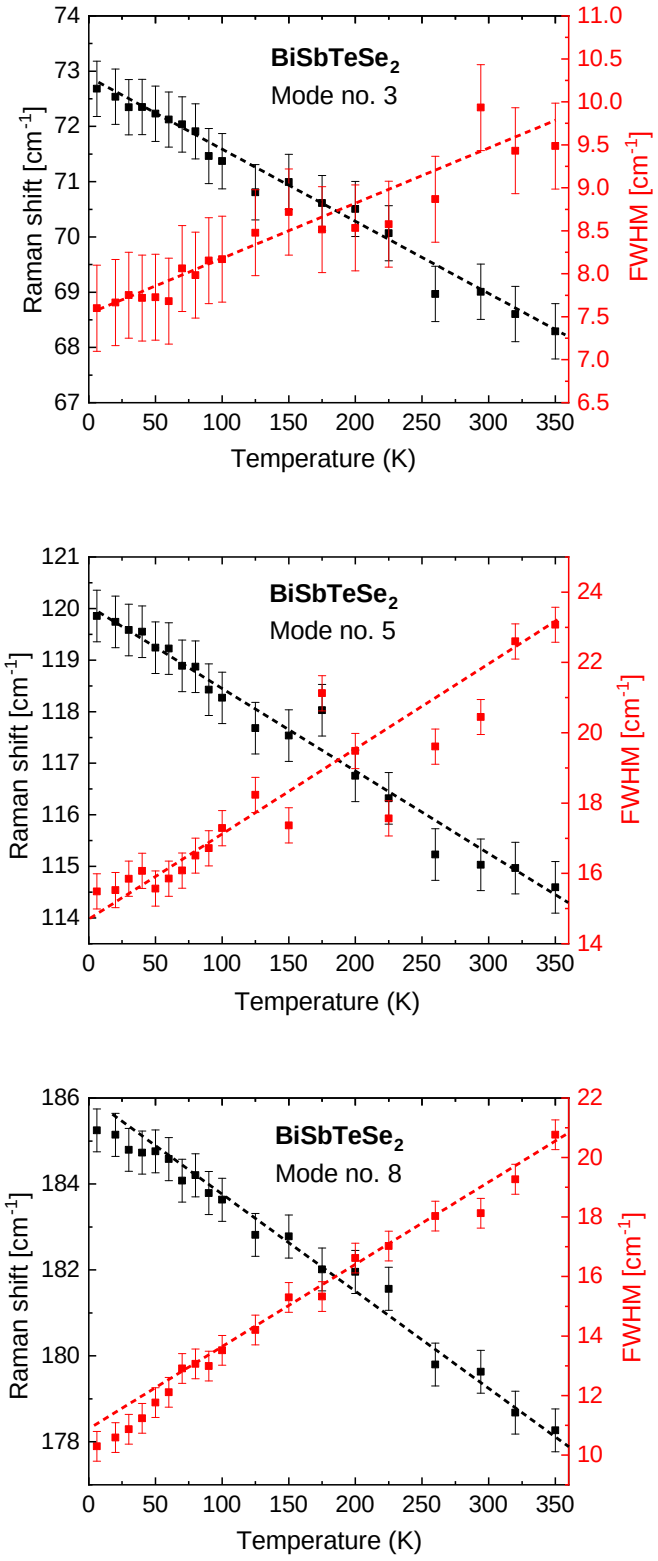

Figure 6.3: Temperature dependent Raman shifts and FWHM of mode (a) no. 3 (b) no. 5 (c) no. 8. Dotted lines are guides for the eyes.

	$BiSbTeSe_2$				Bi_2Te_3		Bi_2Se_3 [213]	Sb_2Te_3 [213]	Bi_2Te_2Se [214,216]	Sb_2Te_2Se [217]	Bi_2TeSe_2 [218,219]
No.	294 K	5 K	FWHM	Pol.	Exp.	Cal.	Exp.	Exp.	Exp.	Exp.	Exp.
1	38.5	40.1	11.1	$\perp, \parallel$	35.8 (E_g)	39.1 (E_g)				41.1 (E_g)	
2	49.0	50.4	13.0	$\parallel$							
3	69.0	72.7	7.6	$\parallel$	62.5 (A_{1g})	63.6 (A_{1g})	72 (A_{1g})	69 (A_{1g})	67.7 (A_{1g})		70 (A_{1g})
4	81.4	85.8	22.7	$\parallel$						82.2 (A_{1g})	
5	114.8	119.9	15.5	$\perp, \parallel$	103 (E_g)	103.2 (E_g)	121 (E_g)	112 (E_g)	110.7 (E_g)	117.5 (E_g)	129 (E_g)
6	126.8	134.2	23.7	$\parallel$	134 (A_{1g})	136.1 (A_{1g})			142	138.3 (E^L)	
7	160.2	160.9	41.1	$\parallel$				165 (A_{1g})	157.7 (A_{1g})		
8	180.1	185.2	10.3	$\parallel$			174.5 (A_{1g})			188.9 (A_{1g})	171 (A_{1g})

Table 6.1: Fitted Raman shifts in cm^{-1}, measured at 294 K and 5K, and the FWHM for the latter ones. $\perp$ and $\parallel$ denotes perpendicular and parallel polarization, respectively. Experimental and in this work calculated Raman shifts of Bi_2Te_3 are presented together with comparable compounds, given from the literature for Bi_2Se_3 [213], Sb_2Te_3 [213], Bi_2Te_2Se [214,216], Sb_2Te_2Se [217], and Bi_2TeSe_2 [218,219]. The assigned irreducible representations are indicated in parenthesis. E^L has been assigned to a local mode [217].

6.1.2.2 Density Functional Calculations of Phonon Modes

To investigate the possible origins of the observed vibrational modes, DFT calculations of lattice dynamics were performed. First we calculated the well investigated parent compound Bi_2Te_3 and found a rather good agreement of phonon frequencies with the experimental results (see Tab. 6.2). Maximal deviation between theoretical and experimental frequencies does not exceed 3.3 cm^{-1}. The binary compound lattice parameters and atomic positions were taken from literature [220]. The rhombohedral axes for $BiSbTeSe_2$ are $a = 10.09326$ $\AA$ and $\alpha = 23.7852°$ [201]. As the sequence of atomic layers in $BiSbTeSe_2$ is unknown and, as it was mentioned above, one would expect a stacking disorder, we arranged atoms in the unit cell in three different ways: Se(1)-Sb-Se(2)-Bi-Te, Se(1)-Bi-Se(2)-Sb-Te and Se(1)-Sb-Te-Bi-Se(2). Previously equivalent atomic positions are now occupied by different sorts of atoms, breaking the inversion symmetry. Resulting structure for $BiSbTeSe_2$ and the unit cell used in the calculations are shown in Fig.6.4.

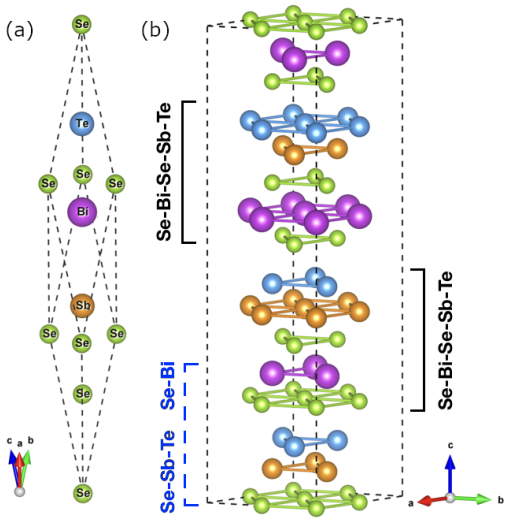

Figure 6.4: Crystal structure of $BiSbTeSe_2$ in $R3m$ with (a) rhombohedral and (b) hexagonal unit cells.

We used the frozen-phonon method [221] and density functional theory (DFT) to calculate phonon frequencies. The exchange-correlation functional was chosen to be in the form proposed by Perdew et *al.* [179, 222]. Since the spin-orbit coupling (SOC) was shown to be important in the formation of topologically protected states in the parent compounds Bi_2Te_3 and Bi_2Se_3 [199, 223], we included this interaction in the calculation scheme. The calculations were performed using the Vienna ab initio simulation package (VASP) [178, 194, 224, 225]. A plane-wave cutoff energy was set to 500 eV. We found

that the k-mesh considerably affects the results of the calculations. Present results were obtained with the $8 \times 8 \times 8$ k-mesh. The structure was geometrically optimized until the energy difference between two ionic iterations reached 10^{-5} eV/atom. To calculate the Hessian matrix only symmetry inequivalent displacements were considered within finite differences method.

In the present calculations for $BiSbTeSe_2$, the three atomic arrangements mentioned above were considered. According to the electronic structure calculations the most favorable sequence is Se(1)-Bi-Se(2)-Sb-Te. Its total energy is lower by 68 meV/f.u. than for Se(1)-Sb-Se(2)-Bi-Te, and lower by approximately 100 meV/f.u. than for Se(1)-Bi-Te-Sb-Se(2). Keeping the same relative order of layers but choosing QL unit in another way (e.g. see Fig.6.4, blue dashed bracket) we got very similar results. However, the sequence with Selenium in the middle of the "real" QL unit still has the lowest total energy. Thus, from the theoretical point of view the most favoured stacking sequence is Se(1)-Bi-Se(2)-Sb-Te.

The calculation results for Bi_2Te_3 are listed in Tab. 6.2 and for different sequences of atomic layers in $BiSbTeSe_2$ in Tab. 6.2. The mode assignment was done using the analysis of the eigenvectors of the obtained dynamical matrix. The atomic displacements for a given frequency are in good agreement with the group theory consideration. As has been mentioned above, the calculated frequencies for Bi_2Te_3 show a good agreement with the experiment and lead to the conclusion that DFT should work for $BiSbTeSe_2$, too. There is indeed a good overall correspondence between calculation and experiment. However, to fit the data satisfactorily a very weak and broad mode centered at 49 cm^{-1} (No. 2 at 294 K) is needed which is absent in the DFT results. In addition, the E-mode at 128 cm^{-1} predicted from the DFT calculations is not resolved in the spectra, possibly due to a weak scattering strength in combination with the vicinity of the stronger E and A_1 modes observed at 119.6 cm^{-1} and 133.8 cm^{-1}, respectively. In Tab. II, one can see that the low frequency E line is found in all three possible structural stackings. In contrast, the observed E mode at 120 cm^{-1} fits only with the calculated E mode of Se(1)-Bi-Se(2)-Sb-Te sequence. Thus, this analysis suggests that locally our samples mostly have Se(1)-Bi-Se(2)-Sb-Te order, which is also supported by the DFT total energy calculations presented below.

Mode assignment	Se-Bi-Se-Sb-Te[a]	Se-Sb-Te-Se-Bi[a]	Se-Sb-Se-Bi-Te[b]	Se-Bi-Te-Se-Sb[b]	Te-Sb-Se-Se-Bi[c]
E	42.2	42.1	42.9	42.6	45.6
A_1	70.3	70.5	69.2	69.0	74.2
E	82.1	82.1	74.3	74.1	68.9
E	119.6	119.7	109.8	109.7	109.4
E	128.0	127.8	129.7	129.5	131.9
A_1	133.8	133.7	138.0	137.7	117.3
A_1	158.1	157.9	150.8	150.6	159.0
A_1	180.0	180.0	176.1	175.9	178.8
Total energy	0	16.6	68.1	117.6	240.0

Table 6.2: Calculated phonon frequencies in cm^{-1} and relative values of total energy in meV for different sequences of atomic layers in $BiSbTeSe_2$. The header row shows the QL unit cells used in the DFT calculations, where the superscripts (a, b, c) refer to formally different atomic arrangements.

6.2 Discussion

The DFT calculations of Bi_2Te_3 reproduce well the experimentally found phonon energies and symmetries at 5 K, confirming the group theoretical assumption for the space group $R\bar{3}m$. This consideration can, however, hardly be directly converted to $BiSbTeSe_2$ since in that case the inversion symmetry is necessarily broken. Indeed, the experiment reveals more than 4 modes ($R\bar{3}m : 2A_{1g} + 2E_g$), which is in good agreement with the theoretical predictions from a symmetry analysis ($R3m : 4A_1 + 4E$) and the DFT calculations. It is useful to note that in Bi_2Te_2Se or $Bi_2(Te_{1-x}Se_x)_3$ for 0.2 < x < 0.9, some peculiar modes which have neither A_1 nor E symmetry have been observed by Tian et al. [216] and Richer et al. [213]. These authors called them local modes, which were proposed to result from Se/Te antisite point defects and vibrate at their own frequency with a broad line width. In view of this work, these local modes may actually be related to the local inversion-symmetry breaking due to antisite defects. By comparing the phonon energies of the strong modes in the Raman spectra in Fig. 6.2 to the calculated phonon energies for various local structures, one notices that the sequences where Selenium is in the middle of the quintuple gives the strongest contributions to the phonon spectrum, meaning that in a major portion of the samples, Selenium is sitting in the middle of the quintuple layer. This is in line with our DFT calculations, which show that the sequence Se(1)-Bi-Se(2)-Sb-Te has the lowest total energy.

6.3 Summary

We have performed polarization dependent spontaneous Raman scattering in a temperature range from 6 K to room temperature and observed an unexpectedly high number of Raman active modes, which contradicts the group theoretical considerations for the global $R\bar{3}m$ symmetry and points to the significance of local inversion symmetry breaking. Our DFT calculations, which explain the Raman spectra of Bi_2Te_3 very well, help us to identify the most prominent local structure realized in $BiSbTeSe_2$, which turned out to be the Se(1)-Bi-Se(2)-Sb-Te sequence.

6.4 Acknowledgments

The here presented chapter has been published in

R. German, E. Komleva, P. Stein, V. Mazurenko, Z. Wang, S. Streltsov, Y.

Ando, P. van Loosdrecht,
"Phonon mode calculations and Raman spectroscopy of the bulk-insulating topological insulator $BiSbTeSe_2$,"
Phys. Rev. Materials, **5**, 054204, 2019.

The Raman measurements were performed by P. Stein and me. The data was analysed and interpreted by myself. The DFT calculations were done by Evgeniia Komleva and Sergey Streltsov. The manuscript was written by myself in collaboration with the co-authors.

6.5 Appendix

Fig. 6.5 shows the shiny surface of BSTS2. The corresponding X-diffraction patterns are in a good agreement with the simulated Bragg-peaks and supports the assumption of the group theoretical considerations of a global space group $R\bar{3}m$.

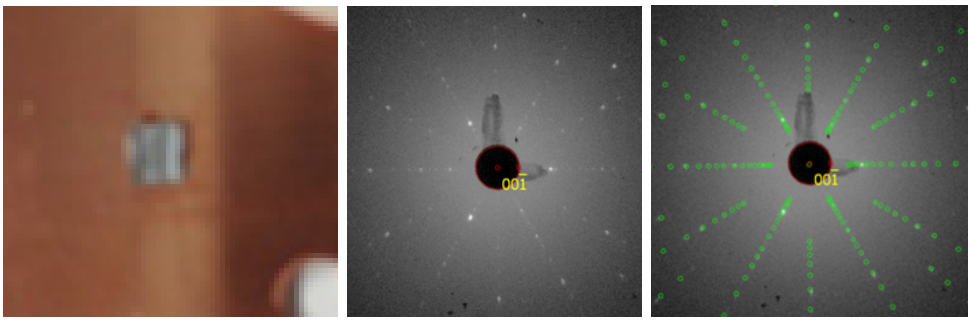

Figure 6.5: (a) Real image of $BiSbTeSe_2$ on a copper sample holder. (b) x- ray diffraction pattern of (a). (c) Reflection peak simulation for the $R\bar{3}m$

6.5.1 $BiSbTeSe_2$ Thin Sample

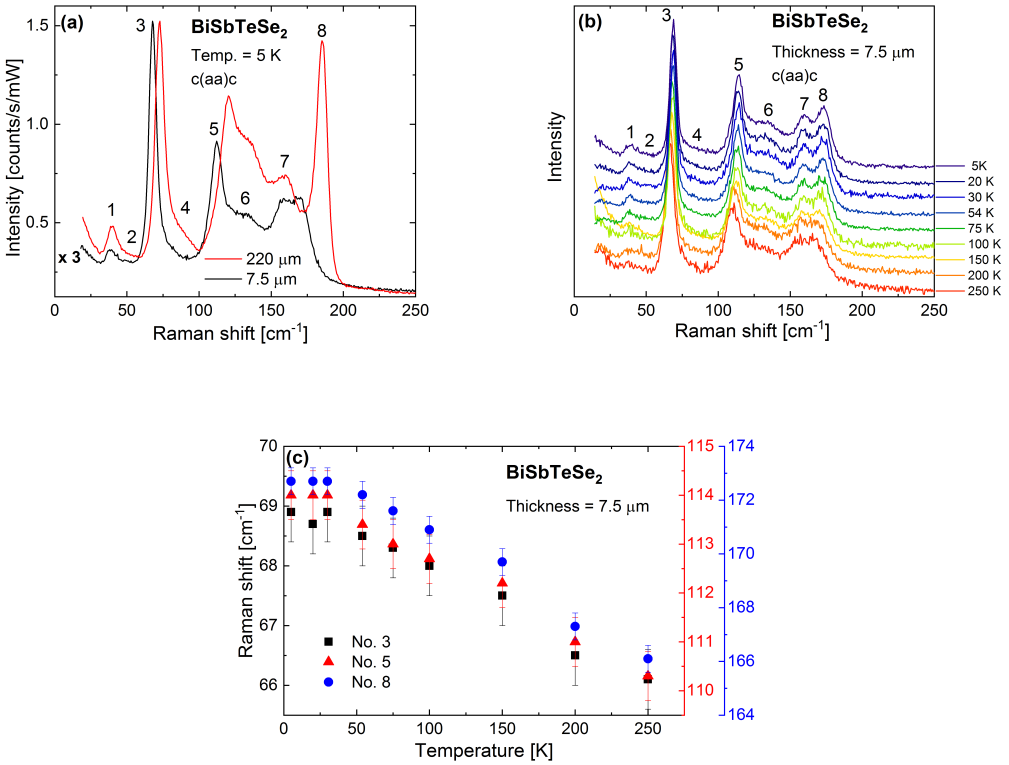

Figure 6.6: (a) Raman spectra of $BiSbTeSe_2$ at 5K in c(aa)c geometry for 220 and 7.5 μm thick samples. (b) Temperature dependent Raman spectra of the 7.5 μm $BiSbTeSe_2$ sample, measured in c(aa)c geometry. Numbers denote the phonon mode assignment from the previous section. (c) Raman shifts of the 7.5 μm thick sample for modes number 3, 5, and 8.

The sample thickness of $BiSbTeSe_2$ was reduced from 220 μm to 7.5 μm (estimated by the periods of IR fringes). The most of the phonon mode energies reveal a red-shift by reducing the thickness, see Fig. 6.6 (a). Mode No. 8 shows the strongest thickness induced shift of 16 cm^{-1} (2 meV). Interestingly, mode No. 7 is not effected by this, although it is also an out-of-plane A_1- mode. Temperature dependence show for the modes No. 3, 5, and 8 a much stronger pronounced saturation of the Raman shift as for the thicker sample, Fig. 6.6c.

6.6 Resistivity

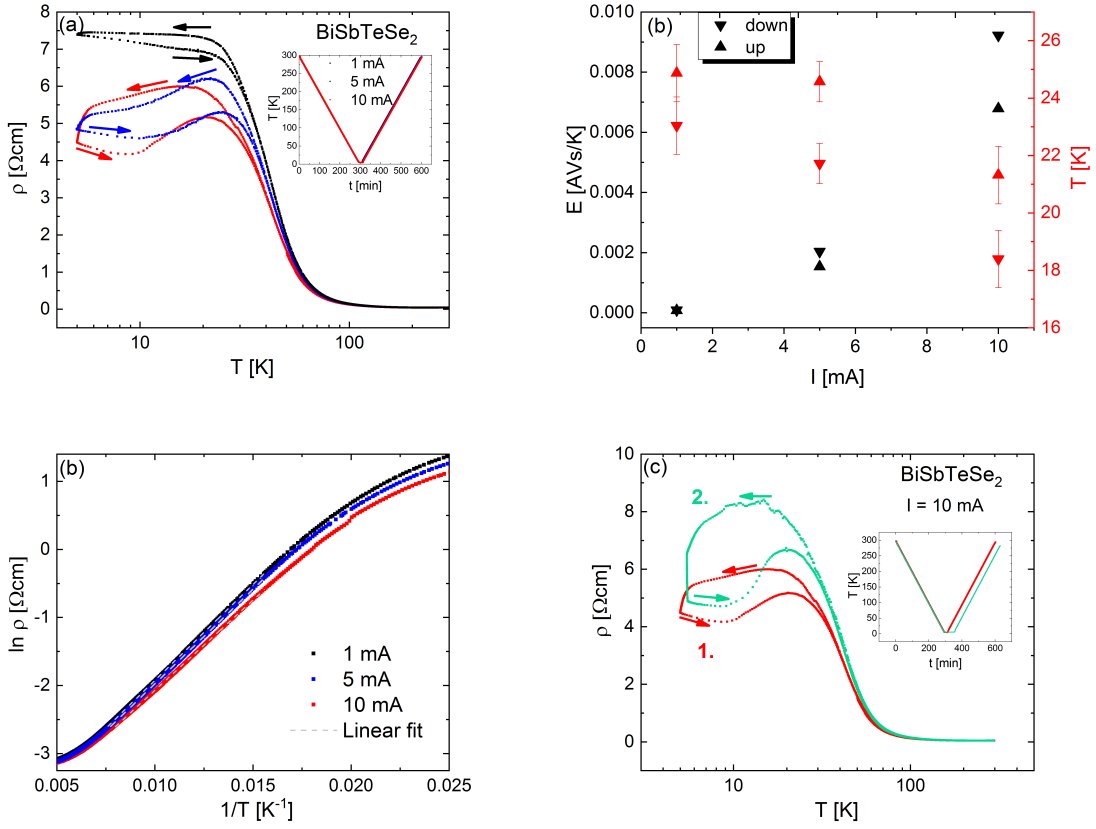

Figure 6.7: (a) Resistivity data of $BiSbTeSe_2$ for 1 mA (black), 5 mA (blue), and 10 mA (red), respectively. The inset shows the time dependent temperature change. (b) Linear fit for (a) to calculate the activation energy Δ. (c) Repeated resistivity measurement measured with 10 mA and a longer duration at the lowest reached temperature, see inset.

Fig. 6.7 a) shows the resistivity for different applied currents. Below $\sim$ 45 K the three resistivity curves start to deviate from each other. Additionally, the difference between down and up measurement becomes larger for higher currents. To exclude measurement time induced effects the cooling and the heating rate was kept constant, see inset Fig. 6.7 a). Above $\sim$ 45 K the data is fitted by the Arrhenius law to compare the activation energies. The following assumption holds

$$\frac{1}{\rho} \sim \sigma \sim n \sim \exp^{-\frac{\Delta}{k_B T}}, \tag{6.3}$$

where σ is the conductivity, n is the population number, Δ is the activation energy and k_B is the Boltzmann constant. Furthermore,

$$\ln \rho \sim \frac{\Delta}{k_B T}, \tag{6.4}$$

where $\Delta \cdot k_B$ is the slope of the fitted function,* Fig. 6.7 b). The obtained values of $\Delta_{1mA} = 24.26 \pm 0.03$ meV, $\Delta_{5mA} = 23.9 \pm 0.03$ meV and $\Delta_{10mA} = 22.8 \pm 0.03$ meV are in the reported range between 22 and 30 meV and can vary from batch to batch [201]. Nevertheless, in the fitted range of 64 and 130 K a current induced decrease of Δ is observed and can be explained by the additional charge carriers which reduces the transition barrier. A decrease of ρ is also observed when the measurement is fixed at an arbitrary temperature below $\sim$ 45 K, demonstrated in Fig. 6.7 c). The inset shows the different measurement times for the lowest reached temperature for 10 mA. Measurement No. 1 and 2 shows different amplitudes, but reveal qualitatively similar features. A possible explanation is the formation of puddles at low temperatures and their spatial reorientation with time. Due to band deformation an electron inside a puddle may only be in a local minima of the ground state. However with time, at low temperatures the electron can tunnel into an available lower energy state. Mobile puddles which change the macroscopic behavior would explain the quantitatively different appearance of measurement No. 1 and 2.

6.7 BiSbTeSe$_2$ White-Light Pump-Probe

Fig. 6.8a and b summarizes the wavelength- and time-dependent results for BiSbTeSe$_2$ at 294 K. For a easier discussion, times T_i at extreme values and the corresponding times in between ΔT_{ij} are defined in Fig. 6.8b. At negative probe delay of the differential reflection signal is detected, caused maybe by probe pulses from earlier times, reaching before the pump pulse and before the sample recovers. Thus, the positive probe delay signal is a superposition between the present pump pulse and a background induced by the pump, Fig. 6.8b (similar effects are observed in Ref. [226]). After a fast rising time of 0.05 ps of the differential reflection signal reaches the first maximum at T_1. Within ΔT_{12} a combination of non-oscillatory-decaying of $\sim$ 5 ps plus high-frequency-oscillatory signal is observed (compare $Bi_{1.5}Bi_{0.5}Te_{1.8}Se_{1.8}$ in Ref. [227]). Fig. 6.8c shows the wavelength independent oscillation subtracted by the exponential decay which reveals a coherent oscillation of the period of 0.5 ps (66.7 cm^{-1}). This is consistent with the Raman observations of the longitudinal A_{1g} in the previous sections. In the literature reported pump-probe studies also observe A_{1g} coherent optical

*The result in J is in the following converted to eV, 1 eV = $1.602176634 * 10^{-19}$ J.

phonon in $Bi_{1.5}Sb_{0.5}Te_{1.8}Se_{1.2}$, Bi_2Se_3, Sb_2Te_3, and Bi_2Te_3 [226–230]. For probe energies below 1.636 ± 0.002 eV (757.68 nm) the signal becomes negative after 2.6 ps and recovers again after 7.4 ps at T_2, normally a sign for photo-induced bleaching. Below 560 nm (2.21 eV) an additional increase is observed. For all wavelength a increase of intensity is observed at $T_3 \sim 18$ ps and at $T_5 \sim 130$ ps with a saddle point $T_4 \sim 30$ ps in between. T_5 and the decay after is strongly energy dependent . ΔT_{23} and ΔT_{34} are both 15 ps which is corresponding to 0.033 THz (0.13786 meV) and can be identified as a coherent acoustic phonon [226].

In summary, the signal above a few ps is interpreted as coherent lattice vibration. Whereas, at smaller delay times it is attributed to a combination of coherent lattice vibrations and energetically or thermally excited carriers. These results are in line with similar experiments on Bi_2Se_3 reported in Ref. [226]. The measurement indicates that in $BiSbTeSe_2$ in the ultrashort regime, with a rising time of ~ 0.05 ps, is due to the thermalization and energy relaxation of hot carriers.

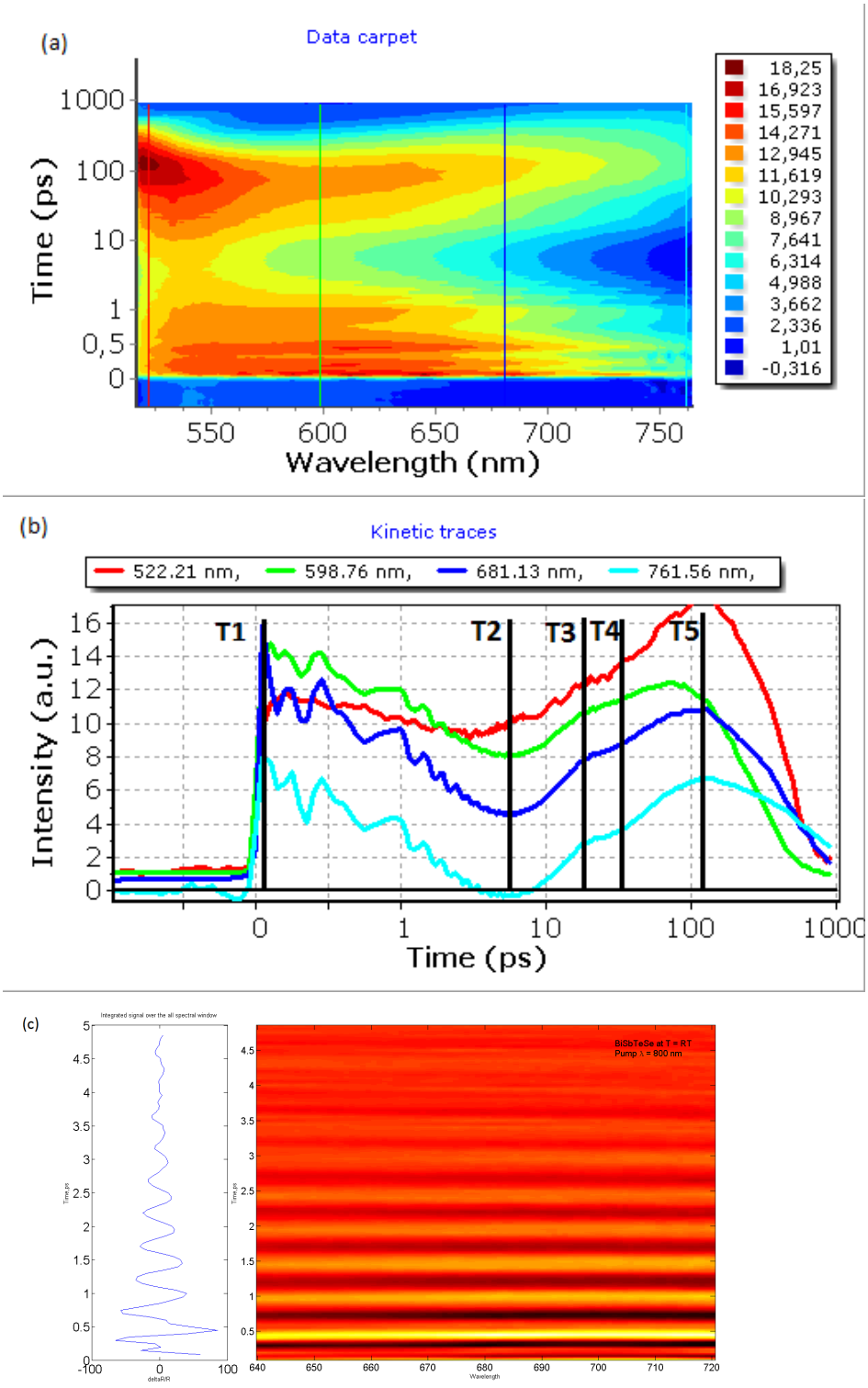

Figure 6.8: (a) Photoinduced change of $BiSbTeSe_2$ versus pump-probe time delay for selected wavelength from 0 to 10 ps. (b) Contour plot of the pump-probe time delay for the first 5 ps, subtracted by the exponential decay, versus the measured wavelength.

Chapter 7

7- Atom Armchair Graphene Nanoribbons

The opening of a band gap in graphene nanoribbons induces novel optical and electronic properties, strongly enhancing their application potential in nanoscale devices. Knowledge of the optical excitations and associated relaxation dynamics are essential for developing and optimizing device designs and functionality. Here we report on the optical excitations and associated relaxation dynamics in surface aligned 7-atom wide armchair graphene nanoribbons as seen by time-resolved spontaneous Stokes and anti-Stokes Raman scattering spectroscopy. On the anti-Stokes side we observe an optically induced increase of the scattering intensity of the Raman active optical phonons which we assign to changes in the optical phonon populations. The optical phonon population decays with a lifetime of $\sim$ 2 ps, indicating an efficient optical-acoustic phonon cooling mechanism. On the Stokes side we observe a substantial decrease of the phonon peak intensities which we relate to the dynamics of the optically induced exciton population. The exciton population shows a multi-exponential relaxation on the hundreds of ps time scale and is independent of the excitation intensity, indicating that exciton-exciton annihilation processes are not important and the existence of dark and trapped exciton states. Our results shed light on the optically induced phonon and exciton dynamics in surface aligned armchair graphene nanoribbons and demonstrate that time-resolved spontaneous Raman scattering spectroscopy is a powerful method for exploring quasi-particle dynamics in low dimensional materials.

7.1 Introduction

Graphene based nanostructures have been attracting widespread attention in research and industry [231–233] since the first graphene electronic device was demonstrated in 2004 [234]. Of particular interests are the spatially confined strips of graphene monolayer, dubbed graphene nanoribbons (GNRs). Due to one-dimensional quantum confinement and edge dependent effects, these GNRs display remarkable chemical, electrical and optical properties, including a width tuneable band gap, excitonic optical transition, and potentially room temperature ballistic transport [235–237]. These novel properties result in many potential applications in nanoscale electronic transistor devices [238], optical modulators [239] , quantum gates [240], and infrared photodetectors [241]. The development of applications, as well as the fundamental understanding of the GNRs electronic properties requires knowledge of the fundamental optical excitation properties and energy relaxation mechanisms in these one dimensional systems. Over the past, electronic structures and excitation properties of GNRs have been investigated via conventional spectroscopic techniques such as X-Ray absorption [242], scanning tunneling [243], and photoelectron spectroscopy [244]. In addition the electronic structure has been studied from a theoretical point of view [245, 246]. The general steady state features such as the band gap structure of GNRs are reasonably well understood by now. Studies on the dynamical non-equilibrium properties of GNRs are, however, more scarce most likely due to lack of sufficiently sensitive experimental techniques for these single layered materials. Recently, polarized reflectance measurements combined with ab initio calculations [237, 247] demonstrated that the optical absorption in armchair graphene nanoribbons (AGNRs) are dominated by excitonic transitions. The investigation of the electronic relaxation dynamics in graphene based nanomaterials has been limited to a few cases reporting transient absorption spectroscopy measurements of solution solvated and suspended samples [248], and time resolved terahertz studies of multilayer aggregated GNRs [249]. The development of methods to grow aligned GNRs on gold surfaces, and techniques to transfer the GNRs to nonmetallic substrates [250] opened the possibility to study the properties of GNRs in a more controlled manner, including for instance symmetry aspects using polarization sensitive spectroscopies. Steady state Raman spectroscopy has been proven to be a versatile tool in the characterization of carbon and graphene based materials [251]. It allows to determine the number and orientation of layered graphene, yields information on strain, doping, disorder, and provides a good method to assess the quality of graphene based materials as well as the nature of edges and functional groups in

functionalized graphene. In addition to this, the time-resolved variant of Raman spectroscopy is a powerful method to investigate both incoherent phonon relaxation as well as electron-phonon coupling and electronic dynamics [252]. In this report, we applied these spectroscopic techniques to study the optical transition properties and in particular the optically induced phonon and electronic dynamics in the 7-atom wide armchair graphene nanoribbons (7-AGNRs) aligned on a silica/silicon substrate. We demonstrated that not only the phonon population, but also the excitonic relaxation dynamics, can be extracted from the optically induced changes in the Raman spectrum. To achieve the latter, we make use of the strong resonant enhancement of the optical phonon Raman scattering due to excitonic transitions. The observed fast phonon creation and relaxation originates from an efficient exciton-phonon and optical-acoustical phonon coupling, respectively, indicating of an efficient energy dissipation in this material. The observed strong resonant optical transition and non-exponential nature of the excitonic relaxation in this one dimensional system evidences the dominated existence of dark and trapped exciton states. These knowledge provide fundamental understanding of the GNRs system toward further optimizing electronic device application.

7.2 Experimental

7-AGNRs were synthesized using the well-established bottom-up fabrication approach on Au (788) surfaces which exhibit a regular arrays of narrow (111) terraces dictating the direction of growth [253] and yielding high quality, densely aligned ribbons. The transfer from the Au (788) substrate to the insulating silica/silicon substrate was performed by the alignment-preserving bubbling transfer method based on an electrochemical delamination process. The bottom up syntheses process and our sample transfer method guarantees that we have monolayer 7-AGNRs film [254]. Steady state (one laser beam) Raman spectra of 7-AGNRs were performed using a micro-Raman setup equipped with a tandem triple spectrometer (Spectroscopy & Imaging GmbH) and LN2 cooled CCD (PyLoN 100; Princeton Instruments). An optical parametric amplifier (OPA, Light conversion), pumped by a single-unit amplified femtosecond laser (Pharos, Light conversion) running at a repetition rate of 100 kHz provided wavelength tuneable (400 nm to 800 nm; 1.5-3.1 eV) picosecond pulses ($\sim$ 2 ps) as excitation source. The excitation pulses were spectrally cleaned and narrowed (full width a half maximum (FWHM) $\sim$ 10 cm^{-1}) using a home build pulse shaper. The pulses were focused on the sample with a 20 times micro objective, and Raman signals were collected in a backscattering geometry. To avoid sample degradation, samples were mounted in a

cryostat pumped down to 10^{-5} mbar. Time-resolved measurements (Fig. 7.1(a)) of 7-AGNRs were performed with the same setup by introducing a pump laser pulse (300 fs) provided by a second OPA (ORPHEUS, Light conversion) pumped by the same amplified laser. Details of the time-resolved spontaneous Raman spectroscopy technics and methods have been described elsewhere [255]. The samples were pumped with laser wavelengths of 590 nm (2.1 eV) and 490 nm (2.5 eV) respectively, and Raman signal were collected using 512 nm (2.4 eV) probe pulses (Fig. 7.1(c)). Both the pump and probe light polarization are parallel to the long axis of the AGNRs. In order to avoid optical damage of the samples and improve the signal to noise ratio, the laser spot sizes on the sample were defocused to ~ 60 μm. The back reflected Raman scattering signals were re-collimated with an additional telescope lens group before entering the spectrometer. Time-resolved measurements were performed using pump pulse fluencies ranging from 7.5 μJ/cm^2 (0.47×10^{14} photons/cm^2) to 38.2 μJ/cm^2 (2.37×10^{14} photons/cm^2). Under these conditions no signs of damage to the sample are observed after hours of measuring. At higher fluencies ($> 50\mu$J/cm^2) we observed an slow ingrowth of a broad band 'background' signal with time and a slowly decreasing phonon peak intensity indicating damage to the sample.

7.3 Results and discussion

Fig. 7.1(b) presents typical steady state polarized Raman scattering spectra of the 7-AGNRs on Stokes side. The phonon scattering peak at around 521 cm^{-1} originates from the silica/silicon substrate and provides a good reference for the measurements. The highly orientated nature of our samples is demonstrated by the strong enhancement ($\times10$) of the Raman signal when the incoming light is polarized along the ribbons [250]. The G- and D-like modes typical for all graphene related materials are clearly observed in the spectra. The C-C stretching G-like mode, located at 1608 cm^{-1}, corresponds to a carbon-carbon bond stretching mode along the ribbon. The D-like mode related to the armchair edge termination of GNRs [256] is found at 1345 cm^{-1} and is weaker than the G-like mode. Other vibrational Raman peaks [257], like the breathing mode related to the ribbon width expansion is found at 398 cm^{-1}, and the confinement derived vibrational modes at 1255 cm^{-1} and 1266 cm^{-1} were also well resolved. In general, the spectra measured with the pulsed laser are fully consistent with previous results measured on 7-AGNRs on insulating and metallic substrate surface with continuum lasers [250]. To investigate resonance effects due to optical transitions in 7-AGNRs, wavelength dependent Raman scattering measurements were performed. Fig. 7.1(c)

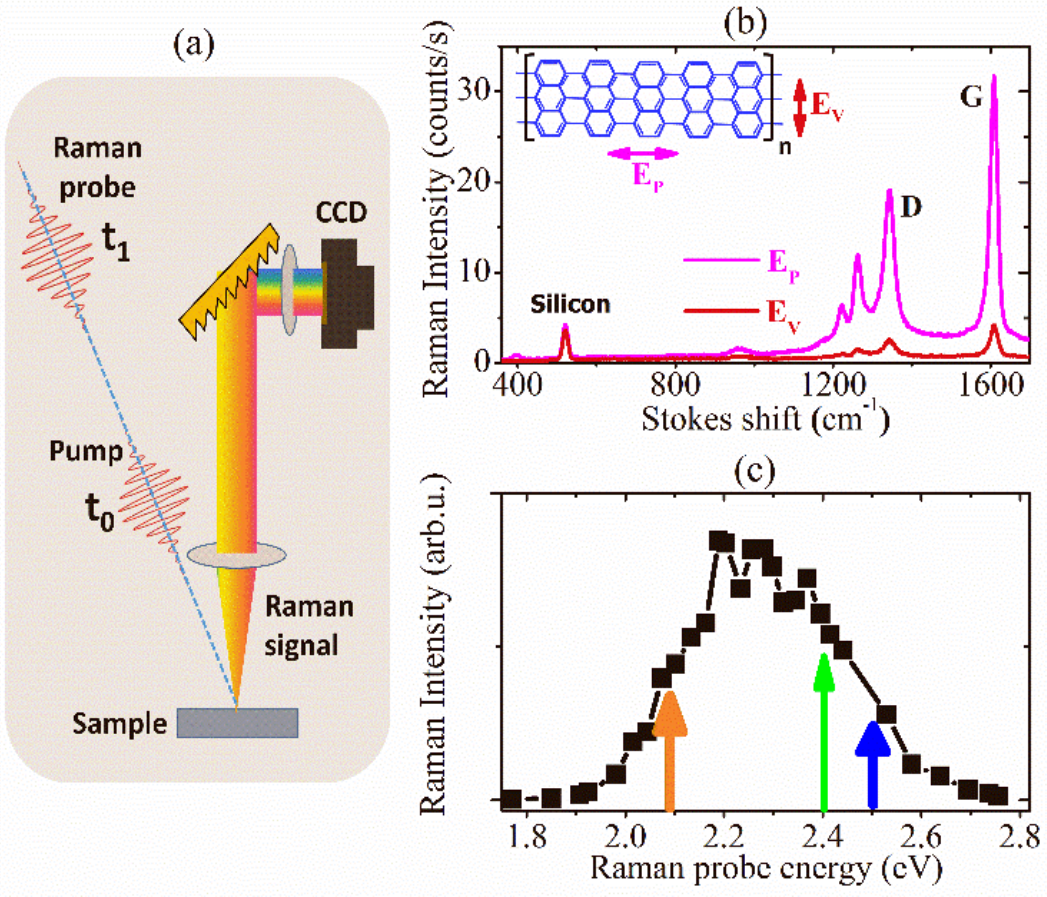

Figure 7.1: (a) Illustration of the spontaneous Raman scattering experiments. Steady state measurement is obtained when the pump beam is blocked. (b) Steady state Raman scattering spectra of the 7-AGNRs on silica/silicon recorded with picosecond pulsed laser at 512 nm, E_P indicates that the polarization of laser pulse is along the ribbons, E_V indicates that the polarization of laser pulse perpendicular to the ribbons. (c) Energy dependence of the Raman intensity of the phonon G peak, showing a strong resonant enhancement of the Raman scattering. Dark yellow and blue arrows indicate the pump energies used for the time-resolved experiments, green arrow indicates the Raman probe energy used for the data shown in (a) and for the time-resolved experiments.

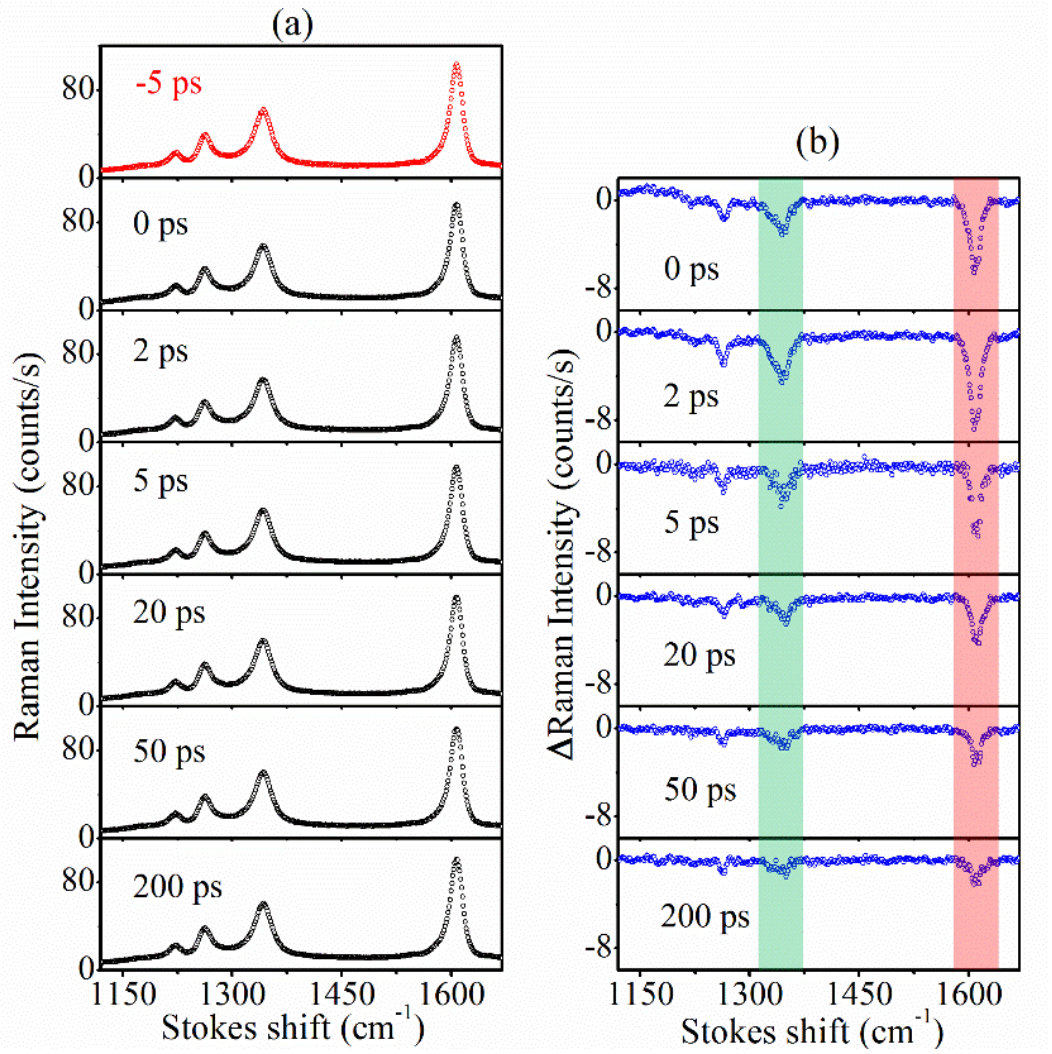

Figure 7.2: Time-resolved spontaneous Raman scattering spectra of the 7-AGNRs recorded on Stokes side, with pump energy at 2.1 eV and Raman probe energy at 2.4 eV. (a) Raman scattering intensity spectra at different delay times after optical excitation. (b) Difference spectra obtained by subtraction the spectrum at $\sim$ 5 ps from each spectrum in (a) at different corresponding delay time. The color bars indicate the integration regions used in the analysis of the transient behaviour.

depicts the resonance profile of the integrated intensity of the G-like mode. A clear resonant profile was observed, centered at $\sim$ 2.3 eV with a FWHM of $\sim$ 0.4 eV. The observed resonant profile resembles the imaginary part of the dielectric function of 7-AGNRs on a gold substrate, which was interpreted in terms of an excitonic transition [237]. The excitonic transition width observed here with Raman is much broader than those of nanotubes, the reason for this most likely originate from the fact that two electronic transitions (E11 and E22) are involved [237] combined with inhomogeneous broadening due to a broad length distribution [258] and possibly defects induced in the sample transfer process. The fundamental energy gap for 7-AGNRs on a gold surface is strongly reduced due to polarization screening by the substrate compared to the theoretically calculated energy gap of $\sim$ 3.7 eV [237]. In our case one expects a much weaker screening by the silica/silicon substrate, and hence a substantially higher single particle band gap. Indeed, it has been demonstrated that the reduced screening for 7-AGNRs aligned on an Au-Silicon alloy substrate leads to a band gap of 2.7 eV [259]. Since the dielectric constant of our silica/silicon substrate is even lower, we expect a single particle band gap much closer to the theoretical value of 3.7 eV. In view of this we can safely assign the observed resonance around 2.3 eV in the Raman scattering experiment to excitonic transitions associated with an exciton binding energy larger than 1 eV.

Fig. 7.2a depicts the time-resolved Stokes spectra after optical excitation at 590 nm (2.1 eV), with excitation laser intensity around 1.2×10^{14} photons/cm^2. To more clearly exhibit the pump induced effects on the Raman spectra, Fig. 7.2(b) shows difference spectra obtained by subtracting the -5 ps spectrum (top panel Fig. 7.2a) from the time delayed spectra in Fig. 7.2a. As is clear from the figures, the Raman spectra show an overall decrease of scattering intensity for all time delays, which recovers on a hundreds of ps time scale. Similar spectral changes were also observed upon excitation at higher photon energy at 490 nm (2.5 eV) (Fig. S2 in the Appendix). These observations are in contrast to the usual observations in time-resolved spontaneous Raman experiments of an increasing optical phonon scattering intensity originates from an, through the electron-phonon scattering processes, optically increased phonon population [260–262].This surprising result can be understood in terms of optically induced changes in the Raman resonance efficiency which allows extraction of the electronic relaxation dynamics from our data, as we will elaborate later on in this report. To obtain a more detailed insight into the dynamics, the changes in the phonon scattering intensities of the D-like and G-like bands are integrated (over regions indicated by the colored areas in Fig. 7.2b) for each time delay.

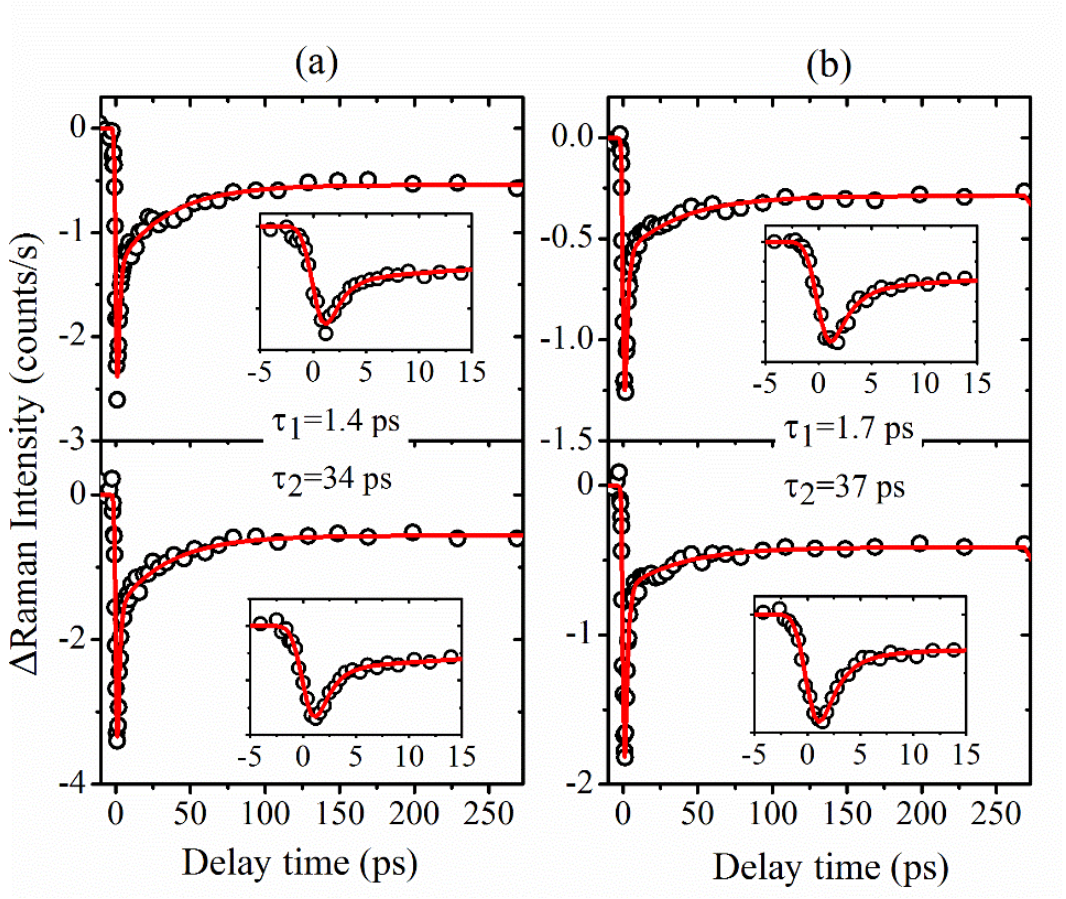

Figure 7.3: Decay dynamics of the phonon peak D-like (top panels) and G-like (bottom panels). (a) Dynamics observed at the excitation wavelength of 590 nm (2.1 eV). (b) Dynamics observed at the excitation wavelength of 490 nm (2.5 eV). Black circles represent the experimental data, red lines represent a global fitted. Insets show the short time dynamics.

The dynamics of the D-like and G-like bands are plotted in Fig. 7.3 and are found to be identical: the changes in the Stokes spectra show a substantial decay within 100s of ps, but only fully recover on a ns time scale, which is out of our detection window. Multi-exponential decay functions are required to fit the data, where a global fitting of the D-like and G-like responses yield decay times of 1.4 ps and 34 ps for the 2.1 eV pumped spectra, and 1.7 and 37 ps for the 2.5 eV pumped spectra. The 20-40 ps decay dynamics observed is much longer than the general optical phonon population dynamics in graphite and graphene related systems [260, 262–264] which are in the time range of 1-2 ps. On the other hand, the lifetime constants obtained here are comparable to those of dynamics in various graphene nanotubes [265–268], where the excitons dynamics typically shows a double exponential decay with lifetimes of 1-15 ps 30-90 ps, respectively. This, together with the resonant nature of the Raman scattering, strongly suggests that an exciton related relaxation mechanism is responsible for the observations.

To test if any many-body relaxation mechanisms are involved in the decay of the Stokes response, excitation intensity dependent measurements are carried out with the pump photon energy at 2.1 eV. The measured results are presented in Fig. 7.4. Since dynamics form D-like and G-like peaks are generally the same, only the average of the D-like and G-like responses is plotted. For pump excitation densities $< 1.2 \times 10^{14}$ photons/cm^2 a linear increase of the signal is observed which seems to saturate above this value (see inset in Fig. 7.4(a)). Fig. 7.4a, which shows the same data normalized to the maximum response, indicates that there is no pump excitation power dependence in the dynamics, demonstrating the absence of many-body processes in the transient behavior of the signal.

It is clear from the above that the dynamics of the phonon population cannot be extracted from the Stokes side Raman spectra. In order to obtain insight in the phonon population experiments on anti-Stokes side, using identical experimental conditions with a pump energy of 2.1 eV and pump intensity of 1.2×10^{14} photons/cm^2. The recorded time dependent spectra are presented in Fig. 7.5, in the same manner as those on Stokes side in Fig. 7.2. Indeed a pump induced enhancement of the phonon scattering signals is observed for both D-like and G-like responses on the anti-Stokes side. The dynamics show a very fast response, with ingrowth times faster than our time resolution and decay time of $\sim$2 ps.

The integrated intensity dynamics for the D-like and G-like responses in Fig. 7.5a are shown in Fig. 7.6 a, both have identical relaxation dynamics. A global single exponential fit yields a decay constant of 1.9 ps, which can be interpreted as the

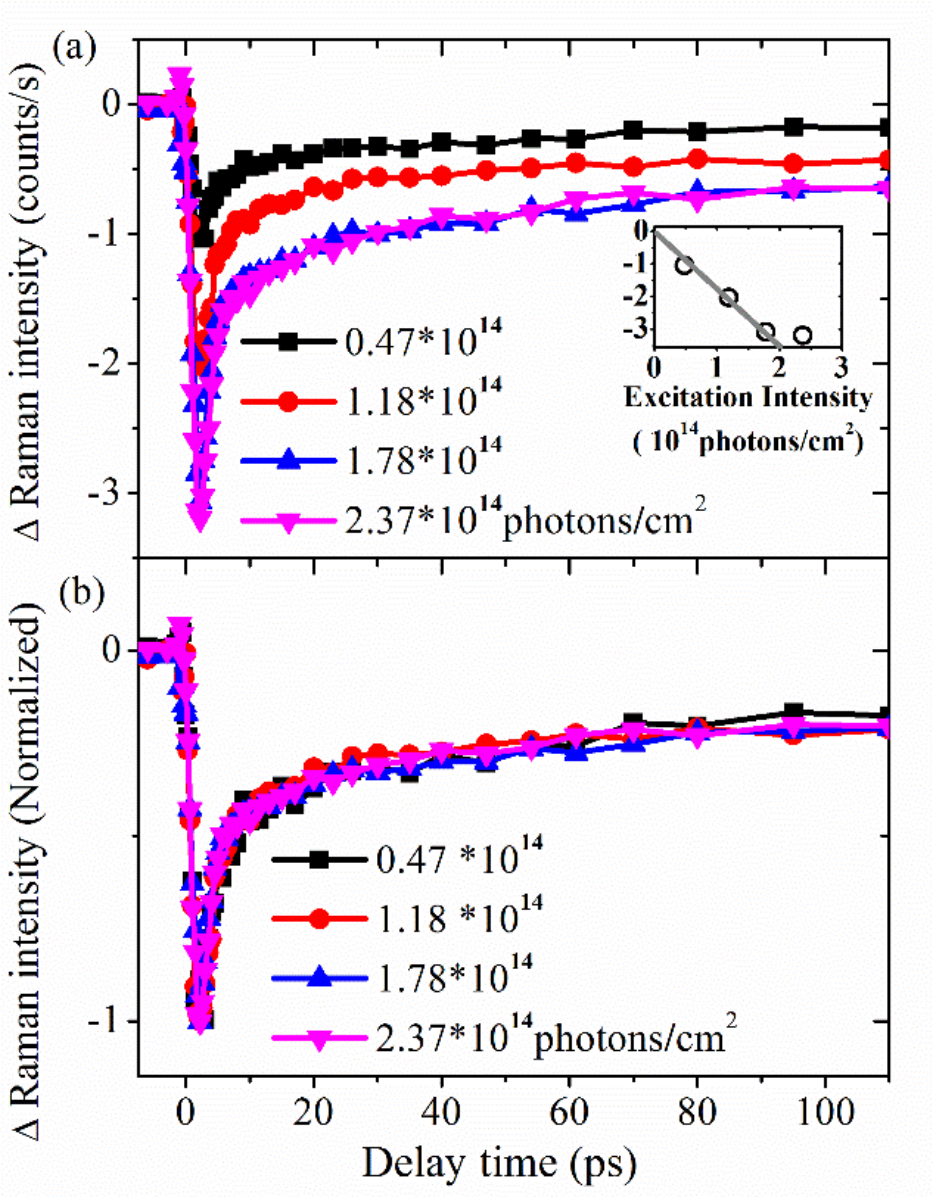

Figure 7.4: Pump (2.1 eV) excitation intensity dependence of the decay dynamics. The data represent the averaged response of the D-like and G-like bands. In a) the raw data are presented and in b) data are normalized to show the absence of the pump intensity dependent dynamics. The inset in a) shows the pump excitation intensity dependence of the amplitude at a delay of 2 ps.

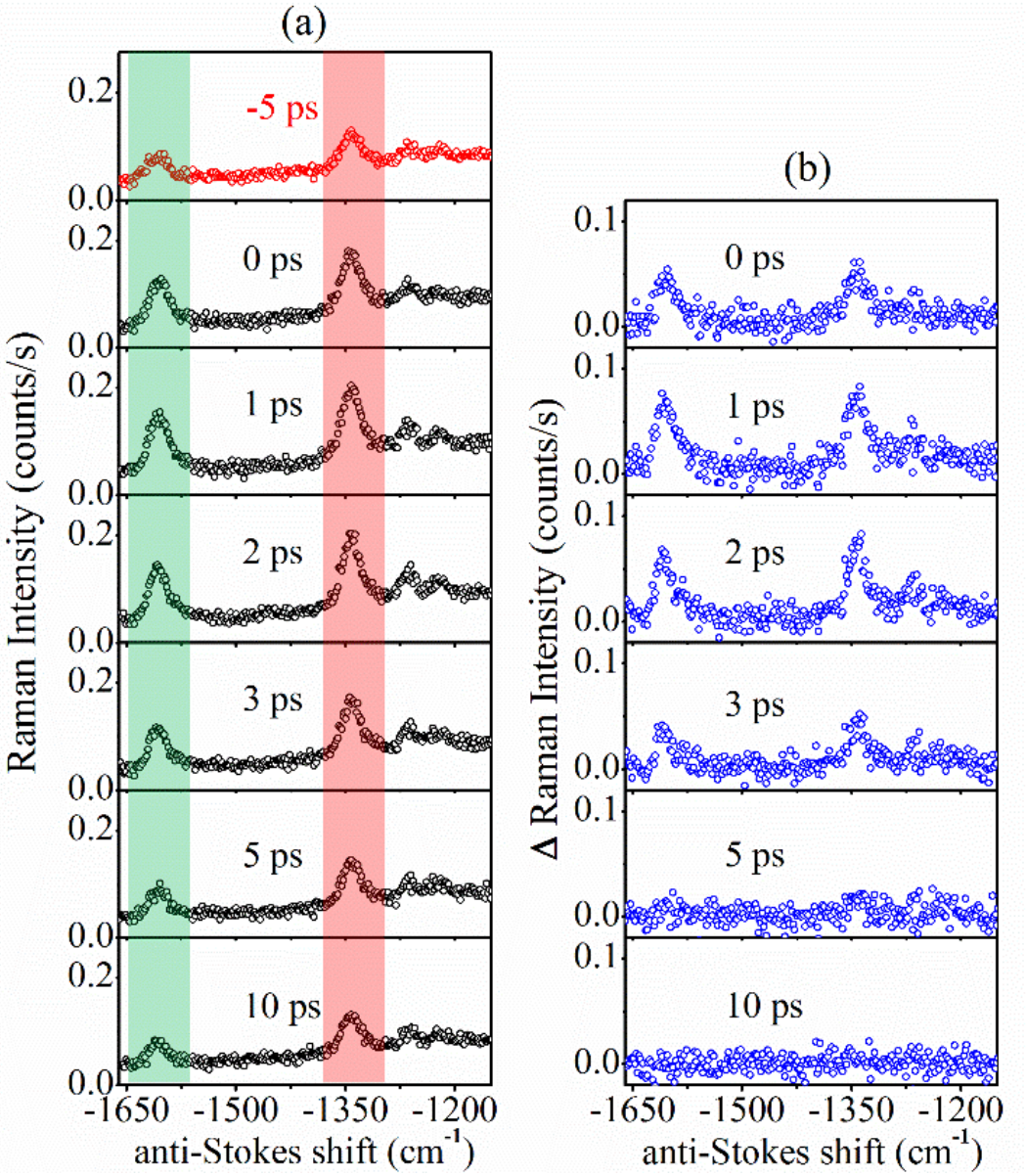

Figure 7.5: Time-resolved spontaneous Raman scattering spectra of the 7-AGNRs recorded on anti-Stokes side. a) Raman scattering intensity spectra at different delay times after optical excitation at 2.1 eV. b) Pump induced difference spectra obtained by subtraction the spectrum at ∼5 ps from each spectrum in a) at different corresponding delay times.

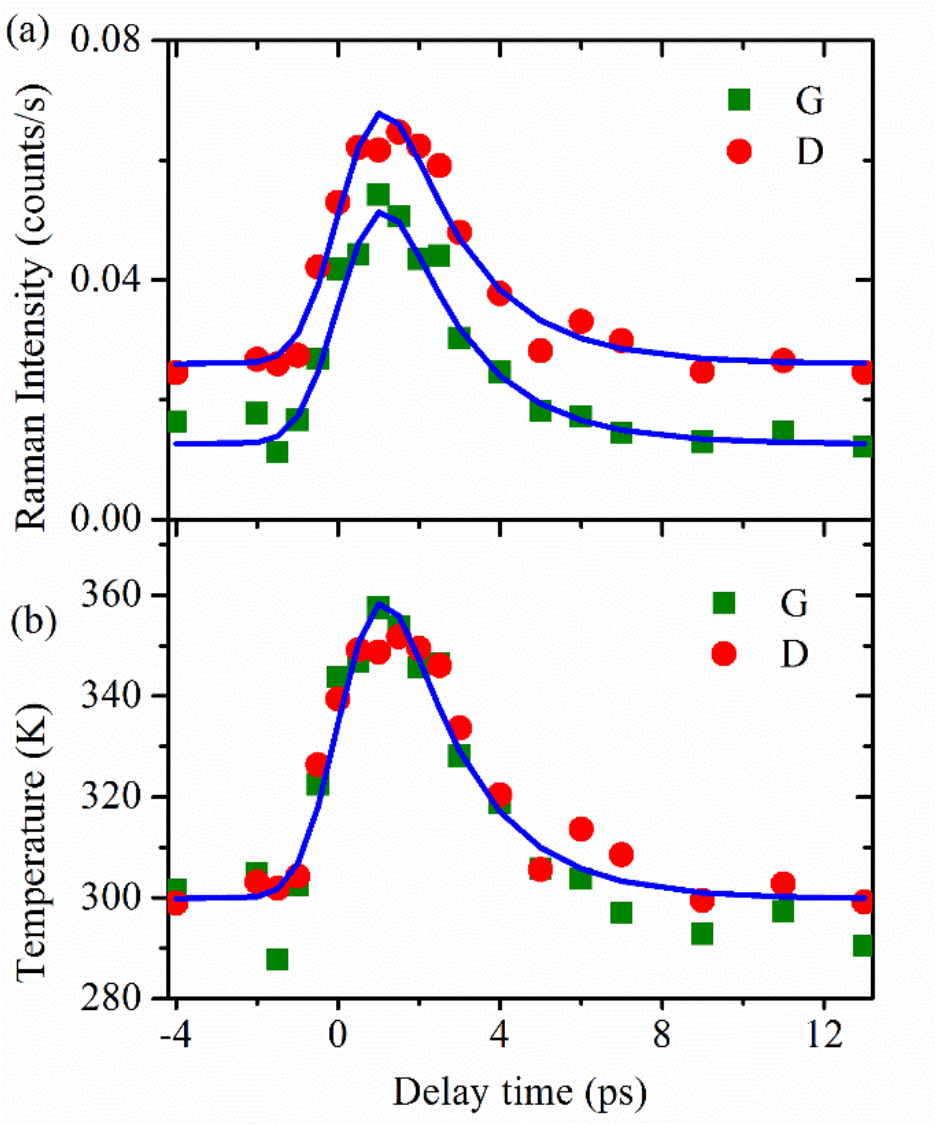

Figure 7.6: Phonon population dynamics of 7-AGNRs extracted from anti-Stokes spectra. a) Dynamics for peak D- and G-like (symbols: experimental data; lines: globe single exponential fit). b) Calculated D- and G-like transient phonon temperatures.

lifetime of the optical phonons. In principle, phonon temperatures can be obtained from the signal ratio between Stokes and anti-Stokes side, based on the detailed balance resulted from fluctuation-dissipation theorem. However, due to the strong resonance Raman effects this is not trivial. We therefore estimated the transient optical phonon temperature using the reasonable assumption (see supplementary information in the Appendix) that before time zero the phonon temperatures are equal to the environment temperature ($\sim$ 300 K). As indicated in Fig. 7.6b, the transient temperatures estimated from both D-like and G-like peaks are, within the experimental accuracy, identical and reach a maximum value of 350 K within our time resolution. They decay to the equilibrium temperature within 2 ps as the optical phonons are depopulated through optical-acoustical phonon scattering. As have been observed from the dynamics of the optical phonon peaks D-like and G-like, the decay behaviors on anti-Stokes side matches the phonon population dynamics, while the decay behaviors on Stokes side matches the electronic relaxation time scale in graphene based materials. To further clearly derive these relations, we assume that the pump induced phonon signal changes are contributed by both of the phonon population and the Raman susceptibility changes. Ignoring other constant parameters, simply the observed Raman signals on the Stokes side [16] can be expressed as:

$$I^S_{un-pumped} = |\chi_R|^2(1 + n_p) \tag{7.1}$$

where χ_R is the phonon Raman susceptibility tensor and n_p is the statistical phonon population number. After optical excitation, the time dependent change of $|\chi_R|^2$ and np is $\Delta|\chi_R|^2(t))$ and $\Delta n_p(t)$ respectively. Thus Raman signal after optical excitation is:

$$I^S_{pumped} = (|\chi_R|^2 + \Delta|\chi_R|^2(t))(1 + n_p + \Delta n_p) \tag{7.2}$$

such that the pump induced difference signal is

$$\Delta I^S = I^S_{pumped} - I^S_{un-pumped} = I^S_{pumped} = (|\chi_R|^2 + \Delta|\chi_R|^2(t))\Delta n_p(t) + (1 + n_p)\Delta|\chi_R|^2(t) \tag{7.3}$$

Since $\Delta n_p(t) << 1$ and $n_p << 1$, formula (3) can be reduced to

$$\Delta I^S = \Delta|\chi_R|^2(t) \tag{7.4}$$

Clearly this indicates that the signal changes on Stokes sides are dominated by the Raman tensor changes. The decreasing of Raman susceptibility can easily be understood from resonant properties of the Raman process, based on a two-state mode. Since the resonant Raman scattering signals are dictated by the first step of resonant optical transition, a bleach of the electronic ground state, or state filling on the excited state, can decrease the optical transition probabilities and thus reduces the Raman signals. For a simplified two energy level model system, we demonstrate that the Raman tensor square changes has simple relation to the hole population probability (Supplementary information in the Appendix) ρ, written as:

$$\Delta|\chi_R|^2(t) = -4\kappa^2\rho \tag{7.5}$$

where κ is a constant, related to the optical transition matrix elements involved in the Raman process. Thus (7.3) becomes:

$$\Delta I^S = -4\kappa^2\rho \tag{7.6}$$

which indicates that, on the Stokes side, the difference signal observed is linearly related to the electron (hole) density. Therefore, the observed decay of Raman signals can be attributed to the electronic relaxation dynamics. Similarly, on anti-Stokes side, the pump induced difference signal can be expressed as:

$$\Delta I^{AS} = \Delta n_p(t)|\chi_R|^2(t) + n_p(t)\Delta|\chi_R|^2(t)... \tag{7.7}$$

In a condition that the phonon population $\Delta n_p(t)$ induced by the pump is larger comparing to the equilibrium phonon population np, while $\Delta|\chi_R|^2(t))$ is only a few percent of $|\chi_R|^2$ (which is true for most of experiments), i.e. specifically we have

$$\frac{\Delta n_p(t)}{n_p(t)} >> \frac{\Delta|\chi_R|^2(t)}{|\chi_R|^2} \tag{7.8}$$

Thus the last two terms on the right side of (7.3) can be ignored, and reduces to

$$\Delta I^{AS} = |\chi_R|^2(t)\Delta n_p(t) \tag{7.9}$$

This is exactly the expected result for the phonon population dynamics which can be observed from anti-Stokes side and is proportional to the signal intensity changes. From above simple analysis, we conclude here that in time-resolved spontaneous Ra-

man spectroscopy, phonon and electronic population dynamics can be observed from the anti-Stokes and Stoke side Phonon signal changes respectively. The optical phonons life time ($\sim$ 2 ps) in 7-AGNRs is found to be very similar to the dynamics observed in graphite and graphene nanotubes [262]. The main difference is in the observed temperature increase which is only 50 K in 7-AGNRs and can exceed 1000 K in graphite under similar excitation conditions [261]. Correspondingly, the phonons in 7-AGNRs also do not show any spectral dynamics such as the stiffening observed in graphite. These differences originate from the generation mechanism of the optical phonons. In the experiments on graphite the optically induced phonon population is created through relaxation of the highly excited free carriers to the conduction band minimum. In our experiments on the 7-AGNRs, however, the optical transitions are excitonic in nature and excited with only a limited amount of excess energy (i.e. close to resonant excitation), leading to a much lower raise of the phonon population, and thus phonon temperature, as compared to the graphite case. The most interesting observation reported here is arguably the decay dynamics of the Stokes spectra. Since we are directly exciting the excitonic transition responsible for the resonant Raman enhancement, the transient decay of the Stokes response directly reflects the exciton dynamics of the 7-AGNRs (see supplementary information). The reduction of the resonant enhancement is a direct consequence of ground state bleaching/excited state filling, i.e. of the reduction of the optical transition probability. We note that pump-probe Terahertz conductivity experiments on multi-layered AGNRs showed a short lived dynamics (1-2 ps) which has been assigned to free carrier relaxation followed by the formation of excitons. Though we observe a similar fast time scale of the initial decay of the Stokes response, its origin has a different nature. Our steady state resonant Raman results demonstrate the pure excitonic nature of the transitions around 2.3 eV in 7-AGNRs, therefore one does not expect any substantial density of free carriers directly after pump excitation. This is corroborated by the observation that the dynamics and amplitudes of the signal are nearly identical for both excitation energies used in the experiments (2.1 eV and 2.5 eV, see Fig. 7.3), and by the observation that the fast decay components recovers around 50% of the initial amplitude. The latter would not be expected if formation of excitons from free carriers is responsible for the initial fast decay since such a process does not substantially recover the optically induced ground state bleaching and thus the changes in the Raman resonance enhancement. Since 7-AGNRs are non-luminescent [250], exciton recombination must be non-radiative decay process. In carbon nanotubes, non-radiative exciton relaxation decay proceeds by passing through either long-lived defect related trap states [269] or through scattering into the optically

inactive dark exciton states [270]. Similarly in the AGNRs, one expects both trap and dark states. The dark states are derived from the E12 (upper valence band to second conduction band) and E21 (second valence band to lowest conduction band) transitions [245], whereas defect related trap states (both short and long lived) are expected to be present either originating from the bottom up growth process or from the electrochemical transfer process. The observed decay dynamics can now be understood as follows. After the initial creation of the free exciton population excitons populate both dark as well as trap states. Within the first 2 ps part of this population (short lived trap states) recombine, thereby reducing the transient response. In the following 30 ps dark excitons decay non-radiatively, leaving only the long lived trap exciton states, which amount to about 20% of the initial excited exciton population. These latter then decay on a nanosecond timescale which is out of our observation window. In most graphene based nanomaterials, such as the carbon nanotubes [271–273] and a cove-shaped graphene nanoribbons [248], diffusion controlled exciton-exciton annihilation dominates the exciton relaxation processes. Our experiments have shown that in our case many-body processes do not play a dominant role. This is understandable in view of the relatively short length [258] of the 7-AGNRs ($\sim$ 20 nm) compared to carbon nanotubes (exceeding 1 μm) and the mild excitation conditions used in our experiments: one does not expect a substantial amount of AGNRs with more than one exciton excited and hence no exciton-exciton annihilation process occurs. In summary, we have employed time-resolved spontaneous Raman spectroscopy to reveal the absence of exciton-exciton processes and a peculiar dependence of the Raman intensity on the Raman tensor for Stokes and anti-Stokes sides in 7-AGNRs. Optical excitation of the excitonic transitions leads to an enhanced optical phonon population through relaxation of the excess exciton energy by exciton-phonon scattering on a time scale faster than our temporal resolution ($\sim$ 1.5 ps). The decay times of the optical D-like and G-like phonon populations, originating from optical-acoustic phonon scattering, are found to be $\sim$ 2 ps, similar to values found in other graphene based nanomaterials and graphite. The exciton dynamics is directly reflected in the optical induced changes of Raman susceptibility. No evidence for diffusion controlled exciton-exciton recombination has been found, consistent with expectations. The exciton relaxation is found to be multi-exponential (decay constants $\sim$ 1.5 , $\sim$ 30 ps and $>$ 1 ns) reflecting the presence of short and long lived trap states as well as the expected dark states with a life time of $\sim$30 ps.

7.4 Acknowledgements

The here presented chapter has been published in

J. Zhu, R. German, B. Senkovskiy, D. Haberer, F. Fischer, A. Grüneis, Y. Ando, P. van Loosdrecht,
"Exciton and phonon dynamics in highly aligned 7-atom wide armchair graphene nanoribbons as seen by time-resolved spontaneous Raman scattering",
Nanoscale, **10**, 37, 17975-17982, 2018.

The 7-ARNRs were grown by B. Senkovskiy. J. Zhu and I did the Raman measurements and the analysis. The manuscript was prepared by J. Zhu and me with fruitful discussions and contributions from the co-authors.

7.5 Appendix

7.5.1 Phonon Temperature Estimation in Resonant TR-Raman

The Raman scattering signals form the Stokes side is

$$I_S = C_S \chi_S^2 (1 + n_p)(\omega - \Omega)^4, \tag{7.10}$$

and the anti-Stokes side

$$I_{aS} = C_{aS} \chi_S^2 n_p (\omega + \Omega)^4, \tag{7.11}$$

Where C_S , C_{aS} are constants including optical constants, geometry factors, laser intensity, detector sensitivity and other instrumental aspects, χ is the Raman tensor, n_p is the phonon population number, and ω and Ω are the laser frequency and phonon frequency, respectively. The ratio of Stokes to anti-Stokes side signal is:

$$R = \frac{C_S \chi_S^2}{C_{aS} \chi_{aS}^2} \frac{1 + n_p}{n_p} \frac{(\nu_{laser} - \Omega)^4}{(\nu_{laser} + \Omega)^4} \tag{7.12}$$

In quasi-equilibrium, the phonon population can be calculated according the statistics, i.e.,

$$n_p = \frac{1}{\exp^{-\frac{h\Omega}{k_B T}}} \tag{7.13}$$

From formula 7.12 and 7.13, temperature of phonons can be calculated. In order to determine the prefactor $\frac{C_S\chi_S^2}{C_{aS}\chi_{aS}^2}$ in 7.12, we further make the assumption that, before time zero, temperature is close to the room temperature (300 K), and the ratios of χ_S to χ_{aS}, C_S to C_{aS} are not changing during all the delay times of the experiments.

7.5.2 Phonon Population and Raman Tensor Changes vs Carrier Population

Without loss of generality, we write down the electronic susceptibility tensor χ_{ij} of a two- energy level system as:

$$\chi_{ij} \propto N(\rho_{00}-\rho_{11})(\frac{<\psi_0|r_i|\psi_1><\psi_1|r_j|\psi_0>}{\omega_{01}-\omega-i\Gamma}+\frac{<\psi_0|r_j|\psi_1><\psi_1|r_i|\psi_0>}{\omega_{01}+\omega+i\Gamma}) \quad (7.14)$$

where N represents two-level density of the system, and ρ_{00} and ρ_{11} are the diagonal density matrix elements referring to the ground state ψ_0 and excited state ψ_1, ω is the laser excitation frequency, and Γ is the damping constant. The Raman susceptibility tensor associated with a general vibration model Q can be written as:

$$\frac{\partial\chi_{ij}}{\partial Q}|_{Q_0} \propto N(\rho_{00}-\rho_{11})\frac{\partial}{\partial Q}(\frac{<\psi_0|r_i|\psi_1><\psi_1|r_j|\psi_0>}{\omega_{01}-\omega-i\Gamma}+\frac{<\psi_0|r_j|\psi_1><\psi_1|r_i|\psi_0>}{\omega_{01}+\omega+i\Gamma})|_{Q_0} \quad (7.15)$$

Thus, Raman tensor is proportional to the population difference $N(\rho_{00}-\rho_{11})$, i.e.

$$\frac{\partial\chi_{ij}}{\partial Q}|_{Q_0} \propto N(\rho_{00}-\rho_{11}), \quad (7.16)$$

where $\rho_{00}+\rho_{11}=1$ and it becomes

$$|\frac{\partial\chi_{ij}}{\partial Q}|_{Q_0}^2 \propto N(1-4\rho_{11}-4\rho_{11}^2). \quad (7.17)$$

Since $\rho_{11} \ll$, ρ_{11}^2 can be neglected such that

$$|\frac{\partial\chi_{ij}}{\partial Q}|_{Q_0}^2 \propto N(1-4\rho_{11}). \quad (7.18)$$

Finally,

$$\Delta|\frac{\partial\chi_{ij}}{\partial Q}|^2_{Q_0} \propto -4N\rho_{11}. \tag{7.19}$$

I.e., the reduction of the squared Raman susceptibility tensor $|\frac{\partial\chi_{ij}}{\partial Q}|^2_{Q_0}$ is linearly proportional to 4 times the excited state population $N\rho_{11}$. The pump induced phonon signal changes are due to both changes in the phonon population as well as changes in the Raman susceptibility. Ignoring changes in the prefactors, the observed Raman signals on the Stokes side can be expressed as:

$$I^S_{un-pumped} = |\chi^S_R|^2(1+n_p) \tag{7.20}$$

After optical excitation, the time dependent change of $|\chi_R|^2$ and n_p is $|\chi_R|^2(t)$ and $\delta n_p(t)$ respectively, thus Raman signal after optical excitation is:

$$I^S_{pumped} = [|\chi^S_R|^2 + \delta|\chi^S_R|^2(t)][1+n_p+\delta n_p(t)] \tag{7.21}$$

such that the pump induced difference signal is

$$\Delta I^S(t) = I^S_{pumped} - I^S_{un-pumped} \tag{7.22}$$

$$= [|\chi^S_R|^2 + \Delta|\chi^S_R|^2(t)]\Delta n_p(t) + (1+n_p)\Delta|\chi^S_R|^2 \tag{7.23}$$

Since $\Delta n_p(t) \ll 1$ and $n_p \ll 1$, the formula reduces to

$$\Delta I^S(t) = \Delta|\chi^S_R|^2(t) \tag{7.24}$$

Combined with 7.19 the Stokes side Raman signal change is

$$\Delta I^S(t) =\propto -4N\rho_{11} \tag{7.25}$$

which indicates that, on the Stokes side, the difference signal observed is linearly related to the electron (hole) density induced by optical pump. Therefore, to a good approximation, the observed dynamics of Raman signals on the Stokes side reflect the

electronic relaxation dynamics.

Similarly, on anti-Stokes side, the change of the intensity can be expressed as,

$$\Delta I^{aS}(t) = |\chi_R^{aS}|^2 \Delta n_p(t) + n_p \Delta |chi_R^{aS}|^2(t) + \Delta n_p(t) \Delta |\chi_R^{aS}|^2(t) \tag{7.26}$$

Since at temperatures $T \leq \hbar\Omega/k_B$ one has $n_p \ll 1$ this can very well be approximated as thus the last two terms on the right side above can be ignored, and reduces to

$$\Delta I^{aS}(t) = |\chi_R^{aS}|^2 \Delta n_p(t) \tag{7.27}$$

Therefore, to a good approximation, the observed dynamics of Raman signals on the anti- Stokes side reflect the vibrational relaxation dynamics.

Bibliography

[1] "https://www.weltderphysik.de/thema/symmetrien/kontinuierliche-symmetrien-und-das-noether-theorem/, Accessed: 2022-07-10." 2

[2] G. Perelman, "Finite extinction time for the solutions to the ricci flow on certain three-manifolds," 2003. 2

[3] E. Derunova, J. Gayles, Y. Sun, M. W. Gaultois, and M. N. Ali, "Fermi surface geometry," 2020. 2

[4] W. Witczak-Krempa, G. Chen, Y. B. Kim, and L. Balents, "Correlated quantum phenomena in the strong spin-orbit regime," *Annual Review of Condensed Matter Physics*, vol. 5, no. 1, pp. 57–82, 2014. 2, 3, 4

[5] B. Keimer and J. E. Moore, "The physics of quantum materials," *Nature Physics*, vol. 13, no. 11, pp. 1045–1055, 2017. 3

[6] M. Imada, A. Fujimori, and Y. Tokura, "Metal-insulator transitions," *Rev. Mod. Phys.*, vol. 70, pp. 1039–1263, Oct 1998. 4, 25

[7] D. Wulferding, Y. Choi, W. Lee, and K.-Y. Choi, "Raman spectroscopic diagnostic of quantum spin liquids," *Journal of Physics: Condensed Matter*, vol. 32, p. 043001, oct 2019. 4

[8] L. Balents, "Spin liquids in frustrated magnets," *Nature*, vol. 464, no. 7286, pp. 199–208, 2010. 4

[9] X. Wan, A. M. Turner, A. Vishwanath, and S. Y. Savrasov, "Topological semimetal and fermi-arc surface states in the electronic structure of pyrochlore iridates," *Phys. Rev. B*, vol. 83, p. 205101, May 2011. 4

[10] A. A. Burkov and L. Balents, "Weyl semimetal in a topological insulator multilayer," *Phys. Rev. Lett.*, vol. 107, p. 127205, Sep 2011. 4

[11] A. Go, W. Witczak-Krempa, G. S. Jeon, K. Park, and Y. B. Kim, "Correlation effects on 3d topological phases: From bulk to boundary," *Phys. Rev. Lett.*, vol. 109, p. 066401, Aug 2012. 4

[12] L. Norris, C. Rahmell, and Y. Mattley, "Raman spectroscopy as a quantitative tool for industry," *Special Issues*, vol. 27, May 2012. 4

[13] R. R. Jones, D. C. Hooper, L. Zhang, D. Wolverson, and V. K. Valev, "Raman techniques: Fundamentals and frontiers," *Nanoscale Research Letters*, vol. 14, no. 1, p. 231, 2019. 4, 5, 6

[14] L. Malard, M. Pimenta, G. Dresselhaus, and M. Dresselhaus, "Raman spectroscopy in graphene," *Physics Reports*, vol. 473, no. 5, pp. 51–87, 2009. 5

[15] R. Yan, J. R. Simpson, S. Bertolazzi, J. Brivio, M. Watson, X. Wu, A. Kis, T. Luo, A. R. Hight Walker, and H. G. Xing, "Thermal conductivity of monolayer molybdenum disulfide obtained from temperature-dependent raman spectroscopy," *ACS Nano*, vol. 8, pp. 986–993, 01 2014. 5

[16] R. Loudon, "The raman effect in crystals," *Advances in Physics*, vol. 13, no. 52, pp. 423–482, 1964. 5, 7, 12, 103

[17] W. Hayes, R. Loudon, and J. W. . Sons, *Scattering of Light by Crystals*. A Wiley-Interscience publication, Wiley, 1978. 5, 9, 11, 12, 13, 18

[18] D. A. Long and D. Long, *The Raman effect: a unified treatment of the theory of Raman scattering by molecules*, vol. 8. Wiley Chichester, 2002. 5, 10, 11, 12

[19] A. C. Ferrari, J. C. Meyer, V. Scardaci, C. Casiraghi, M. Lazzeri, F. Mauri, S. Piscanec, D. Jiang, K. S. Novoselov, S. Roth, and A. K. Geim, "Raman spectrum of graphene and graphene layers," *Phys. Rev. Lett.*, vol. 97, p. 187401, Oct 2006. 5

[20] M. Lazzeri and F. Mauri, "Nonadiabatic kohn anomaly in a doped graphene monolayer," *Phys. Rev. Lett.*, vol. 97, p. 266407, Dec 2006. 5

[21] M. Kalbac, A. Reina-Cecco, H. Farhat, J. Kong, L. Kavan, and M. S. Dresselhaus, "The influence of strong electron and hole doping on the raman intensity of chemical vapor-deposition graphene," *ACS Nano*, vol. 4, pp. 6055–6063, 10 2010. 5

[22] C.-F. Chen, C.-H. Park, B. W. Boudouris, J. Horng, B. Geng, C. Girit, A. Zettl, M. F. Crommie, R. A. Segalman, S. G. Louie, and F. Wang, "Controlling inelastic light scattering quantum pathways in graphene," *Nature*, vol. 471, no. 7340, pp. 617–620, 2011. 5

[23] C. Casiraghi, "Raman fingerprint of charged impurities in graphene," *Appl. Phys. Lett.*, vol. 91, 2007. 5

[24] W. J. Zhao, P. H. Tan, J. Liu, and A. C. Ferrari, "Intercalation of few-layer graphite flakes with fecl3: Raman determination of fermi level, layer by layer decoupling, and stability," *J. Am. Chem. Soc.*, vol. 133, 2011. 5

[25] A. Das, "Phonon renormalisation in doped bilayer graphene," *Phys. Rev. B*, vol. 79, 2009. 5

[26] J. Yan, "Electric field effect tuning of electron-phonon coupling in graphene," *Phys. Rev. Lett.*, vol. 98, 2007. 5

[27] D. M. Basko, "Boundary problems for dirac electrons and edge-assisted raman scattering in graphene," *Phys. Rev. B*, vol. 79, 2009. 5

[28] A. K. Gupta, T. J. Russin, H. R. Gutiérrez, and P. C. Eklund, "Probing graphene edges via raman scattering," *ACS Nano*, vol. 3, 2009. 5

[29] M. A. Pimenta, G. Dresselhaus, M. S. Dresselhaus, L. G. Cançado, A. Jorio, and R. Saito, "Studying disorder in graphite-based systems by raman spectroscopy," *Phys. Chem. Chem. Phys.*, vol. 9, pp. 1276–1290, 2007. 5

[30] S. Ryu, J. Maultzsch, M. Y. Han, P. Kim, and L. E. Brus, "Raman spectroscopy of lithographically patterned graphene nanoribbons," *ACS Nano*, vol. 5, 2011. 5

[31] P. Venezuela, M. Lazzeri, and F. Mauri, "Theory of double-resonant raman spectra in graphene: Intensity and line shape of defect-induced and two-phonon bands," *Phys. Rev. B*, vol. 84, 2011. 5

[32] A. A. Balandin, S. Ghosh, W. Bao, I. Calizo, D. Teweldebrhan, F. Miao, and C. N. Lau, "Superior thermal conductivity of single-layer graphene," *Nano Letters*, vol. 8, pp. 902–907, 03 2008. 5

[33] N. Bonini, N. Lazzeri, N. Marzari, and F. Mauri, "Phonon anharmonicities in graphite and graphene," *Phys. Rev. Lett.*, vol. 99, 2007. 5

[34] D. A. Chenet, O. B. Aslan, P. Y. Huang, C. Fan, A. M. van der Zande, T. F. Heinz, and J. C. Hone, "In-plane anisotropy in mono- and few-layer res2 probed by raman spectroscopy and scanning transmission electron microscopy," *Nano Letters*, vol. 15, pp. 5667–5672, 09 2015. 5

[35] M. Mohr, J. Maultzsch, and C. Thomsen, "Splitting of the raman 2d band of graphene subjected to strain," *Phys. Rev. B*, vol. 82, p. 201409, Nov 2010. 5

[36] D. Yoon, Y. W. Son, and H. Cheong, "Strain-dependent splitting of double resonance raman scattering band in graphene," *Phys. Rev. Lett.*, vol. 106, 2011. 5

[37] M. Huang, "Phonon softening and crystallographic orientation of strained graphene studied by raman spectroscopy," *Proc. Natl Acad. Sci. USA*, vol. 106, 2009. 5

[38] C. Rice, R. J. Young, R. Zan, U. Bangert, D. Wolverson, T. Georgiou, R. Jalil, and K. S. Novoselov, "Raman-scattering measurements and first-principles calculations of strain-induced phonon shifts in monolayer mos_2," *Phys. Rev. B*, vol. 87, p. 081307, Feb 2013. 5

[39] U. P. Agarwal, R. S. Reiner, and S. A. Ralph, "Cellulose i crystallinity determination using ft–raman spectroscopy: univariate and multivariate methods," *Cellulose*, vol. 17, no. 4, pp. 721–733, 2010. 5

[40] T. Gokus, "Making graphene luminescent by oxygen plasma treatment," *ACS Nano*, vol. 3, 2009. 5

[41] D. C. Elias, "Control of graphene's properties by reversible hydrogenation: Evidence for graphane," *Science*, vol. 323, 2009. 5

[42] R. R. Nair, "Fluorographene: mechanically strong and thermally stable two-dimensional wide-gap semiconductor," *Small*, vol. 6, 2010. 5

[43] J. H. Chen, W. G. Cullen, C. Jang, M. S. Fuhrer, and E. D. Williams, "Defect scattering in graphene," *Phys. Rev. Lett.*, vol. 102, 2008. 5

[44] D. M. Basko, "Calculation of the RamanGpeak intensity in monolayer graphene: role of ward identities," *New Journal of Physics*, vol. 11, p. 095011, sep 2009. 5

[45] A. Grüneis, "Phonon surface mapping of graphite: Disentangling quasi-degenerate phonon dispersions," *Phys. Rev. B*, vol. 80, 2009. 5

[46] P. May, "Signature of the two-dimensional phonon dispersion in graphene probed by double-resonant raman scattering," *Phys. Rev. B*, vol. 87, 2013. 5

[47] D. M. Basko, S. Piscanec, and A. C. Ferrari, "Electron-electron interactions and doping dependence of the two-phonon raman intensity in graphene," *Phys. Rev. B*, vol. 80, 2009. 5

[48] D. M. Basko, "Theory of resonant multiphonon raman scattering in graphene," *Phys. Rev. B*, vol. 78, 2008. 5

[49] C. Faugeras, M. Amado, P. Kossacki, M. Orlita, M. Sprinkle, C. Berger, W. A. de Heer, and M. Potemski, "Tuning the electron-phonon coupling in multilayer graphene with magnetic fields," *Phys. Rev. Lett.*, vol. 103, p. 186803, Oct 2009. 5

[50] P. Kossacki, "Electronic excitations and electron-phonon coupling in bulk graphite through raman scattering in high magnetic fields," *Phys. Rev. B*, vol. 84, 2011. 5

[51] C. Faugeras, "Magneto-raman scattering of graphene on graphite: Electronic excitations and their coupling to optical phonons," *Phys. Rev. Lett.*, vol. 107, 2011. 5

[52] Y. Kim, J. M. Poumirol, A. Lombardo, N. G. Kalugin, T. Georgiou, Y. J. Kim, K. S. Novoselov, A. C. Ferrari, J. Kono, O. Kashuba, V. I. Fal'ko, and D. Smirnov, "Measurement of filling-factor-dependent magnetophonon resonances in graphene using raman spectroscopy," *Phys. Rev. Lett.*, vol. 110, p. 227402, May 2013. 5

[53] J. Yan, "Observation of magneto-phonon resonance of dirac fermions in graphite," *Phys. Rev. Lett.*, vol. 105, 2010. 5

[54] T. Ando, "Magnetic oscillation of optical phonon in graphene," *J. Phys. Soc. Jpn*, vol. 76, 2007. 5

[55] C. H. Lui, "Imaging stacking order in few-layer graphene," *Nano Lett.*, vol. 11, 2011. 5

[56] C. Lui, "Observation of layer-breathing mode vibrations in few-layer graphene through combination raman scattering," *Nano Lett.*, vol. 12, 2012. 5

[57] F. Herziger, F. May, and J. Maultzsch, "Layer number determination in graphene using out-of-plane vibrations," *Phys. Rev. B*, vol. 85, 2012. 5

[58] D. Cialla, A. März, R. Böhme, F. Theil, K. Weber, M. Schmitt, and J. Popp, "Surface-enhanced raman spectroscopy (sers): progress and trends," *Analytical and Bioanalytical Chemistry*, vol. 403, no. 1, pp. 27–54, 2012. 5

[59] M. D. Sonntag, J. M. Klingsporn, L. K. Garibay, J. M. Roberts, J. A. Dieringer, T. Seideman, K. A. Scheidt, L. Jensen, G. C. Schatz, and R. P. Van Duyne, "Single-molecule tip-enhanced raman spectroscopy," *The Journal of Physical Chemistry C*, vol. 116, pp. 478–483, 01 2012. 5

[60] R. Zhang, Y. Zhang, Z. C. Dong, S. Jiang, C. Zhang, L. G. Chen, L. Zhang, Y. Liao, J. Aizpurua, Y. Luo, J. L. Yang, and J. G. Hou, "Chemical mapping of a single molecule by plasmon-enhanced raman scattering," *Nature*, vol. 498, no. 7452, pp. 82–86, 2013. 5, 6

[61] S. Reichardt and L. Wirtz, "Theory of resonant raman scattering: Towards a comprehensive ab initio description," *Phys. Rev. B*, vol. 99, p. 174312, May 2019. 5

[62] A. C. Ferrari and D. M. Basko, "Raman spectroscopy as a versatile tool for studying the properties of graphene," *Nature Nanotechnology*, vol. 8, p. 235, 2013. 5

[63] T. M. G. Mohiuddin, A. Lombardo, R. R. Nair, A. Bonetti, G. Savini, R. Jalil, N. Bonini, D. M. Basko, C. Galiotis, N. Marzari, K. S. Novoselov, A. K. Geim, and A. C. Ferrari, "Uniaxial strain in graphene by raman spectroscopy: g peak splitting, grüneisen parameters, and sample orientation," *Phys. Rev. B*, vol. 79, p. 205433, May 2009. 5

[64] M. Huang, H. Yan, T. F. Heinz, and J. Hone, "Probing strain-induced electronic structure change in graphene by raman spectroscopy," *Nano Letters*, vol. 10, pp. 4074–4079, 10 2010. 5

[65] J. E. Lee, G. Ahn, J. Shim, Y. S. Lee, and S. Ryu, "Optical separation of mechanical strain from charge doping in graphene," *Nature Communications*, vol. 3, no. 1, p. 1024, 2012. 5

[66] J. C. Chacón-Torres, L. Wirtz, and T. Pichler, "Manifestation of charged and strained graphene layers in the raman response of graphite intercalation compounds," *ACS Nano*, vol. 7, pp. 9249–9259, 10 2013. 5

[67] A. C. Ferrari, "Raman spectroscopy of graphene and graphite: Disorder, electron–phonon coupling, doping and nonadiabatic effects," *Solid State Communications*, vol. 143, no. 1, pp. 47 – 57, 2007. Exploring graphene. 5

[68] S. Pisana, M. Lazzeri, C. Casiraghi, K. S. Novoselov, A. K. Geim, A. C. Ferrari, and F. Mauri, "Breakdown of the adiabatic born–oppenheimer approximation in graphene," *Nature Materials*, vol. 6, no. 3, pp. 198–201, 2007. 5

[69] H. P. C. Miranda, S. Reichardt, G. Froehlicher, A. Molina-Sánchez, S. Berciaud, and L. Wirtz, "Quantum interference effects in resonant raman spectroscopy of single- and triple-layer mote2 from first-principles," *Nano Letters*, vol. 17, pp. 2381–2388, 04 2017. 5

[70] S. Goler, J. Yan, V. Pellegrini, and A. Pinczuk, "Raman spectroscopy of magneto-phonon resonances in graphene and graphite," *Solid State Communications*, vol. 152, no. 15, pp. 1289–1293, 2012. 5

[71] C. Neumann, D. Halpaap, S. Reichardt, L. Banszerus, M. Schmitz, K. Watanabe, T. Taniguchi, B. Beschoten, and C. Stampfer, "Probing electronic lifetimes and phonon anharmonicities in high-quality chemical vapor deposited graphene by magneto-raman spectroscopy," *Applied Physics Letters*, vol. 107, no. 23, p. 233105, 2015. 5

[72] J. Sonntag, S. Reichardt, L. Wirtz, B. Beschoten, M. I. Katsnelson, F. Libisch, and C. Stampfer, "Impact of many-body effects on landau levels in graphene," *Phys. Rev. Lett.*, vol. 120, p. 187701, May 2018. 5

[73] F. Benz, R. Chikkaraddy, A. Salmon, H. Ohadi, B. de Nijs, J. Mertens, C. Carnegie, R. W. Bowman, and J. J. Baumberg, "Sers of individual nanoparticles on a mirror: Size does matter, but so does shape," *The Journal of Physical Chemistry Letters*, vol. 7, pp. 2264–2269, 06 2016. 5

[74] P. Verma, "Tip-enhanced raman spectroscopy: Technique and recent advances," *Chemical Reviews*, vol. 117, pp. 6447–6466, 05 2017. 5

[75] P. P. Patra, R. Chikkaraddy, R. P. N. Tripathi, A. Dasgupta, and G. V. P. Kumar, "Plasmofluidic single-molecule surface-enhanced raman scattering from dynamic assembly of plasmonic nanoparticles," *Nature Communications*, vol. 5, no. 1, p. 4357, 2014. 5

[76] E. Bailo and V. Deckert, "Tip-enhanced raman scattering," *Chem. Soc. Rev.*, vol. 37, pp. 921–930, 2008. 5

[77] R. M. Stöckle, Y. D. Suh, V. Deckert, and R. Zenobi, "Nanoscale chemical analysis by tip-enhanced raman spectroscopy," *Chemical Physics Letters*, vol. 318, no. 1, pp. 131 – 136, 2000. 5

[78] M. S. Anderson, "Locally enhanced raman spectroscopy with an atomic force microscope," *Applied Physics Letters*, vol. 76, pp. 3130–3132, 2020/07/15 2000. 5

[79] K. L. Kelly, E. Coronado, L. L. Zhao, and G. C. Schatz, "The optical properties of metal nanoparticles: The influence of size, shape, and dielectric environment," *The Journal of Physical Chemistry B*, vol. 107, pp. 668–677, 01 2003. 5

[80] P. Verma, T. aki Yano, Y. Inouye, and S. Kawata, "Tip-enhanced near-field Raman scattering and imaging of carbon nanostructures," in *Plasmonics: Nanoimaging, Nanofabrication, and their Applications II* (S. Kawata, V. M. Shalaev, and D. P. Tsai, eds.), vol. 6324, pp. 96 – 104, International Society for Optics and Photonics, SPIE, 2006. 5

[81] N. Anderson, A. Hartschuh, S. Cronin, and L. Novotny, "Nanoscale vibrational analysis of single-walled carbon nanotubes," *Journal of the American Chemical Society*, vol. 127, pp. 2533–2537, 03 2005. 5

[82] S. Najjar, D. Talaga, L. Schué, Y. Coffinier, S. Szunerits, R. Boukherroub, L. Servant, V. Rodriguez, and S. Bonhommeau, "Tip-enhanced raman spectroscopy of combed double-stranded dna bundles," *The Journal of Physical Chemistry C*, vol. 118, pp. 1174–1181, 01 2014. 5

[83] E. Bailo and V. Deckert, "Tip-enhanced raman spectroscopy of single rna strands: Towards a novel direct-sequencing method," *Angewandte Chemie International Edition*, vol. 47, no. 9, pp. 1658–1661, 2008. 5

[84] D. Kurouski, M. Mattei, and R. P. Van Duyne, "Probing redox reactions at the nanoscale with electrochemical tip-enhanced raman spectroscopy," *Nano Letters*, vol. 15, pp. 7956–7962, 12 2015. 5

[85] C. S. Hamann and M. D. Sonntag, *Introduction to Raman Spectroscopy in the Undergraduate Curriculum*, ch. 1, pp. 1–11. 6

[86] J. T. Mendonça, B. Thidé, and H. Then, "Stimulated raman and brillouin backscattering of collimated beams carrying orbital angular momentum," *Phys. Rev. Lett.*, vol. 102, p. 185005, May 2009. 6

[87] M. Kasevich and S. Chu, "Atomic interferometry using stimulated raman transitions," *Phys. Rev. Lett.*, vol. 67, pp. 181–184, Jul 1991. 6

[88] J. Vieira, R. M. G. M. Trines, E. P. Alves, R. A. Fonseca, J. T. Mendonça, R. Bingham, P. Norreys, and L. O. Silva, "Amplification and generation of ultra-intense twisted laser pulses via stimulated raman scattering," *Nature Communications*, vol. 7, no. 1, p. 10371, 2016. 6

[89] L. Yin, B. J. Albright, K. J. Bowers, W. Daughton, and H. A. Rose, "Saturation of backward stimulated scattering of laser in kinetic regime: Wavefront bowing, trapped particle modulational instability, and trapped particle self-focusing of plasma waves," *Physics of Plasmas*, vol. 15, no. 1, p. 013109, 2008. 6

[90] H. J. Lee and J.-X. Cheng, "Imaging chemistry inside living cells by stimulated raman scattering microscopy," *Methods*, vol. 128, pp. 119–128, 2017. Imaging Cell Biology and Physiology In Vivo Using Intravital Microscopy. 6

[91] S. Coen, A. H. L. Chau, R. Leonhardt, J. D. Harvey, J. C. Knight, W. J. Wadsworth, and P. S. J. Russell, "Supercontinuum generation by stimulated raman scattering and parametric four-wave mixing in photonic crystal fibers," *J. Opt. Soc. Am. B*, vol. 19, pp. 753–764, Apr 2002. 6

[92] J.-X. Cheng and X. S. Xie, "Coherent anti-stokes raman scattering microscopy: Instrumentation, theory, and applications," *The Journal of Physical Chemistry B*, vol. 108, pp. 827–840, 01 2004. 6

[93] C. L. Evans, E. O. Potma, and X. S. Xie, "Coherent anti-stokes raman scattering spectral interferometry:determination of the real and imaginary components of nonlinear susceptibility $\chi(3)$ for vibrational microscopy," *Opt. Lett.*, vol. 29, pp. 2923–2925, Dec 2004. 6

[94] C. L. Evans and X. S. Xie, "Coherent anti-stokes raman scattering microscopy: Chemical imaging for biology and medicine," *Annual Review of Analytical Chemistry*, vol. 1, no. 1, pp. 883–909, 2008. PMID: 20636101. 6

[95] C. C. Moura, R. S. Tare, R. O. C. Oreffo, and S. Mahajan, "Raman spectroscopy and coherent anti-stokes raman scattering imaging: prospective tools for monitoring skeletal cells and skeletal regeneration," *Journal of The Royal Society Interface*, vol. 13, no. 118, p. 20160182, 2016. 6

[96] R. M. Goodhead, J. Moger, T. S. Galloway, and C. R. Tyler, "Tracing engineered nanomaterials in biological tissues using coherent anti-stokes raman scattering (cars) microscopy – a critical review," *Nanotoxicology*, vol. 9, no. 7, pp. 928–939, 2015. PMID: 25962086. 6

[97] M. Ji, D. A. Orringer, C. W. Freudiger, S. Ramkissoon, X. Liu, D. Lau, A. J. Golby, I. Norton, M. Hayashi, N. Y. R. Agar, G. S. Young, C. Spino, S. Santagata, S. Camelo-Piragua, K. L. Ligon, O. Sagher, and X. S. Xie, "Rapid, label-free detection of brain tumors with stimulated raman scattering microscopy," *Science Translational Medicine*, vol. 5, no. 201, pp. 201ra119–201ra119, 2013. 6

[98] M. Kuball and J. W. Pomeroy, "A review of raman thermography for electronic and opto-electronic device measurement with submicron spatial and nanosecond temporal resolution," *IEEE Transactions on Device and Materials Reliability*, vol. 16, no. 4, pp. 667–684, 2016. 6

[99] H. Kuzmany, *Solid-State Spectroscopy: An Introduction*. Springer Berlin Heidelberg, 2009. 7, 11, 12, 13, 15, 16, 17, 18

[100] A. Cantarero, "Raman scattering applied to materials science," *Procedia Materials Science*, vol. 9, pp. 113–122, 2015. International Congress of Science and Technology of Metallurgy and Materials, SAM – CONAMET 2014. 8

[101] R. Loudon, *The Quantum Theory of Light*. OUP Oxford, 2000. 12

[102] C. Ji-Xin and S. X. Xiaoliang, *Coherent Raman Scattering Microscopy*. Boca Raton: CRC Press, 1 ed., 2012. 12

[103] W. Demtröder, *Laserspektroskopie: Grundlagen und Techniken*. 01 2011. 13

[104] U. Fano, "Effects of configuration interaction on intensities and phase shifts," *Phys. Rev.*, vol. 124, pp. 1866–1878, Dec 1961. 16

[105] M. Testa-Anta, M. A. Ramos-Docampo, M. Comesaña-Hermo, B. Rivas-Murias, and V. Salgueiriño, "Raman spectroscopy to unravel the magnetic properties

of iron oxide nanocrystals for bio-related applications," *Nanoscale Adv.*, vol. 1, pp. 2086–2103, 2019. 16

[106] D. Tuschel, "Raman thermometry," vol. 31, 12 2016. 17

[107] J. J. Gallardo, J. Navas, D. Zorrilla, R. Alcántara, D. Valor, C. Fernández-Lorenzo, and J. Martín-Calleja, "Micro-raman spectroscopy for the determination of local temperature increases in tio2 thin films due to the effect of radiation," *Appl. Spectrosc.*, vol. 70, pp. 1128–1136, Jul 2016. 17

[108] M. G. Cottam and D. J. Lockwood, *Light scattering in magnetic solids*. Wiley New York, 1986. 18, 20

[109] P. A. Fleury and R. Loudon, "Scattering of light by one- and two-magnon excitations," *Phys. Rev.*, vol. 166, pp. 514–530, Feb 1968. 18, 19, 20

[110] R. Versteeg, *Optically probed order and dynamics in the chiral cluster magnet* Cu_2OSeO_3. PhD thesis, University of Cologne, 2019. 18, 20

[111] Y. Ando, "Topological insulator materials," *J. Phys. Soc. Japan*, vol. 82, no. 10, p. 102001, 2013. 22, 73

[112] C.-H. Yee and L. Balents, "Phase separation in doped mott insulators," *Phys. Rev. X*, vol. 5, p. 021007, Apr 2015. 25

[113] Y. Cao, P. Shafer, X. Liu, D. Meyers, M. Kareev, S. Middey, J. W. Freeland, E. Arenholz, and J. Chakhalian, "Magnetism and electronic structure of $YTiO_3$ thin films," *Applied Physics Letters*, vol. 107, no. 11, p. 112401, 2015. 25

[114] X. Yang and G. Wu, "Correlation corrected phonon vibration in YTiO and its effect on electronic properties," *EPL (Europhysics Letters)*, vol. 117, p. 27004, jan 2017. 25

[115] T. Katsufuji, Y. Okimoto, and Y. Tokura, "Spectral weight transfer of the optical conductivity in doped mott insulators," *Phys. Rev. Lett.*, vol. 75, pp. 3497–3500, Nov 1995. 25

[116] Y. Okimoto, T. Katsufuji, Y. Okada, T. Arima, and Y. Tokura, "Optical spectra in (La,Y)TiO_3: Variation of mott-hubbard gap features with change of electron correlation and band filling," *Phys. Rev. B*, vol. 51, pp. 9581–9588, Apr 1995. 25

[117] K. Morikawa, T. Mizokawa, A. Fujimori, Y. Taguchi, and Y. Tokura, "Photoemission spectral weight distribution in $Y_{1-x}Ca_xTiO_3$," *Phys. Rev. B*, vol. 54, pp. 8446–8451, Sep 1996. 25

[118] Y. Taguchi, Y. Tokura, T. Arima, and F. Inaba, "Change of electronic structures with carrier doping in the highly correlated electron system $Y_{1-x}Ca_xTiO_3$," *Phys. Rev. B*, vol. 48, pp. 511–518, Jul 1993. 26

[119] Y. Tokura, Y. Taguchi, Y. Moritomo, K. Kumagai, T. Suzuki, and Y. Iye, "Barely metallic states with enhanced carrier mass in $Y_{1-x}Ca_xTiO_3$," *Phys. Rev. B*, vol. 48, pp. 14063–14066, Nov 1993. 26

[120] F. Iga, T. Naka, T. Matsumoto, N. Shirakawa, K. Murata, and Y. Nishihara, "Study of first-order metal-insulator transition in the strongly correlated electron system $Y_{1-x}Ca_xTiO_3$," *Physica B: Condensed Matter*, vol. 223-224, pp. 526 – 528, 1996. Proceedings of the International Conference on Strongly Correlated Electron Systems. 26

[121] K. Kato, E. Nishibori, M. Takata, M. Sakata, T. Nakano, K. Uchihira, M. Tsubota, F. Iga, and T. Takabatake, "The metal–insulator transition in $Y_{1-x}Ca_xTiO_3$ caused by phase separation," *Journal of the Physical Society of Japan*, vol. 71, no. 9, pp. 2082–2085, 2002. 26, 35

[122] H. Nakao, M. Tsubota, F. Iga, K. Uchihira, T. Nakano, T. Takabatake, K. Kato, and Y. Murakami, "Orbitally ordered state in $Y_{1-x}Ca_xTiO_3$ ($0 < x \leq 0.5$)," *Journal of the Physical Society of Japan*, vol. 73, no. 10, pp. 2620–2623, 2004. 26

[123] M. Tsubota, F. Iga, T. Nakano, K. Uchihira, S. Kura, M. Takemura, Y. Bando, K. Umeo, T. Takabatake, E. Nishibori, M. Takata, M. Sakata, K. Kato, and Y. Ohishi, "Hole-doping and pressure effects on the metal–insulator transition in single crystals of $Y_{1-x}Ca_xTiO_3$ ($0.37 \leq x \leq 0.41$)," *Journal of the Physical Society of Japan*, vol. 72, no. 12, pp. 3182–3188, 2003. 26

[124] H. Matsuhata, F. Iga, M. Tsubota, T. Nakano, T. Takabatake, and K. Kato, "Phase separation in $Y_{1-x}Ca_xTiO_3$ associated with the insulator-to-metal transition: Observation by transmission electron microscopy," *Phys. Rev. B*, vol. 70, p. 134109, Oct 2004. 26, 29, 34

[125] A. Komarek, *Complex ordering phenomena in transition metal oxides and oxyhalides*. dissertation, University of Cologne, 2009. 26, 27, 34, 35

[126] M. Tsubota, F. Iga, K. Uchihira, T. Nakano, S. Kura, T. Takabatake, S. Kodama, H. Nakao, and Y. Murakami, "Coupling between orbital and lattice degrees of freedom in $Y_{1-x}Ca_xTiO_3$ ($0 < x \leq 0.75$): A resonant x-ray scattering study," *Journal of the Physical Society of Japan*, vol. 74, no. 12, pp. 3259–3266, 2005. 27

[127] F. Barbo, M. Bertolo, A. Bianco, G. Cautero, S. Fontana, T. K. Johal, S. La Rosa, G. Margaritondo, and K. Kaznacheyev, "Spectromicroscopy beamline at elettra: Performances achieved at the end of commissioning," *Review of Scientific Instruments*, vol. 71, no. 1, pp. 5–10, 2000. 27

[128] M. N. Iliev, M. V. Abrashev, H.-G. Lee, V. N. Popov, Y. Y. Sun, C. Thomsen, R. L. Meng, and C. W. Chu, "Raman spectroscopy of orthorhombic perovskitelike $YMnO_3$ and $LaMnO_3$," *Phys. Rev. B*, vol. 57, pp. 2872–2877, Feb 1998. 31, 32, 145

[129] T. Tsurui, N. Ogita, M. Udagawa, M. Tsubota, and F. Iga, "Raman scattering investigation of $Y_{1-x}Ca_xTiO_3$," *Phys. Rev. B*, vol. 69, p. 024102, Jan 2004. 31, 32, 35, 145

[130] T. Katsufuji and Y. Tokura, "Anomalous variation of phonon raman intensities near the metal-to-mott-insulator transition in titanium oxide systems," *Phys. Rev. B*, vol. 50, pp. 2704–2707, Jul 1994. 32

[131] S. Nakatsuji, S.-i. Ikeda, and Y. Maeno, "Ca 2ruo 4: New mott insulators of layered ruthenate," *Journal of the Physical Society of Japan*, vol. 66, no. 7, pp. 1868–1871, 1997. 37

[132] S. Nakatsuji, T. Ando, Z. Mao, and Y. Maeno, "Metal insulator transition in ca2-xsrxruo4," *Physica B: Condensed Matter*, vol. 259-261, pp. 949–950, 1999. Funding Information: The authors acknowledge T. Ishiguro and K. Yamada for useful discussions and kind support. They are grateful to S. Ikeda for helpful discussion. This work was supported by a Grant-in-Aid for Scientific Research on Priority Areas "Anomalous Metallic State near the Mott Transition" from the Ministry of Education, Science, Sports and Culture. 37, 38

[133] S. Nakatsuji and Y. Maeno, "Switching of magnetic coupling by a structural symmetry change near the mott transition in $ca_{2-x}sr_xruo_4$," *Phys. Rev. B*, vol. 62, pp. 6458–6466, Sep 2000. 37

[134] Y. Maeno, H. Hashimoto, K. Yoshida, S. Nishizaki, T. Fujita, J. G. Bednorz, and F. Lichtenberg, "Superconductivity in a layered perovskite without copper," *Nature*, vol. 372, no. 6506, pp. 532–534, 1994. 37

[135] M. Braden, G. André, S. Nakatsuji, and Y. Maeno, "Crystal and magnetic structure of ca_2ruo_4 : magnetoelastic coupling and the metal-insulator transition," *Phys. Rev. B*, vol. 58, pp. 847–861, Jul 1998. 37, 38, 42, 43, 57, 59, 65

[136] O. Friedt, M. Braden, G. André, P. Adelmann, S. Nakatsuji, and Y. Maeno, "Structural and magnetic aspects of the metal-insulator transition in $ca_{2-x}sr_xruo_4$," *Phys. Rev. B*, vol. 63, p. 174432, Apr 2001. 37, 38, 40, 41, 42, 43, 57, 59, 65, 140

[137] Z. Fang and K. Terakura, "Magnetic phase diagram of $ca_{2-x}sr_xruo_4$ governed by structural distortions," *Phys. Rev. B*, vol. 64, p. 020509, Jun 2001. 37

[138] E. Gorelov, M. Karolak, T. O. Wehling, F. Lechermann, A. I. Lichtenstein, and E. Pavarini, "Nature of the mott transition in ca_2ruo_4," *Phys. Rev. Lett.*, vol. 104, p. 226401, Jun 2010. 37, 57, 69

[139] G. Zhang and E. Pavarini, "Mott transition, spin-orbit effects, and magnetism in ca_2ruo_4," *Phys. Rev. B*, vol. 95, p. 075145, Feb 2017. 37, 38, 58

[140] G. Zhang and E. Pavarini, "Higgs mode and stability of xy-orbital ordering in ca_2ruo_4," *Phys. Rev. B*, vol. 101, p. 205128, May 2020. 37, 38

[141] J. H. Jung, Z. Fang, J. P. He, Y. Kaneko, Y. Okimoto, and Y. Tokura, "Change of electronic structure in ca_2ruo_4 induced by orbital ordering," *Phys. Rev. Lett.*, vol. 91, p. 056403, Jul 2003. 37

[142] T. Hotta and E. Dagotto, "Prediction of orbital ordering in single-layered ruthenates," *Phys. Rev. Lett.*, vol. 88, p. 017201, Dec 2001. 37

[143] A. Liebsch and H. Ishida, "Subband filling and mott transition in $ca_{2-x}sr_xruo_4$," *Phys. Rev. Lett.*, vol. 98, p. 216403, May 2007. 37

[144] Liebsch, A., "Absence of orbital-dependent mott transition in $ca_{2-x}sr_xruo_4$," *Europhys. Lett.*, vol. 63, no. 1, pp. 97–103, 2003. 37

[145] V. Anisimov, I. Nekrasov, D. Kondakov, T. Rice, and M. Sigrist, "Orbital-selective mott-insulator transition in $ca_{2-x}sr_xruo_4$," *The European Physical Journal B - Condensed Matter and Complex Systems*, vol. 25, pp. 191–201, Jan 2002. 37

[146] G. Khaliullin, "Excitonic magnetism in van vleck–type d^4 mott insulators," *Phys. Rev. Lett.*, vol. 111, p. 197201, Nov 2013. 38, 58

[147] S. Kunkemöller, D. Khomskii, P. Steffens, A. Piovano, A. A. Nugroho, and M. Braden, "Highly anisotropic magnon dispersion in ca_2ruo_4: Evidence for strong spin orbit coupling," *Phys. Rev. Lett.*, vol. 115, p. 247201, Dec 2015. 38, 46, 47

[148] A. Akbari and G. Khaliullin, "Magnetic excitations in a spin-orbit-coupled d^4 mott insulator on the square lattice," *Phys. Rev. B*, vol. 90, p. 035137, Jul 2014. 38, 58

[149] S. Kunkemöller, E. Komleva, S. V. Streltsov, S. Hoffmann, D. I. Khomskii, P. Steffens, Y. Sidis, K. Schmalzl, and M. Braden, "Magnon dispersion in $ca_2ru_{1-x}ti_xo_4$: Impact of spin-orbit coupling and oxygen moments," *Phys. Rev. B*, vol. 95, p. 214408, Jun 2017. 38, 39, 41, 43, 46, 47

[150] D. Sutter, C. Fatuzzo, S. Moser, M. Kim, R. Fittipaldi, A. Vecchione, V. Granata, Y. Sassa, G. Cossalter, F. Gatti, M. Grioni, H. Ronnow, N. Plumb, C. Matt, M. Shi, M. Hoesch, T. Kim, T. Chang, H. Jeng, C. Jozwiak, A. Bostwick, E. Rotenberg, A. Georges, T. Neupert, and J. Chang, "Hallmarks of hunds coupling in the mott insulator ca_2ruo_4," *Nat Commun.*, vol. 5, May 2017. 38

[151] A. Jain, M. Krautloher, J. Porras, G. Ryu, D. Chen, D. Abernathy, J. Park, A. Ivanov, J. Chaloupka, G. Khaliullin, B. Keimer, and B. Kim, "Higgs mode and its decay in a two-dimensional antiferromagnet," *Nature Physics*, vol. 13, p. 633, Dec 2017. 38, 46, 47

[152] C. S. Alexander, G. Cao, V. Dobrosavljevic, S. McCall, J. E. Crow, E. Lochner, and R. P. Guertin, "Destruction of the mott insulating ground state of ca_2ruo_4 by a structural transition," *Phys. Rev. B*, vol. 60, pp. R8422–R8425, Sep 1999. 38, 57

[153] P. Steffens, O. Friedt, P. Alireza, W. G. Marshall, W. Schmidt, F. Nakamura, S. Nakatsuji, Y. Maeno, R. Lengsdorf, M. M. Abd-Elmeguid, and M. Braden,

"High-pressure diffraction studies on ca_2ruo_4," *Phys. Rev. B*, vol. 72, p. 094104, Sep 2005. 38, 40, 41, 50, 140

[154] G. Cao, S. McCall, V. Dobrosavljevic, C. S. Alexander, J. E. Crow, and R. P. Guertin, "Ground-state instability of the mott insulator ca_2ruo_4 : impact of slight la doping on the metal-insulator transition and magnetic ordering," *Phys. Rev. B*, vol. 61, pp. R5053–R5057, Feb 2000. 38

[155] S. Nakatsuji and Y. Maeno, "Switching of magnetic coupling by a structural symmetry change near the mott transition in $ca_{2-x}sr_xruo_4$," *Phys. Rev. B*, vol. 62, pp. 6458–6466, Sep 2000. 38

[156] F. Nakamura, T. Goko, M. Ito, T. Fujita, S. Nakatsuji, H. Fukazawa, Y. Maeno, P. Alireza, D. Forsythe, and S. R. Julian, "From mott insulator to ferromagnetic metal: A pressure study of ca_2ruo_4," *Phys. Rev. B*, vol. 65, p. 220402, May 2002. 38

[157] F. Nakamura, M. Sakaki, Y. Yamanaka, S. Tamaru, T. Suzuki, and Y. Maeno, "Electric-field-induced metal maintained by current of the mott insulator ca2ruo4," *Scientific Reports*, vol. 3, p. 2536, 2013. 38

[158] Y. Taguchi, T. Matsumoto, and Y. Tokura, "Dielectric breakdown of one-dimensional mott insulators sr_2cuo_3 and $srcuo_2$," *Phys. Rev. B*, vol. 62, pp. 7015–7018, Sep 2000. 38

[159] R. Okazaki, Y. Nishina, Y. Yasui, F. Nakamura, T. Suzuki, and I. Terasaki, "Current-induced gap suppression in the mott insulator ca2ruo4," *Journal of the Physical Society of Japan*, vol. 82, no. 10, p. 103702, 2013. 38, 68, 69

[160] J. Zhang, A. S. McLeod, Q. Han, X. Chen, H. A. Bechtel, Z. Yao, S. N. Gilbert Corder, T. Ciavatti, T. H. Tao, M. Aronson, G. L. Carr, M. C. Martin, C. Sow, S. Yonezawa, F. Nakamura, I. Terasaki, D. N. Basov, A. J. Millis, Y. Maeno, and M. Liu, "Nano-resolved current-induced insulator-metal transition in the mott insulator ca_2ruo_4," *Phys. Rev. X*, vol. 9, p. 011032, Feb 2019. 38, 39, 58

[161] J. Bertinshaw, N. Gurung, P. Jorba, H. Liu, M. Schmid, D. T. Mantadakis, M. Daghofer, M. Krautloher, A. Jain, G. H. Ryu, O. Fabelo, P. Hansmann, G. Khaliullin, C. Pfleiderer, B. Keimer, and B. J. Kim, "Unique crystal structure

of ca_2ruo_4 in the current stabilized semimetallic state," *Phys. Rev. Lett.*, vol. 123, p. 137204, Sep 2019. 38, 65, 68

[162] C. Cirillo, V. Granata, G. Avallone, R. Fittipaldi, C. Attanasio, A. Avella, and A. Vecchione, "Emergence of a metallic metastable phase induced by electrical current in ca_2ruo_4," *Phys. Rev. B*, vol. 100, p. 235142, Dec 2019. 38

[163] K. Fürsich, J. Bertinshaw, P. Butler, M. Krautloher, M. Minola, and B. Keimer, "Raman scattering from current-stabilized nonequilibrium phases in ca_2ruo_4," *Phys. Rev. B*, vol. 100, p. 081101, Aug 2019. 38, 58, 68

[164] C. Sow, S. Yonezawa, S. Kitamura, T. Oka, K. Kuroki, F. Nakamura, and Y. Maeno, "Current-induced strong diamagnetism in the mott insulator ca2ruo4," *Science*, vol. 358, no. 6366, pp. 1084–1087, 2017. 38, 67

[165] K. Jenni, F. Wirth, K. Dietrich, L. Berger, Y. Sidis, S. Kunkemöller, C. P. Grams, D. I. Khomskii, J. Hemberger, and M. Braden, "Evidence for current-induced phase coexistence in ca_2ruo_4 and its influence on magnetic order," *Phys. Rev. Materials*, vol. 4, p. 085001, Aug 2020. 38, 39, 42, 51, 68

[166] G. Mattoni, S. Yonezawa, F. Nakamura, and Y. Maeno, "Role of local temperature in the current-driven metal–insulator transition of ca_2ruo_4," *Phys. Rev. Materials*, vol. 4, p. 114414, Nov 2020. 38, 39

[167] H. Zhao, B. Hu, F. Ye, C. Hoffmann, I. Kimchi, and G. Cao, "Nonequilibrium orbital transitions via applied electrical current in calcium ruthenates," *Phys. Rev. B*, vol. 100, p. 241104, Dec 2019. 38, 39

[168] G. Mattoni, S. Yonezawa, and Y. Maeno, "Diamagnetic-like response from localized heating of a paramagnetic material," *Applied Physics Letters*, vol. 116, no. 17, p. 172405, 2020. 38

[169] A. G. Khachaturian, "Theory of structural transformations in solids," 39, 42

[170] S. Kaufmann, U. Rössler, O. Heczko, M. Wuttig, J. Buschbeck, L. Schultz, and S. Fähler, "Adaptive modulations of martensites.," *Phys Rev Lett.*, vol. 104, p. 145702, Apr 2010. 39

[171] H. Fukazawa, S. Nakatsuji, and Y. Maeno, "Intrinsic properties of the mott insulator ca2ruo4+ (=0) studied with single crystals," *Physica B: Condensed Matter*, vol. 281-282, pp. 613 – 614, 2000. 39

[172] S. Kunkemöller, F. Sauer, A. A. Nugroho, and M. Braden, "Magnetic anisotropy of large floating-zone-grown single-crystals of srruo3," *Crystal Research and Technology*, vol. 51, no. 4, pp. 299–305, 2016. 39

[173] T. Mizokawa, L. H. Tjeng, G. A. Sawatzky, G. Ghiringhelli, O. Tjernberg, N. B. Brookes, H. Fukazawa, S. Nakatsuji, and Y. Maeno, "Spin-orbit coupling in the mott insulator ca_2ruo_4," *Phys. Rev. Lett.*, vol. 87, p. 077202, Jul 2001. 41, 57

[174] A. G. Khachaturyan, S. M. Shapiro, and S. Semenovskaya, "Adaptive phase formation in martensitic transformation," *Phys. Rev. B*, vol. 43, pp. 10832–10843, May 1991. 42

[175] M. Braden, W. Reichardt, Y. Sidis, Z. Mao, and Y. Maeno, "Lattice dynamics and electron-phonon coupling in sr_2Ruo_4: Inelastic neutron scattering and shell-model calculations," *Phys. Rev. B*, vol. 76, p. 014505, Jul 2007. 42, 43

[176] Y. Wang, J. J. Wang, J. E. Saal, S. L. Shang, L.-Q. Chen, and Z.-K. Liu, "Phonon dispersion in sr_2ruo_4 studied by a first-principles cumulative force-constant approach," *Phys. Rev. B*, vol. 82, p. 172503, Nov 2010. 42, 43

[177] H. Rho, S. L. Cooper, S. Nakatsuji, H. Fukazawa, and Y. Maeno, "Lattice dynamics and the electron-phonon interaction in ca_2ruo_4," *Phys. Rev. B*, vol. 71, p. 245121, Jun 2005. 42, 45, 46, 47, 145

[178] G. Kresse and J. Furthmüller, "Efficient iterative schemes for ab initio total-energy calculations using a plane-wave basis set," *Phys. Rev. B*, vol. 54, pp. 11169–11186, Oct 1996. 43, 80

[179] J. P. Perdew, K. Burke, and M. Ernzerhof, "Generalized gradient approximation made simple," *Phys. Rev. Lett.*, vol. 77, pp. 3865–3868, Oct 1996. 43, 80

[180] S. V. Streltsov and D. I. Khomskii, "Unconventional magnetism as a consequence of the charge disproportionation and the molecular orbital formation in $ba_4ru_3o_{10}$," *Phys. Rev. B*, vol. 86, p. 064429, Aug 2012. 43

[181] S. Lee, J.-G. Park, D. T. Adroja, D. Khomskii, S. Streltsov, K. A. McEwen, H. Sakai, K. Yoshimura, V. I. Anisimov, D. Mori, R. Kanno, and R. Ibberson, "Spin gap in tl2ru2o7 and the possible formation of haldane chains in three-dimensional crystals," *Nature Materials*, vol. 5, no. 6, pp. 471–476, 2006. 43

[182] S.-M. Souliou, J. c. v. Chaloupka, G. Khaliullin, G. Ryu, A. Jain, B. J. Kim, M. Le Tacon, and B. Keimer, "Raman scattering from higgs mode oscillations in the two-dimensional antiferromagnet ca_2ruo_4," *Phys. Rev. Lett.*, vol. 119, p. 067201, Aug 2017. 46, 47, 67, 68

[183] J. Jung, "Raman scattering and optical absorption studies of an orbital ordered ca2ruo4," *Solid State Communications*, vol. 133, no. 2, pp. 103 – 107, 2005. 46

[184] Gruninger, "Experimental quest for orbital waves," *Nature*, vol. 418, p. 137204, Sep 2002. 46

[185] W. Witczak-Krempa, G. Chen, Y. B. Kim, and L. Balents, "Correlated quantum phenomena in the strong spin-orbit regime," *Annual Review of Condensed Matter Physics*, vol. 5, no. 1, pp. 57–82, 2014. 57

[186] I. Zegkinoglou, J. Strempfer, C. S. Nelson, J. P. Hill, J. Chakhalian, C. Bernhard, J. C. Lang, G. Srajer, H. Fukazawa, S. Nakatsuji, Y. Maeno, and B. Keimer, "Orbital ordering transition in ca_2ruo_4 observed with resonant x-ray diffraction," *Phys. Rev. Lett.*, vol. 95, p. 136401, Sep 2005. 57

[187] S. Kunkemöller, D. Khomskii, P. Steffens, A. Piovano, A. A. Nugroho, and M. Braden, "Highly anisotropic magnon dispersion in ca_2ruo_4: Evidence for strong spin orbit coupling," *Phys. Rev. Lett.*, vol. 115, p. 247201, Dec 2015. 57, 58

[188] H. Zhao, B. Hu, F. Ye, C. Hoffmann, I. Kimchi, and G. Cao, "Nonequilibrium orbital transitions via applied electrical current in calcium ruthenate," 2019. 58

[189] S. Kunkemöller, E. Komleva, S. V. Streltsov, S. Hoffmann, D. I. Khomskii, P. Steffens, Y. Sidis, K. Schmalzl, and M. Braden, "Magnon dispersion in $ca_2ru_{1-x}ti_xo_4$: Impact of spin-orbit coupling and oxygen moments," *Phys. Rev. B*, vol. 95, p. 214408, Jun 2017. 58, 59, 60, 61, 67

[190] C. J. BRADLEY and B. L. DAVIES, "Magnetic groups and their corepresentations," *Rev. Mod. Phys.*, vol. 40, pp. 359–379, Apr 1968. 60

[191] A. P. Cracknell, "Scattering matrices for the raman effect in magnetic crystals," *Journal of Physics C: Solid State Physics*, vol. 2, pp. 500–511, mar 1969. 60

[192] A. P. Cracknell, "Group theory and magnetic phenomena in solids," *Reports on Progress in Physics*, vol. 32, pp. 633–707, jul 1969. 60

[193] E. V. Komleva, V. Y. Irkhin, I. V. Solovyev, M. I. Katsnelson, and S. V. Streltsov, "Unconventional magnetism and electronic state in the frustrated layered system $pdcro_2$," *Phys. Rev. B*, vol. 102, p. 174438, Nov 2020. 64

[194] G. Kresse and J. Furthmüller, "Efficiency of ab-initio total energy calculations for metals and semiconductors using a plane-wave basis set," *Comput. Mater. Sci.*, vol. 6, no. 1, pp. 15 – 50, 1996. 64, 80

[195] R. Elmér, M. Berg, L. Carlén, B. Jakobsson, B. Norén, A. Oskarsson, G. Ericsson, J. Julien, T.-F. Thorsteinsen, M. Guttormsen, G. Løvhøiden, V. Bellini, E. Grosse, C. Müntz, P. Senger, and L. Westerberg, "k^+ emission in symmetric heavy ion reactions at subthreshold energies [phys. rev. lett. 77, 4884 (1996)]," *Phys. Rev. Lett.*, vol. 78, pp. 1396–1396, Feb 1997. 64

[196] J. Fuchs, P. W. Epperlein, M. Welte, and W. Eisenmenger, "Energy gap reduction in superconducting tin films by quasiparticle injection," *Phys. Rev. Lett.*, vol. 38, pp. 919–922, Apr 1977. 68

[197] J. H. Jung, Z. Fang, J. P. He, Y. Kaneko, Y. Okimoto, and Y. Tokura, "Change of electronic structure in ca_2ruo_4 induced by orbital ordering," *Phys. Rev. Lett.*, vol. 91, p. 056403, Jul 2003. 69

[198] M. Z. Hasan and C. L. Kane, "Colloquium: Topological insulators," *Rev. Mod. Phys.*, vol. 82, no. 4, pp. 3045–3067, 2010. 73

[199] H. Zhang, C.-X. Liu, X.-L. Qi, X. Dai, Z. Fang, and S.-C. Zhang, "Topological insulators in bi_2se_3, bi_2te_3 and sb_2te_3 with a single dirac cone on the surface," *Nature Phys.*, vol. 5, pp. 438–442, 05 2009. 74, 80

[200] Z. Ren, A. A. Taskin, S. Sasaki, K. Segawa, and Y. Ando, "Large bulk resistivity and surface quantum oscillations in the topological insulator Bi_2Te_2Se," *Phys. Rev. B*, vol. 82, p. 241306, Dec 2010. 74

[201] Z. Ren, A. A. Taskin, S. Sasaki, K. Segawa, and Y. Ando, "Optimizing Bi2-xSbxTe3-ySey solid solutions to approach the intrinsic topological insulator regime," *Phys. Rev. B*, vol. 84, no. 16, p. 165311, 2011. 74, 75, 80, 88

[202] A. A. Taskin and Y. Ando *Phys. Rev. B*, vol. 84, p. 035301, 2011. 74

[203] T. Arakane, T. Sato, S. Souma, K. Kosaka, K. Nakayama, M. Komatsu, T. Takahashi, Z. Ren, K. Segawa, and Y. Ando *Nature Commun.*, vol. 3, p. 636, 2012. 74

[204] K. Segawa, Z. Ren, S. Sasaki, T. Tsuda, S. Kuwabata, and Y. Ando, "Ambipolar transport in bulk crystals of a topological insulator by gating with ionic liquid," *Phys. Rev. B*, vol. 86, no. 7, p. 075306, 2012. 74

[205] B. I. Shklovskii and A. L. Efros, "Completely compensated crystalline semiconductor as a model of an amorphous semiconductor," *Sov. Phys. JETP*, vol. 35, p. 610, 1972. 74

[206] T. C. B. Skinner and B. Shklovskii, "Why is the bulk resistivity of topological insulators so small?," *Phys. Rev. Lett.*, vol. 109, p. 176801, 2012. 74

[207] Y. Xu, I. Miotkowski, C. Liu, J. Tian, H. Nam, N. Alidoust, J. Hu, C.-K. Shih, M. Z. Hasan, and Y. P. Chen, "Observation of topological surface state quantum hall effect in an intrinsic three-dimensional topological insulator," *Nature Phys.*, vol. 10, no. 12, pp. 956–963, 2014. 74

[208] F. Yang, S. Ghatak, A. A. Taskin, K. Segawa, Y. Ando, M. Shiraishi, Y. Kanai, K. Matsumoto, A. Rosch, and Y. Ando, "Switching of charge-current-induced spin polarization in the topological insulator bisbtese$_2$," *Phys. Rev. B*, vol. 94, no. 7, p. 075304, 2016. 74

[209] S. Ghatak, O. Breunig, F. Yang, Z. Wang, A. A. Taskin, and Y. Ando, "Anomalous fraunhofer patterns in gated josephson junctions based on the bulk-insulating topological insulator bisbtese$_2$," *Nano Lett.*, vol. 18, no. 8, pp. 5124–5131, 2018. 74

[210] L. A. Jauregui, M. Kayyalha, A. Kazakov, I. Miotkowski, L. P. Rokhinson, and Y. P. Chen, "Gate-tunable supercurrent and multiple andreev reflections in a superconductor-topological insulator nanoribbon-superconductor hybrid device," *Appl. Phys. Lett.*, vol. 112, no. 9, p. 093105, 2018. 74

[211] Y. Liu, J. Besbas, Y. Wang, P. He, M. Chen, D. Zhu, Y. Wu, J. M. Lee, L. Wang, J. Moon, N. Koirala, S. Oh, and H. Yang, "Direct visualization of current-induced spin accumulation in topological insulators," *Nature Commun.*, vol. 9, no. 1, p. 2492, 2018. 74

[212] I. Efthimiopoulos, J. Zhang, M. Kucway, C. Park, R. C. Ewing, and Y. Wang, "Sb2se3 under pressure," *Sci. Rep.*, vol. 3, p. 2665, 2013. 74

[213] W. Richter, H. Köhler, and C. R. Becker, "A Raman and Far-Infrared Investigation of Phonons in the Rhombohedra1 V2-V13 Compounds," *Phys. Status Solidi*, vol. 84, pp. 619–628, 1977. 76, 79, 83, 145

[214] A. Akrap, M. Tran, A. Ubaldini, J. Teyssier, E. Giannini, D. van der Marel, P. Lerch, and C. C. Homes *Phys. Rev. B*, vol. 86, no. 23, p. 235207, 2012. 77, 79, 145

[215] N. Borgwardt, J. Lux, I. Vergara, Z. Wang, A. A. Taskin, K. Segawa, P. H. M. van Loosdrecht, Y. Ando, A. Rosch, and M. Grüninger, "Self-organized charge puddles in a three-dimensional topological material," *Phys. Rev. B*, vol. 93, no. 24, p. 245149, 2016. 77

[216] Y. Tian, G. B. Osterhoudt, S. Jia, R. J. Cava, and K. S. Burch *Appl. Phys. Lett.*, vol. 108, p. 041911, 2016. 79, 83, 145

[217] C.-K. Lee, C.-M. Cheng, S.-C. Weng, W.-C. Chen, K.-D. Tsuei, S.-H. Yu, M. M.-C. Chou, C.-W. Chang, L.-W. Tu, H.-D. Yang, C.-W. Luo, and M. M. Gospodinov, "Robustness of a Topologically Protected Surface State in a Sb2Te2Se Single Crystal," *Sci. Rep.*, vol. 6, no. March, p. 36538, 2016. Supplementary. 79, 145

[218] J. Yuan, M. Zhao, W. Yu, Y. Lu, C. Chen, M. Xu, S. Li, K. Ping Loh, and B. Qiaoliang, "Raman Spectroscopy of Two-Dimensional Bi2TexSe3 x Platelets Produced by Solvothermal Method," *Materials*, vol. 8, no. 8, pp. 5007–5017, 2015. 79, 145

[219] Y. Wang, S. Liu, J. Yuan, P. Wang, J. Chen, J. Li, S. Xiao, Q. Bao, Y. Gao, and J. He, "Why is the bulk resistivity of topological insulators so small?," *Sci. Rep.*, vol. 6, p. 33070, 2016. 79, 145

[220] F. Hulliger, *Structural chemistry of layer-type phases*. D. Reidel, 1976. 80

[221] A. Togo and I. Tanaka, "First principles phonon calculations in materials science," *Scr. Mater.*, vol. 108, pp. 1–5, Nov 2015. 80

[222] J. P. Perdew, K. Burke, and M. Ernzerhof, "Generalized gradient approximation made simple [phys. rev. lett. 77, 3865 (1996)]," *Phys. Rev. Lett.*, vol. 78, pp. 1396–1396, Feb 1997. 80

[223] P. Larson, S. D. Mahanti, and M. G. Kanatzidis, "Electronic structure and transport of bi_2te_3 and $babite_3$," *Phys. Rev. B*, vol. 61, pp. 8162–8171, Mar 2000. 80

[224] G. Kresse and J. Hafner, "Ab initio molecular dynamics for liquid metals," *Phys. Rev. B*, vol. 47, pp. 558–561, Jan 1993. 80

[225] G. Kresse and J. Hafner, "Ab initio molecular-dynamics simulation of the liquid-metal˘amorphous-semiconductor transition in germanium," *Phys. Rev. B*, vol. 49, pp. 14251–14269, May 1994. 80

[226] N. Kumar, B. A. Ruzicka, N. P. Butch, P. Syers, K. Kirshenbaum, J. Paglione, and H. Zhao, "Spatially resolved femtosecond pump-probe study of topological insulator Bi_2Se_3," *Phys. Rev. B*, vol. 83, p. 235306, Jun 2011. 88, 89

[227] L. Cheng, C. La-o vorakiat, C. S. Tang, S. K. Nair, B. Xia, L. Wang, J.-X. Zhu, and E. E. M. Chia, "Temperature-dependent ultrafast carrier and phonon dynamics of topological insulator bi1.5sb0.5te1.8se1.2," *Applied Physics Letters*, vol. 104, no. 21, p. 211906, 2014. 88, 89

[228] Y. Li, V. A. Stoica, L. Endicott, G. Wang, C. Uher, and R. Clarke, "Coherent optical phonon spectroscopy studies of femtosecond-laser modified sb2te3 films," *Applied Physics Letters*, vol. 97, no. 17, p. 171908, 2010. 89

[229] S. Li, H. Huang, W. Zhu, W. Wang, K. Chen, D.-x. Yao, Y. Wang, T. Lai, Y. Wu, and F. Gan, "Femtosecond laser-induced crystallization of amorphous sb2te3 film and coherent phonon spectroscopy characterization and optical injection of electron spins," *Journal of Applied Physics*, vol. 110, no. 5, p. 053523, 2011. 89

[230] A. Q. Wu, X. Xu, and R. Venkatasubramanian, "Ultrafast dynamics of photoexcited coherent phonon in bi2te3 thin films," *Applied Physics Letters*, vol. 92, no. 1, p. 011108, 2008. 89

[231] A. Narita, X.-Y. Wang, X. Feng, and K. Müllen, "New advances in nanographene chemistry," *Chem. Soc. Rev.*, vol. 44, pp. 6616–6643, 2015. 92

[232] A. Enyashin and A. L. Ivanovskii, "Graphene allotropes," *physica status solidi (b)*, vol. 248, pp. 1879 – 1883, 08 2011. 92

[233] F. Bonaccorso, Z. Sun, T. Hasan, and A. C. Ferrari, "Graphene allotropes," *Nature Photonics*, vol. 4, p. 611, 10 2010. 92

[234] K. S. Novoselov, A. K. Geim, S. V. Morozov, D. Jiang, Y. Zhang, S. V. Dubonos, I. V. Grigorieva, and A. A. Firsov, "Electric field effect in atomically thin carbon films," *Science*, vol. 306, no. 5696, pp. 666–669, 2004. 92

[235] K. Wakabayashi, K. ichi Sasaki, T. Nakanishi, and T. Enoki, "Electronic states of graphene nanoribbons and analytical solutions," *Science and Technology of Advanced Materials*, vol. 11, p. 054504, oct 2010. 92

[236] J. Alfonsi and M. Meneghetti, "Excitonic properties of armchair graphene nanoribbons from exact diagonalization of the hubbard model," *New Journal of Physics*, vol. 14, p. 053047, may 2012. 92

[237] R. Denk, M. Hohage, P. Zeppenfeld, J. Cai, C. A. Pignedoli, H. Söde, R. Fasel, X. Feng, K. Müllen, S. Wang, D. Prezzi, A. Ferretti, A. Ruini, E. Molinari, and P. Ruffieux, "Exciton-dominated optical response of ultra-narrow graphene nanoribbons," *Nature Communications*, vol. 5, p. 4253, 2014. 92, 97

[238] F. Schwierz, "Graphene transistors," *Nature Nanotechnology*, vol. 5, p. 487, 5 2010. 92

[239] H. Zhang, Y. Miyamoto, X. Cheng, and A. Rubio, "Optical field terahertz amplitude modulation by graphene nanoribbons," *Nanoscale*, vol. 7, pp. 19012–19017, 2015. 92

[240] I. G. Karafyllidis, "Quantum walks on graphene nanoribbons using quantum gates as coins," *Journal of Computational Science*, vol. 11, pp. 326 – 330, 2015. 92

[241] E. Ahmadi, A. Asgari, and K. Ahmadiniar, "The optical responsivity in ir-photodetector based on armchair graphene nanoribbons with p–i–n structure," *Superlattices and Microstructures*, vol. 52, no. 4, pp. 605 – 611, 2012. 92

[242] X. Zhu, A. P. Hitchcock, C. Bittencourt, P. Umek, and P. Krüger, "Individual titanate nanoribbons studied by 3d-resolved polarization dependent x-ray absorption spectra measured with scanning transmission x-ray microscopy," *The Journal of Physical Chemistry C*, vol. 119, no. 42, pp. 24192–24200, 2015. 92

[243] H. Söde, L. Talirz, O. Gröning, C. A. Pignedoli, R. Berger, X. Feng, K. Müllen, R. Fasel, and P. Ruffieux, "Electronic band dispersion of graphene nanoribbons via fourier-transformed scanning tunneling spectroscopy," *Phys. Rev. B*, vol. 91, p. 045429, Jan 2015. 92

[244] P. Ruffieux, J. Cai, N. C. Plumb, L. Patthey, D. Prezzi, A. Ferretti, E. Molinari, X. Feng, K. Müllen, C. A. Pignedoli, and R. Fasel, "Electronic structure of atomically precise graphene nanoribbons," *ACS Nano*, vol. 6, no. 8, pp. 6930–6935, 2012. PMID: 22853456. 92

[245] L. Yang, M. L. Cohen, and S. G. Louie, "Excitonic effects in the optical spectra of graphene nanoribbons," *Nano Letters*, vol. 7, no. 10, pp. 3112–3115, 2007. PMID: 17824720. 92, 106

[246] X. Zhu and H. Su, "Excitons of edge and surface functionalized graphene nanoribbons," *The Journal of Physical Chemistry C*, vol. 114, no. 41, pp. 17257–17262, 2010. 92

[247] R. Denk, A. Lodi-Rizzini, S. Wang, M. Hohage, P. Zeppenfeld, J. Cai, R. Fasel, P. Ruffieux, R. F. J. Berger, Z. Chen, A. Narita, X. Feng, K. Müllen, R. Biagi, V. De Renzi, D. Prezzi, A. Ruini, and A. Ferretti, "Probing optical excitations in chevron-like armchair graphene nanoribbons," *Nanoscale*, vol. 9, pp. 18326–18333, 2017. 92

[248] G. Soavi, S. Dal Conte, C. Manzoni, D. Viola, A. Narita, Y. Hu, X. Feng, U. Hohenester, E. Molinari, D. Prezzi, K. Müllen, and G. Cerullo, "Exciton–exciton annihilation and biexciton stimulated emission in graphene nanoribbons," *Nature Communications*, vol. 7, p. 11010, 2016. 92, 106

[249] S. A. Jensen, R. Ulbricht, A. Narita, X. Feng, K. Müllen, T. Hertel, D. Turchinovich, and M. Bonn, "Ultrafast photoconductivity of graphene nanoribbons and carbon nanotubes," *Nano Letters*, vol. 13, no. 12, pp. 5925–5930, 2013. PMID: 24093134. 92

[250] B. V. Senkovskiy, M. Pfeiffer, S. K. Alavi, A. Bliesener, J. Zhu, S. Michel, A. V. Fedorov, R. German, D. Hertel, D. Haberer, L. Petaccia, F. R. Fischer, K. Meerholz, P. H. M. van Loosdrecht, K. Lindfors, and A. Grüneis, "Making graphene nanoribbons photoluminescent," *Nano Letters*, vol. 17, no. 7, pp. 4029–4037, 2017. PMID: 28358214. 92, 94, 105

[251] A. C. Ferrari, "Raman spectroscopy of graphene and graphite: Disorder, electron–phonon coupling, doping and nonadiabatic effects," *Solid State Communications*, vol. 143, no. 1, pp. 47 – 57, 2007. Exploring graphene. 92

[252] D. Fausti, O. V. Misochko, and P. H. M. van Loosdrecht, "Ultrafast photoinduced structure phase transition in antimony single crystals," *Phys. Rev. B*, vol. 80, p. 161207, Oct 2009. 93

[253] J. Cai, P. Ruffieux, R. Jaafar, M. Bieri, T. Braun, S. Blankenburg, M. Muoth, A. P. Seitsonen, M. Saleh, X. Feng, K. Müllen, and R. Fasel, "Atomically precise bottom-up fabrication of graphene nanoribbons," *Nature*, vol. 466, p. 470, 2010. 93

[254] B. V. Senkovskiy, A. V. Fedorov, D. Haberer, M. Farjam, K. A. Simonov, A. B. Preobrajenski, N. Mårtensson, N. Atodiresei, V. Caciuc, S. Blügel, A. Rosch, N. I. Verbitskiy, M. Hell, D. V. Evtushinsky, R. German, T. Marangoni, P. H. M. van Loosdrecht, F. R. Fischer, and A. Grüneis, "Semiconductor-to-metal transition and quasiparticle renormalization in doped graphene nanoribbons," *Advanced Electronic Materials*, vol. 3, no. 4, p. 1600490, 2017. 93

[255] R. B. Versteeg, J. Zhu, P. Padmanabhan, C. Boguschewski, R. German, M. Goedecke, P. Becker, and P. H. M. van Loosdrecht, "A tunable time-resolved spontaneous raman spectroscopy setup for probing ultrafast collective excitation and quasiparticle dynamics in quantum materials," *Structural Dynamics*, vol. 5, no. 4, p. 044301, 2018. 94

[256] K.-i. Sasaki, K. Kato, Y. Tokura, S. Suzuki, and T. Sogawa, "Pseudospin for raman d band in armchair graphene nanoribbons," *Phys. Rev. B*, vol. 85, p. 075437, Feb 2012. 94

[257] R. Gillen, M. Mohr, and J. Maultzsch, "Raman-active modes in graphene nanoribbons," *physica status solidi (b)*, vol. 247, no. 11-12, pp. 2941–2944, 2010. 94

[258] S. Linden, D. Zhong, A. Timmer, N. Aghdassi, J. H. Franke, H. Zhang, X. Feng, K. Müllen, H. Fuchs, L. Chi, and H. Zacharias, "Electronic structure of spatially aligned graphene nanoribbons on au(788)," *Phys. Rev. Lett.*, vol. 108, p. 216801, May 2012. 97, 106

[259] O. Deniz, C. Sánchez-Sánchez, T. Dumslaff, X. Feng, A. Narita, K. Müllen, N. Kharche, V. Meunier, R. Fasel, and P. Ruffieux, "Revealing the electronic structure of silicon intercalated armchair graphene nanoribbons by scanning tunneling spectroscopy," *Nano Letters*, vol. 17, no. 4, pp. 2197–2203, 2017. PMID: 28301723. 97

[260] D. Song, F. Wang, G. Dukovic, M. Zheng, E. D. Semke, L. E. Brus, and T. F. Heinz, "Direct measurement of the lifetime of optical phonons in single-walled carbon nanotubes," *Phys. Rev. Lett.*, vol. 100, p. 225503, Jun 2008. 97, 99

[261] H. Yan, D. Song, K. F. Mak, I. Chatzakis, J. Maultzsch, and T. F. Heinz, "Time-resolved raman spectroscopy of optical phonons in graphite: Phonon anharmonic coupling and anomalous stiffening," *Phys. Rev. B*, vol. 80, p. 121403, Sep 2009. 97, 105

[262] K. Kang, D. Abdula, D. G. Cahill, and M. Shim, "Lifetimes of optical phonons in graphene and graphite by time-resolved incoherent anti-stokes raman scattering," *Phys. Rev. B*, vol. 81, p. 165405, Apr 2010. 97, 99, 105

[263] K. Kang, T. Ozel, D. G. Cahill, and M. Shim, "Optical phonon lifetimes in single-walled carbon nanotubes by time-resolved raman scattering," *Nano Letters*, vol. 8, no. 12, pp. 4642–4647, 2008. PMID: 19367808. 99

[264] J. M. Nesbitt and D. C. Smith, "Measurements of the population lifetime of d band and g band phonons in single-walled carbon nanotubes," *Nano Letters*, vol. 13, no. 2, pp. 416–422, 2013. PMID: 23297761. 99

[265] S. G. Chou, M. F. DeCamp, J. Jiang, G. G. Samsonidze, E. B. Barros, F. Plentz, A. Jorio, M. Zheng, G. B. Onoa, E. D. Semke, A. Tokmakoff, R. Saito, G. Dresselhaus, and M. S. Dresselhaus, "Phonon-assisted exciton relaxation dynamics for a (6,5)-enriched dna-wrapped single-walled carbon nanotube sample," *Phys. Rev. B*, vol. 72, p. 195415, Nov 2005. 99

[266] D. J. Styers-Barnett, S. P. Ellison, C. Park, K. E. Wise, and J. M. Papanikolas, "Ultrafast dynamics of single-walled carbon nanotubes dispersed in polymer films," *The Journal of Physical Chemistry A*, vol. 109, no. 2, pp. 289–292, 2005. PMID: 16833346. 99

[267] D. J. Styers-Barnett, S. P. Ellison, B. P. Mehl, B. C. Westlake, R. L. House, C. Park, K. E. Wise, and J. M. Papanikolas, "Exciton dynamics and biexciton formation in single-walled carbon nanotubes studied with femtosecond transient absorption spectroscopy," *The Journal of Physical Chemistry C*, vol. 112, no. 12, pp. 4507–4516, 2008. 99

[268] O. A. Dyatlova, C. Köhler, E. Malic, J. Gomis-Bresco, J. Maultzsch, A. Tsagan-Mandzhiev, T. Watermann, A. Knorr, and U. Woggon, "Ultrafast relaxation

dynamics via acoustic phonons in carbon nanotubes," *Nano Letters*, vol. 12, no. 5, pp. 2249–2253, 2012. PMID: 22432930. 99

[269] F. Wang, G. Dukovic, L. E. Brus, and T. F. Heinz, "Time-resolved fluorescence of carbon nanotubes and its implication for radiative lifetimes," *Phys. Rev. Lett.*, vol. 92, p. 177401, Apr 2004. 105

[270] H. Zhao and S. Mazumdar, "Electron-electron interaction effects on the optical excitations of semiconducting single-walled carbon nanotubes," *Phys. Rev. Lett.*, vol. 93, p. 157402, Oct 2004. 106

[271] R. M. Russo, E. J. Mele, C. L. Kane, I. V. Rubtsov, M. J. Therien, and D. E. Luzzi, "One-dimensional diffusion-limited relaxation of photoexcitations in suspensions of single-walled carbon nanotubes," *Phys. Rev. B*, vol. 74, p. 041405, Jul 2006. 106

[272] J. Allam, M. T. Sajjad, R. Sutton, K. Litvinenko, Z. Wang, S. Siddique, Q.-H. Yang, W. H. Loh, and T. Brown, "Measurement of a reaction-diffusion crossover in exciton-exciton recombination inside carbon nanotubes using femtosecond optical absorption," *Phys. Rev. Lett.*, vol. 111, p. 197401, Nov 2013. 106

[273] G. Soavi, F. Scotognella, D. Viola, T. Hefner, T. Hertel, G. Cerullo, and G. Lanzani, "High energetic excitons in carbon nanotubes directly probe charge-carriers," *Scientific Reports*, vol. 5, 2015. 106

List of Figures

List of Tables

Summary

The scope of this work covers phenomena in different classes of materials, investigated by spatial, temperature, polarization, and time dependent Raman spectroscopy. It was shown that local symmetry changes observed by different Raman spectroscopy techniques, influences significantly the macroscopic properties of a material. Various Raman active excitation were investigated such as one- and two- phonon, one- and two- magnon, exciton, and electronic background excitations.

In $Y_{0.63}Ca_{0.37}TiO_3$ the temperature-driven conducting properties could be connected to the percolation of local conducting phases, forced by local structural changes. In $Ca_2Ru_{0.998}Ti_{0.002}O_4$ it was shown that the electric current induced metal-insulator transition is a consequence of local changes in the octaheder structrure of the perovskite percolating again through the sample and changing not only the conductivity, but also the magnetic ordering by increasing the current. In $BiSbTeSe_2$ it was shown that the preferred local structure of the atomic composition necessarily breaks inversion symmetry and explains consequently the unexpectedly high number of Raman active phonon modes. In surface aligned 7-atom wide armchair graphene nanoribbons it was shown that the exciton dynamics can be traced by optical pump induced changes of the phonon population.

Acknowledgement

I would not be the person I have become today if I had not been accompanied by so many wonderful and inspiring people. I hope that these people know about their importance, even if it will hardly be possible for me to do them justice in their entirety. First of all, I would like to thank my family, who gave me everything. I thank Paul for the chance and his confidence to send me on this journey. Every journey needs a compass and I thank you, Fulvio and Caesarina, for bringing me every time to the right road when it was needed. But, even the best ship is only as good as its crew. You made a bad ship swim, thank you Britta (Muddi), Rolf and Iason, Jingyi, Prashant, Thomas, Kestutis, Henning, Robin, Anuja, Matteo, Ionela, Andrea, Jens, Yajun, Chris, Christoph, Julian, Bernhard, Ignacio, Sebastian, Philipp, Elina, Kiran, Yu, Fumiya, Lin, Chris, Lena, Raluca, Evgenia, Jörg, Manpreet, Simon, Petra, Claudia, Oliver, Johannes, and Hamoon, for all the small and the big things which made this time so great!

List of Publications

Zero-dimensional (CH3NH3)3Bi2I9 perovskite for optoelectronic applications

S. Öz *et al.*, *Solar Energy Materials and Solar Cells*, **158**, 195 - 201 (2016)

Doi: 10.1016/j.solmat.2016.01.035

Semiconductor-to-Metal Transition and Quasiparticle Renormalization in Doped Graphene Nanoribbons

B. Senkovskiy *et al.*, *Advanced Electronic Materials*, **3**, 4, 1600490 (2017)

Doi: 10.1021/acs.nanolett.7b00147

Making Graphene Nanoribbons Photoluminescent

B. Senkovskiy *et al.*, *Nano Letters*, **17**, 4029-4037 (2017)

Doi: 10.1021/acs.nanolett.7b00147

A tunable time-resolved spontaneous Raman spectroscopy setup for probing ultrafast collective excitation and quasiparticle dynamics in quantum materials

R.B. Versteeg *et al.*, *Structural Dynamics*, **5**, 4, 044301 (2018)

Doi: 10.1063/1.5037784

Temperature dependent percolation mechanism for conductivity in $Y_{0.63}Ca_{0.37}TiO_4$

R. German *et al.*, *Materials Research Express*, **5**, 126101 (2018)

Doi: 10.1088/2053-1591/aae0cc

Exciton and phonon dynamics in highly aligned 7-atom wide armchair graphene nanoribbons as seen by time-resolved spontaneous Raman scattering

J. Zhu *et al.*, *Nanoscale*, **10**, 37, 17975-17982, (2018)

Doi: 10.1039/C8NR05950K

Phonon mode calculations and Raman spectroscopy of the bulk-insulating topological insulator $BiSbTeSe_2$
R. German *et al.*, *Phys. Rev. Materials*, **5**, 054204 (2019)
Doi: 10.1103/PhysRevMaterials.3.054204

Charge transport in oxygen-deficient $EuTiO_3$**: The emerging picture of dilute metallicity in quantum-paraelectric perovskite oxides**
J. Engelmayer *et al.*, *Phys. Rev. Materials*, **3**, 5, 051401, (2019)
Doi: 10.1103/PhysRevMaterials.3.051401

High-field quantum disordered state in $\alpha - RuCl_3$**: Spin flips, bound states, and multiparticle continuum**
A. Sahasrabudhe *et al.*, *Phys. Rev. B*, **101**, 14, 140410, (2020)
Doi: 10.1103/PhysRevB.101.140410

Unraveling the Excitonic Transition and Associated Dynamics in Confined Long Linear Carbon-chains with Time-Resolved Resonance Raman Scattering
J. Zhu *et al.*, *arXiv* (2021)
Doi: 0.48550/ARXIV.2105.14014

Declaration of Authorship

(Gemäß der Promotionsordnung vom 12. März 2020)
Hiermit versichere ich an Eides statt, dass ich die vorliegende Dissertation selbstständig und ohne die Benutzung anderer als der angegebenen Hilfsmittel und Literatur angefertigt habe. Alle Stellen, die wörtlich oder sinngemäß aus veröffentlichten und nicht veröffentlichten Werken dem Wortlaut oder dem Sinn nach entnommen wurden, sind als solche kenntlich gemacht. Ich versichere an Eides statt, dass diese Dissertation noch keiner anderen Fakultät oder Universität zur Prüfung vorgelegen hat; dass sie - abgesehen von unten angegebenen Teilpublikationen und eingebundenen Artikeln und Manuskripten - noch nicht veröffentlicht worden ist sowie, dass ich eine Veröffentlichung der Dissertation vor Abschluss der Promotion nicht ohne Genehmigung des Promotionsausschusses vornehmen werde. Die Bestimmungen dieser Ordnung sind mir bekannt. Darüber hinaus erkläre ich hiermit, dass ich die Ordnung zur Sicherung guter wissenschaftlicher Praxis und zum Umgang mit wissenschaftlichem Fehlverhalten der Universität zu Köln gelesen und sie bei der Durchführung der Dissertation zugrundeliegenden Arbeiten und der schriftlich verfassten Dissertation beachtet habe und verpflichte mich hiermit, die dort genannten Vorgaben bei allen wissenschaftlichen Tätigkeiten zu beachten und umzusetzen. Ich versichere, dass die eingereichte elektronische Fassung der eingereichten Druckfassung vollständig entspricht.

Teilpublikationen

Temperature dependent percolation mechanism for conductivity in $Y_{0.63}Ca_{0.37}TiO_4$
R. German *et al.*, *Materials Research Express*, **5**, 126101 (2018)
Doi: 10.1088/2053-1591/aae0cc

Exciton and phonon dynamics in highly aligned 7-atom wide armchair graphene nanoribbons as seen by time-resolved spontaneous Raman scattering
J. Zhu *et al.*, *Nanoscale*, **10**, 37, 17975-17982, (2018)
Doi: 10.1039/C8NR05950K

Phonon mode calculations and Raman spectroscopy of the bulk-insulating topological insulator $BiSbTeSe_2$
R. German *et al.*, *Phys. Rev. Materials*, **5**, 054204 (2019)
Doi: 10.1103/PhysRevMaterials.3.054204

Raphael German

Wissen, 11.07.2022